Observations of Winter Storms with a Video Disdrometer and Polarimetric Radar

by
Kyoko Ikeda

Department of Atmospheric Science
Colorado State University
Fort Collins, Colorado

Colorado State University

Department of Atmospheric Science

Paper No. 783

OBSERVATIONS OF WINTER STORMS WITH A VIDEO DISDROMETER AND POLARIMETRIC RADAR

Submitted by

KYOKO IKEDA

Department of Atmospheric Sciences

In partial fulfillment of the requirements

For the Degree of Master of Science

Colorado State University

Fort Collins, Colorado

Spring 2007

ABSTRACT

OBSERVATIONS OF WINTER STORMS WITH A VIDEO DISDROMETER AND POLARIMETRIC RADAR

With efforts to upgrade the operational NEXRAD radars to include polarimetric capability underway, there are growing interests in developing radar-based algorithms for classifying hydrometeor types, quantifying winter precipitation, and improving the parameterization of winter precipitation in numerical forecast models. The capabilities of polarimetric radars, such as to better quantify warm season precipitation, have been demonstrated in various studies. However, these tasks are further complicated for winter precipitation by the need to know hydrometeor phase and bulk density of ice particles. In this study, data collected with a two-dimensional video disdrometer and S-band dual-polarization radar during the Winter Icing and Storms Project 2004 (WISP04) storms are examined in support of ongoing research to develop radar-based algorithms for cold season precipitation.

The capability to match radar-measured and disdrometer-based calculations of radar reflectivity factor and differential reflectivity is essential for retrieving hydrometeor characteristics with radar. During the WISP04, the disdrometer provided detailed information regarding hydrometeor size, number concentration, terminal velocity, and

shape during the precipitation events. In this study, bulk ice particle density is estimated using an empirical relationship derived from disdrometer measurements of precipitation volume and rain gauge measurements of precipitation mass. Reflectivity and differential reflectivity, as measured by radar and computed from disdrometer observations are compared, and the combined dataset is used to examine storm microphysical properties. The measurements and computed values show good agreement and reveal that the radar detected subtle changes in the characteristics of winter precipitation. Additionally, sensitivity of the scattering computations to assumed ice particle characteristics is examined, and particle size distributions from radar measurements are retrieved for comparisons with the disdrometer observations.

Kyoko Ikeda
Atmospheric Science Department
Colorado State University
Fort Collins, CO 80523
Spring 2007

ACKNOWLEDGEMENTS

I would like to express my appreciation to my advisor, Dr. Steven Rutledge, for his guidance. I am grateful to Drs. E. Brandes, G. Zhang, V. Bringi, W. Cotton, and J. Vivekanandan for their invaluable insight and advice on the research topic, S. Landolt for providing valuable support for operating the disdrometer during the WISP04 project and insightful conversation, S. Ellis for enlightening discussion regarding the hydrometeor classification algorithm, and P. Kennedy for his input on our radar data analyses. The kind effort of Ms. P. Warfel for reviewing this document, P. Kennedy and D. Brunkow for preparing the CSU-CHILL radar data, and R. Rilling for preparing the S-Pol radar data for analysis are appreciated. I am also grateful to Dr. M. Politovich for the opportunity to participate in the WISP04 field project, and the CSU radar meteorology group for helpful discussions and guidance. This work was supported by the Federal Aviation Weather Research Program and the National Center for Atmospheric Research. The views expressed are those of the authors and do not necessarily represent the official policy of the U.S. government.

TABLE OF CONTENTS

LIST OF FIGURES

LIST OF TABLES

Equation Chapter 1 Section 1

CHAPTER 1

INTRODUCTION

The Winter Icing and Storms Project 2004 (WISP04) was conducted from February to April 2004 in north central Colorado. Program objectives were to evaluate remote sensing techniques for icing detection and to quantify winter precipitation in support of airport deicing operations. The storms were probed with a two dimensional-video disdrometer and two S-band (10 cm) dual-polarization radars in support of ongoing research to develop radar-based algorithms for classifying hydrometeor types, quantifying winter precipitation, and improving the parameterization of winter precipitation in numerical forecast models. An ability to match radar-measured and disdrometer-based radar parameters is essential when developing algorithms for winter precipitation. As a first step, this study presents the microphysical properties of the precipitation systems using the disdrometer data to verify that the radar detects subtle changes in the characteristics of winter precipitation, and computes the equivalent reflectivity factor (Z_H) and the differential reflectivity (Z_{DR}) from the disdrometer data in order to compare with the radar measurements. The radar measurements are then used to retrieve snow particle size distributions for comparison with the disdrometer observations.

The calculations of Z_H and Z_{DR} are based on scattering amplitudes of raindrops and ice particles computed with the transition-matrix (T matrix) method (Barber and Yeh 1975; Vivekananden et al. 1991). Knowledge about bulk ice particle density, approximate particle shape, and fall mode are essential for computing scattering amplitudes. However, properties of ice particles are complex. In this study, the scattering amplitudes during the rain-snow transition and snow phases are estimated according to an empirical relationship between particle size and bulk ice particle density developed from past disdrometer observations. The sensitivity of the scattering calculations to the assumed hydrometeor properties is then investigated. In a sense, the density-size relationship allows for changes in bulk ice particle density that are anticipated to occur with storm evolution. Similar approaches have been used to estimate radar parameters (e.g., Vivekanandan et al. 1994; Ryzhkov et al. 1998). However, comparisons of the computed radar parameters with the video disdrometer have not been performed for cold season precipitation. Video disdrometers provide important information regarding hydrometeor size, shape, terminal velocity, and number concentration at high temporal resolution, while polarimetric radar measurements give insight regarding microphysical properties of precipitating clouds owing to their sensitivity to particle size, shape, orientation, phase, and bulk density. When combined, the datasets are excellent for developing radar-based algorithms concerning winter precipitation as mentioned previously.

In this document, the properties of polarimetric radar measurements and a summary of previous studies on hydrometeor scattering calculations and comparisons between the measured- and computed-radar parameters are introduced next. The

locations of the instruments and the data used in this study are described in Chapter 2, and Chapter 3 outlines the calculation method of Z_H and Z_{DR} based on the disdrometer measurements. Analyses of the disdrometer and radar measurements during two winter storms and radar-disdrometer comparisons of the radar variables are given in Chapters 4 and 5. The sensitivities of the scattering calculations to properties of ice particles will be examined in Chapter 6, and finally, Chapter 7 demonstrates microphysical retrievals based on the polarimetric radar measurements. The summary and concluding remarks are given in Chapter 8.

1.1 Properties of polarimetric radar measurements

The principle of dual-polarization radar is to transmit horizontally and vertically polarized electromagnetic waves and receive backscattered signals. The radar backscatter cross-sections are not the same for the two polarizations because illuminated hydrometeors have a variation of shapes, bulk densities, and a distribution of orientations. Signal properties change continuously due to scattering, differential attenuation, differential phase shifts, and depolarization in the precipitation yielding information regarding the illuminated hydrometeors. The capabilities of polarimetric radars have been demonstrated in various studies, e.g., in improving rainfall estimates (e.g., Seliga et al. 1981; Goddard and Cherry 1984; Brandes et al. 2002); retrieving raindrop size distributions (e.g., Bringi et al. 2001; Zhang et al. 2001; Gorgucci et al. 2002; Brandes et al. 2004); identifying hydrometeors (Vivekanandan et al. 1999; Straka et al. 2000); estimating melting levels (Brandes and Ikeda 2004); and detecting hail (e.g., Aydin et al.

1986; Bringi et al. 1986; Brandes et al. 1995). Efforts in upgrading the operational NEXRAD (WSR-88D) radars to include polarimetric capability are in progress (Ryzhkov et al. 2005). Microphysical studies using dual-frequency radar (Vivekanandan et al. 2001) and airborne polarimetric radar (Wolde et al. 2001) are also new areas in remote sensing research.

Equivalent radar reflectivity (reflectivity or Z_H, hereafter) and differential reflectivity (Z_{DR}) are the radar parameters primarily discussed in this study. Radar reflectivity at horizontal (H) and vertical polarization (V) for a unit volume ($mm^6\ m^{-3}$) are defined

$$Z_{H,V} = \frac{\lambda^4}{\pi^5 |K_w|^2} \int_0^{D_{max}} \sigma_{H,V}(D) N(D) dD \tag{1.1}$$

where λ is the radar wavelength, K_w is the dielectric factor of water, $\sigma_{H,V}(D)$ are the radar cross-sections of scatterers at horizontal and vertical polarization, N(D) is the size distribution, D is the particle equivalent volume diameter, and D_{max} is the maximum particle size. In practice, $Z_{H,V}$ is expressed in dBZ ($10\log_{10}Z_H$). Most hydrometeors are considered Rayleigh scatterers at the S-band wavelength unless they are large and wet such as melting snow aggregates and wet hail. The radar cross-sections in the Rayleigh scattering regime are a function of particle size and dielectric factor, i.e., particle bulk density. Typically, the radar returns are dominated by the presence of large particles due to the 6th power of the particle diameter, which appears in the expression of $\sigma_{H,V}(D)$. Scattering behavior becomes complex in the Mie regime due to loss of propagating electromagnetic waves by the forward scattering.

The differential reflectivity (Z_{DR}, in dB) has the form

$$Z_{DR} = 10 \times \log_{10}(Z_H / Z_V). \quad (1.2)$$

Z_{DR} is independent of particle concentration because it is a ratio of reflectivity at horizontal and vertical polarizations. It is sensitive to particle bulk density, shape and canting angle and can be interpreted as the reflectivity-weighted mean aspect ratio of the illuminated hydrometeors. Z_{DR} is positive (negative) for oblate (prolate) particles. For particles that are spherical or have a random distribution of orientations, Z_{DR} is zero. Raindrops tend to flatten while falling and orient themselves with their major axis close to horizontal in the mean with a small oscillation about the horizontal axes. Typically, Z_{DR} ranges from 0.2 to 3 dB for rain and increases with drop size and rain intensity (Doviak and Zrnic 1993). Pristine ice crystals fall with their major axes near horizontal and can have Z_{DR} values as large as 2 to 5 dB, depending on crystal type (e.g., Vivekanandan et al. 1993; Ryzhkov and Zrnic 1998; Ryzhkov et al. 1998). Aggregates have high aspect ratio (vertical axis divided by horizontal axis) and low bulk density. Consequently, Z_{DR} is usually < 0.5 dB (Meischner et al. 1991; Vivekanandan et al. 1993; Ryzhkov and Zrnic 1998). Z_{DR} sensitivity to a particle shape is more pronounced for particles with high bulk density such as pristine ice crystals, but it is less when bulk density is low (Herzegh and Jameson 1992).

Linear depolarization ratio (LDR) and copolar correlation coefficients (ρ_{HV}) are also useful parameters in winter precipitation. LDR (dB) is the ratio of the cross-polar and copolar signals and is expressed as

$$LDR = 10 \times \log_{10}(Z_{VH} / Z_{HH}), \quad (1.3)$$

where Z_{VH} is the signal received at vertical polarization for a horizontally transmitted polarization wave and Z_{HH} is the signals received and transmitted at a horizontal

polarization. LDR is large when the alignment of particles is random. Canting angles of raindrops are narrowly distributed about the horizontal. Hence, LDR values for rain are small (on the order of –35 to –25 dB). Values for dry snowflakes are also small even if the particles wobble due to their small bulk density. The largest values are associated with wet aspherical particles such as melting snowflakes. Melting snow typically has an LDR values between –20 to –15 dB.

The correlation between copolar returns at horizontal and vertical polarization at zero time lag is expressed

$$\left|\rho_{HV}(0)\right| = \left\langle S_{VV} S_{HH}^{*} \right\rangle / \left(\left\langle S_{HH}^{2} \right\rangle^{1/2} \left\langle S_{VV}^{2} \right\rangle^{1/2} \right), \tag{1.4}$$

where S_{vv} and S_{HH} are scattering amplitudes of illuminated hydrometeors at horizontal and vertical polarization, respectively, and brackets express time-averaged quantities. Correlation coefficients (ρ_{HV}, hereafter) are close to unity when radar sample volumes contain homogeneous targets. ρ_{HV} is low (< 0.9) in mixed-phase conditions. The correlations are reduced for non-meteorological targets (< 0.7-0.8). Pronounced signatures of melting in LDR and ρ_{HV} often facilitate the determination of melting levels (0°C) even when the reflectivity bright band is absent.

1.2 Previous studies

Hall et al. (1984) modeled relations between particle axis ratio and Z_{DR} for different hydrometeors based on Rayleigh-Gans scattering theory (Bringi and Chandrasekar 2001). Using the relations to interpret measurements of Z_H and Z_{DR} from various precipitations, they found that the additional data provided by dual-polarization

radar better describe hydrometeor types and furthermore distinguishes hydrometeors from non-meteorological targets. Since this study, there have been many studies that have demonstrated improvements in hydrometeor identification, data quality control, rainfall estimation, and characterization of non-meteorological echo using the full suite of polarimetric variables. Below the discussion focuses on such studies applied to cold clouds.

Evans and Vivekanandan (1990) computed backscattering and extinction matrices using the discrete dipole approximation approach (Purcell and Pennypacker 1973; Goedecke and O'Brien 1988) for plates, columns, and needles having particle sizes from 0.06 to 2.0 mm and bulk densities between 0.92 and 0.23 g cm^{-3}. Their modeling work revealed that the particle shapes played an important role, and particle bulk density was a significant contributing factor to values of the polarimetric radar measurables. This in turn suggested that the bulk density could be retrieved from Z_{DR} once assumptions were made about particle orientation and shape.

A rigorous approach using a combination of the T matrix and Mueller matrix for computing radar parameters was presented by Vivekanandan et al. (1991) in order to demonstrate the effect of particles' canting angle distributions and antenna elevation on polarimetric radar measurables. In this method, the computational method started with computing scattering from axisymmetric particles by the T-matrix approach, which took into account non-Rayleigh scattering effects. Subsequently, the Mueller matrix simulated hydrometeor fall modes and computed polarimetric radar parameters with respect to various antenna elevation angles. Vivekanandan et al. (1993) followed this approach to examine radar responses in mixtures of hydrometeors. Their computations of single-

scatter radar observables for rain, hail, graupel, ice particles, and snow aggregates based on various assumed size, shape, density, and orientations (their Table 1) clearly showed how individual species affected radar observables. The application of the computational method on a numerical cloud model simulation revealed that while the rain and graupel/hail having large bulk density were easily detected, snow aggregates were difficult to detect because of its low density and tumbling motions. Nevertheless, the responses of the polarimetric parameters to the evolving cloud showed promise in utilizing the polarimetric radar measurements for relating kinematic and microphysical aspects of cloud systems.

In the subsequent work, Vivekanandan et al. (1994) continued investigating single scattering properties of ice crystals, but they used an expression of Z_H and Z_{DR} in terms of bulk density and axis ratio derived from a two-dimensional least-square fit curve of scattering amplitudes with respect to the two parameters. Analyses of polarimetric radar measurements in winter precipitation based on the modeling results showed that multiparameter radar measurements are useful in qualitatively identifying the presence of oriented ice crystals. Additionally, they proposed that if the transformation process between ice crystals and aggregates was approximated with an ad hoc relation between particle bulk density (ρ_s) and axis ratio (r), e.g.,

$$\rho_s \times r = 0.92, \tag{1.5}$$

the values of density or axis ratio could be inferred from Z_{DR}, which in turn yields improvement in the radar-based retrievals of ice water content. However, sensitivity tests of the T-matrix based scattering calculations to assumed particle bulk density, shape, and distributions performed by Hogan et al. (2000) clearly demonstrated a wide range of

retrieved ice water content depending on the particle characteristic assumption and emphasized the challenges in determining the representative characteristics of ice particles for retrievals of precipitation/cloud properties.

As Vivekanandan et al. (1994) stated radar parameter modeling studies assist the microphysical interpretation of radar measurements which in turn lead to an improved precipitation retrieval algorithm. Further improvements should be possible when multiparameter radar observations and in situ cloud measurements are available to validate the model computations. However, few modeling studies have utilized comprehensive in situ verification data. Matrosov et al. (1996) modeled the elevation-angle dependencies of radar depolarization for ice crystals and aggregated snow based on the Rayleigh theory at Ka-band, and verified the model results with field observations of ice particles. The model approximated the bulk density and aspect ratios of ice crystals using size-dependent power relations from Pruppacher and Klett (1997), Heymsfield (1972), Auer and Veal (1970), Jayaweera and Cottis (1969), and Jayaweera and Ohtake (1974). The ice crystals were assumed to have a gamma distribution. For aggregates, a density-size relation of Locatelli and Hobbs (1974),

$$\rho_s = 0.07D^{-1.1} \tag{1.6}$$

was applied. The aggregates were considered spheroids with aspect ratios of 0.3 and 0.8. In general, the model calculations agreed well with the measurements, and demonstrated a possibility that depolarization ratio dependencies on radar elevation angles can be used to distinguish between various types of ice hydrometeors and to estimate their shapes.

Ryzhkov et al. (1998) applied the scattering model of Matrosov et al. (1996) for a S-band radar to retrieve ice water content from polarimetric measurements. A

consistency check was made between the radar-measured and estimated Z_H values from in-situ 2D-P (two-dimensional precipitation) data collected during a single-flight penetration through an ice-phase cloud. The average difference between the measured and estimated Z_H was approximately 5-7 dBZ. Additional verification of the scattering model presented by Matrosov et al. (2001) showed consistent results. The discrepancy in the Ryzhkov et al. study may have come from temporal difference between the radar scans and the aircraft flight through a developing convective cloud.

More recently, Liao et al. (2005) presented an approach to retrieve snow particle size distributions with airborne dual-wavelength radar measurements and verified the retrievals with in situ aircraft measurements and ground-based S- and X-band radars. A detail description of the dual-wavelength-based retrieval algorithm is given in Liao et al. (2005). The key point in this approach is to relate the difference of radar reflectivity at two wavelengths (DFR) to the equivalent median volume diameter (D_0). In essence, the DFR increases with D_0 as particles enter the Mie scattering regime for a shorter wavelength while remaining in the Rayleigh regime at the longer wavelength. Particle size distributions can be retrieved from DFR if assumptions about bulk ice particle density and shape parameter (μ) of gamma particle size distributions are made.

Liao et al. (2005) first examined the relation between D_0 and the DFR for a pair of X- and Ka-band radars and a pair of S- and X-band radars. The reflectivity at each wavelength was computed based on the Mie theory (Bringi and Chandrasekar 2001) with the bulk ice particle density between 0.05 and 0.8 g cm^{-3} and a gamma size distribution with a constant μ between -0.5 and 6. For the X-Ka band pair, the relationship between DFR and D_0 was independent of ρ_s for $D_0 < 3.5$ mm, but was sensitive to μ which may

lead to a significant uncertainty in the estimates of D_0. The dependencies of the DFR-D_0 relation on μ and ρ_s were more pronounced for the S-X band pair. Next, they retrieved D_0 and N_t based on an airborne dual-wavelength radar with X- and Ka-band wavelengths. The retrievals agreed well with the 2D-P observations from a separate aircraft when μ = -0.5 and $\rho_s = 0.2$ g cm^{-3} in a region dominated by aggregates and when $\mu = 1$ and $\rho_s = 0.7$ g cm^{-3} in a graupel-dominated region. The retrievals for the S-X band pair was reasonably consistent with the observation despite the fact that the S-band radar was on the ground and the X-band component was provided by the airborne radar.

Verification data collected with research aircraft have a number of advantages. Most importantly, aircraft can sample the regions of cloud system that is of most interest and follow its evolution. Additionally, aircraft penetrate precipitation systems at various heights providing information on vertical structure. However, aircraft locations do not always coincide with ground-based radar scanning volumes, which yields uncertainty in the verification data. Additional uncertainty may also arise from the fact that the sample volume of radar is much greater than point-measurements made by an aircraft. Moreover, comparisons with the ground-based radars are limited to the number of times the aircraft intersects the region of precipitation scanned by the radar. Verification of the model computations and retrieval methods is also difficult when in situ measurements of basic hydrometeor properties such as particle size distribution, shape, orientation, and bulk density are not available. Assumptions may be made based on previous observational studies, e.g., Locatelli and Hobbs (1974), Heymsfield (1978), and Mitchell et al. (1990). However, as previously noted, uncertainties in basic hydrometeor

properties significantly affect retrievals of microphysical aspects of clouds and precipitation, further complicating the verification process.

Ground-based optical devices with a capability of sampling frozen hydrometeors such as the 2-D video disdrometer is another type of instrument that is useful for verification. An optical sensor developed by Locatelli and Hobbs (1974), high-frequency optical snow measuring device developed by Muramoto et al. (1995), and the HVSD (Hydrometeor Velocity and Shape Detector; Barthazy 2004) have been used to study characteristics of ice particles. However, few studies have performed radar-disdrometer comparisons of radar parameters or microphysical retrievals. For example, Löffler-Mang and Blahak (2001) obtained snow observations in Germany with a Particle Size and Velocity (PARSIVEL) disdrometer to compute radar reflectivity based on the theoretical work of Smith (1984). The PARSIVEL disdrometer is an optical sensor that produces a horizontal sheet of light some of which is blocked as particles enter the disdrometer and measures maximum particle size and fall velocity. The fall velocity of individual particles is determined from the duration of the light blockage as they pass through the light beam of 1 mm in width, assuming that the particles are spherical and have diameters equal to the measured maximum diameter. Löffler-Mang and Blahak used the 5-minute averages of these values due to a large scatter in the individual terminal velocity measurements. Radar reflectivities were calculated from 5-minute particle size distributions and average fall velocities based on the disdrometer data. Mass of the precipitation particles was estimated from an empirical relation between particle size and mass for graupel from Locatelli and Hobbs (1974). The calculated reflectivities systematically underestimated the reflectivity by 3-5 dBZ in stratiform precipitation;

while the differences were between –6 and 16 dBZ in convective cases. The authors attributed the biases to the presence of non-graupel like ice particles, strong temporal and spatial variability of the snow event, and temporal variations of the ice particle type. The mass estimated from the Locattelli and Hobbs' relation possibly contributed to the reflectivity bias because their maximum diameters were generally smaller than those determined by Locattelli and Hobbs (1974), who defined the maximum diameters to be the diameter of the smallest circle into which a snowflake will fit. Consistent with the earlier studies, this study concluded that the mass-size relation (or density-size relation, in essence) to be the most critical factor in the calculations.

Recently, Brandes et al. (2006) compiled data collected with a two-dimensional video disdrometer (Schöenhuber 1998; Kruger and Krajewski 2002) during winter seasons (October-April) between 2003 and 2005 in Colorado. The study demonstrated the capabilities of the video disdrometer in measuring winter precipitation and presented inter-relationships among properties of frozen particles and environmental state variables. As will be discussed in Chapter 2, the video disdrometer is capable of "seeing" the two-dimensional shapes of the ice particles, providing good measurements of equivolumetric diameters and fall velocity for individual particle. Although the measurements are only taken at a fixed point, an advantage to using ground-based disdrometers is its capability to continuously monitor changes in precipitation characteristics associated with storm evolution. The two-dimensional disdrometer measurements in rain have proven useful for studying the physical properties of raindrops (Thurai and Bringi 2005) and verifying radar-based retrievals of size distributions (e.g., Brandes et al. 2002). Brandes et al. (2006) showed that disdrometer data in winter precipitation are just as useful for studies

of particle characterization and remote sensing verification. A goal of the present study is to further demonstrate these points.

Equation Chapter 2 Section 1

CHAPTER 2

STUDY AREA AND DATA

Figure 2.1a shows the WISP04 field project study area. The field project was mainly focused in the Front Range region, west of Denver, CO. The data used in this study come from two radar systems, a 2-D video disdrometer, a radiometer, and a wind profiler. Field notes from the author supplement the disdrometer data. Observations of crystal type, size, degree of riming, and amount of aggregation were made every 15 minutes.

The radar data were collected with the NCAR's S-band dual-polarization radar (S-Pol) located at Marshall, Colorado (Fig. 2.1a). Scan strategies included plan-position indicator (PPI) scans at 0.5 and 1.5° antenna elevation angles and range-height indicator (RHI) scans between 40 and 44° azimuth angles, over the video disdrometer placed at a range of 19 km and an azimuth angle of 42° from the radar. The Z_{DR} values were corrected for a system bias of 0.08 dB. The bias was determined from radar data that were collected by rotating the antenna while pointing vertically in light rain. In theory, raindrops should produce a Z_{DR} value of 0 dB in the mean when viewed with a vertically-pointing antenna.

The Colorado State University CSU-CHILL radar, operating at S-band and located 54 km to the northwest of the disdrometer site (Fig. 2.1a), collected data on 20

February 2004 during one of the two case studies. Sector scans at 0.7, 1.1, and 1.5° and RHI scans between 214 and 228° were performed over the disdrometer. The CSU-CHILL's Z_{DR} bias for this event is unknown. However, Z_{DR} was typically 0.3 dB lower than that of the S-Pol system.

The radar-disdrometer comparisons are made using data points from the low-level PPI scans (at 0.5 and 1.5° for the S-Pol; at 0.7° for the CSU-CHILL) and portions of the RHI scans with the radar beam heights corresponding to those of the PPI scan beams over the disdrometer site. The main lobe of the radar beams passed over the disdrometer site at 408 m (S-Pol at 0.5°), 740 m (S-Pol at 1.5°), and 600 m (CSU-CHILL at 0.7°) above ground (Fig. 2.1b). Non-meteorological targets were filtered out from the radar data based on the values of horizontally polarized transmitted power, ρ_{HV}, and LDR for the radar-disdrometer comparisons.

The 2-D video disdrometer (Fig. 2.2) consists of two line-scan cameras providing front and side views of hydrometeors falling into the instrument with each camera having a single line of 700 photo-detectors positioned opposite a light source (Fig. 2.3). Hydrometeors falling through the 10 cm by 10 cm measuring area block the light source, shadowing some photo-detectors at a horizontal resolution of 0.15 mm. The number of blocked photo-detectors is recorded for each camera at a frequency of 51.2 kHz. Vertical resolution typically varies between 0.03 mm (snowflakes) and 0.1 mm (rain drops) depending on particle fall speed. The sampling creates image projection slices of the hydrometeors. Together with the height of the light beam, the total volume of the individual image slices gives an estimate of the particle volume.

Information provided on individual hydrometeors includes silhouette images, equivolumetric diameter, height and width information from each camera, and the particle terminal velocity. Equivolumetric diameter is computed from the particle volume, and particle terminal velocity is deduced from the vertical distance between the two camera planes and the time the hydrometeor takes to settle through each plane (Fig. 2.3). Raindrop axis ratio, canting angle, and horizontal velocity can also be obtained with the instrument. The disdrometer is equipped with temperature and wind sensors. Further description of the disdrometer is found in Kruger and Krajewski (2002) and Thurai and Bringi (2005).

The wind affects disdrometer measurements (Nespor et al. 2000). Typically, wind speed greater than about 4-5 m s^{-1} significantly influences the measurements of ice particles. To minimize the wind effects, the disdrometer can be placed inside a wind shield. However, wind shields were not used during the WISP04. Because wind speeds were 5 m s^{-1} and less during the study period on 20 February and less than 4 m s^{-1} on 5 March 2004, the disdrometer may have experienced some undercatchment. In datasets with the wind effects, the fall velocities are generally noisy due to an increase in the number of mismatched particles in the two cameras, and the positions at which the particles intersect the virtual measurement surface as they fall into the disdrometer are not uniformly distributed. These effects were not significant enough to affect the present datasets.

A wind profiler was located at Platteville, CO. A radiometer was located at the Marshall field site and gave estimates of temperature and relative humidity. Special

rawinsondes launched from the Marshall field site and the routine soundings from the National Weather Services at Denver provided upper-air measurements.

Table 2.1: Locations of the measurement sites used in this study. The range and azimuthal direction are in respect to the S-Pol radar site.

Instrumentations (location)	Elevation (km MSL)	Range (km)	Azimuth (degree)
NCAR S-Pol radar Radiometer (Marshall field site)	1.742	0	0
Disdrometer (Erie, CO)	1.521	18.80	41.6
Wind profiler (Platteville, CO)	1.540	29.81	57.0
CSU-CHILL radar (Greeley, CO)	1.432	72.74	40.8

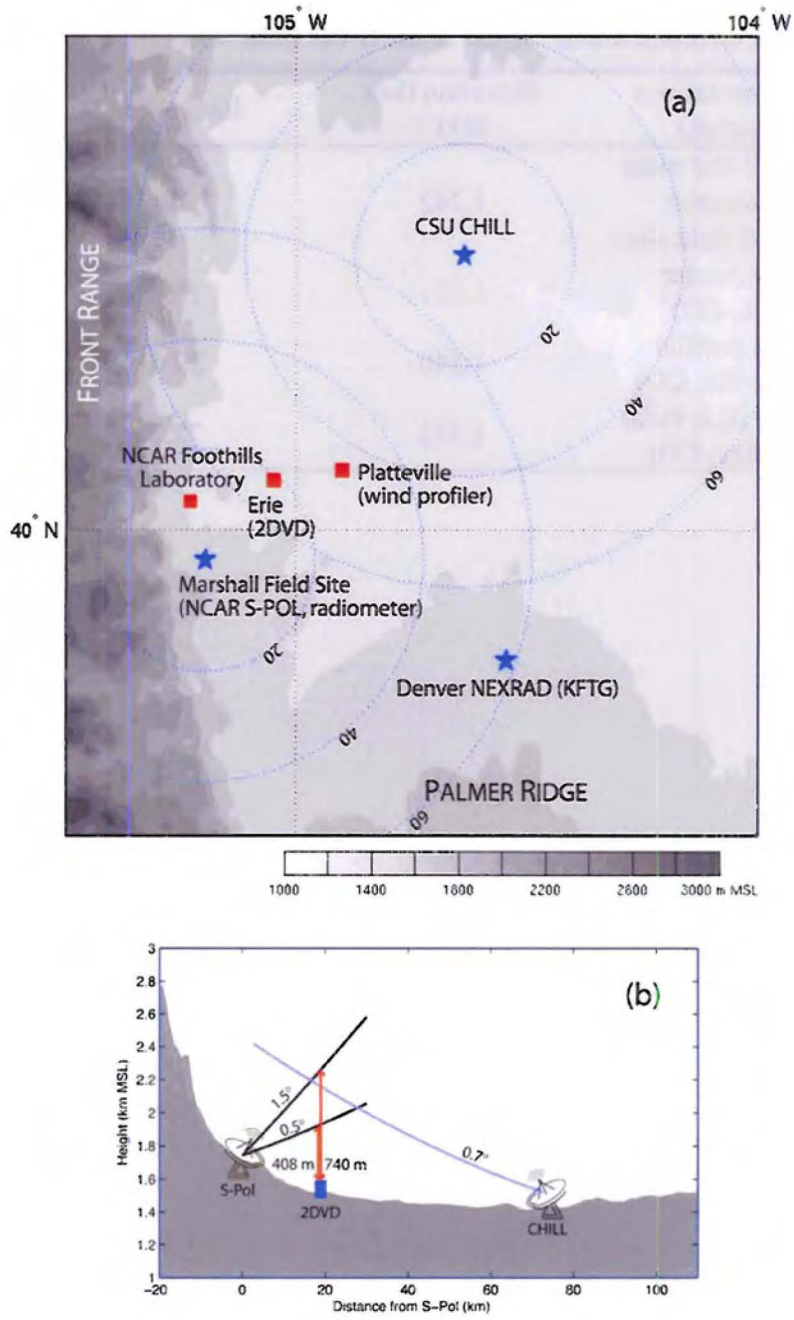

Figure 2.1: (a) Topographic map of the WISP04 study area showing the elevation (kilometers) in grayscale. Stars are radar sites, and squares indicate the measurement sites used in this study (Table 2.1). Range rings are in increments of 20 km. (b) Terrain profile of a cross-section through the S-Pol and CSU-CHILL radar sites with an illustration of the radar beams passing over the disdrometer site at antenna elevation angles indicated (black and blue lines). Also indicated are the heights of the radar beams above the disdrometer (red double arrows).

Figure 2.2: Photograph of the 2-D Video disdrometer.

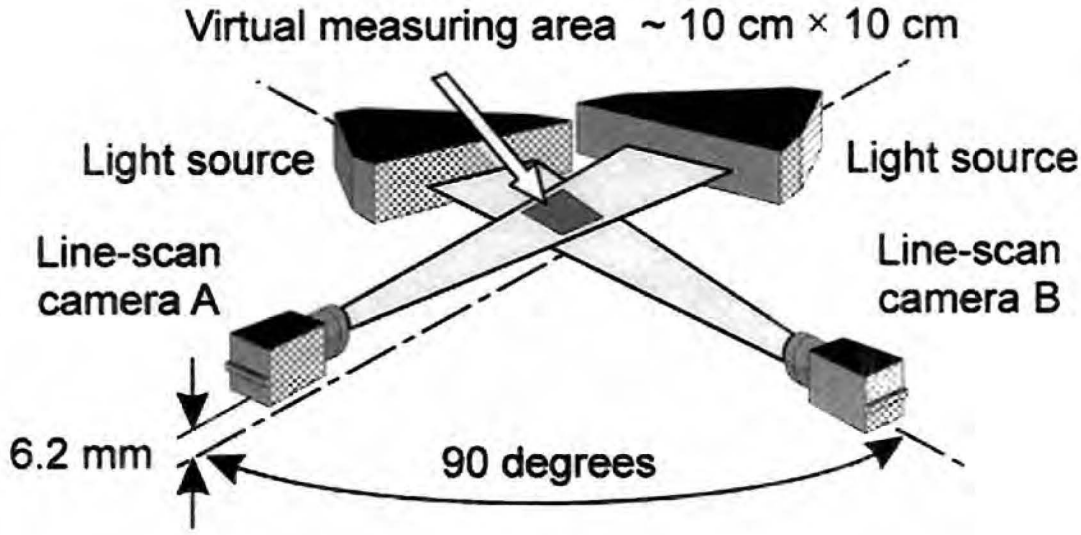

Figure 2.3: A schematic of the virtual measuring area, two line-scan cameras and their light source that are positioned 90 degrees from each other [from Kruger and Krajewski (2002)]. The instrument was calibrated and the distance between the two sheets of light (generally 6.2-7.0 mm) was measured at the beginning of the WISP04 field project. The height offset is used by the data acquisition software to compute particle terminal velocities.

Equation Chapter 3 Section 1

CHAPTER 3

COMPUTATIONAL METHOD

Radar reflectivity at horizontal (H) and vertical (V) polarization can be computed from

$$Z_{H,V} = \frac{4\lambda^4}{\pi^4 |K_w|^2} \sum_{i=1}^{M} N(D_i) |S_{H,V}|^2 \Delta D \qquad \left[mm^6 m^{-3} \right] \tag{3.1}$$

where λ is the radar wavelength, K_w is the dielectric factor of water, $N(D_i)$ is the size distribution for the *i*-th size category having an equivalent diameter (mm) between D_i and $D_i + \Delta D$, M is the total number of size categories, and $| S_{H,V} |$ is the backscattering amplitude at horizontal and vertical polarization (see e.g., Bringi and Chandrasekar 2001; Zhang et al. 2001). The backscattering amplitudes and radar cross-section ($\sigma_{H,V}$) are related by

$$\sigma_{H,V} = 4\pi |S_{H,V}|^2 . \tag{3.2}$$

For the study presented here, the disdrometer data were discretized into size categories of 0.2 mm over the range of 0.1-20.1 mm for ice particles and 0.1-8.1 mm for rain. For a given size category, the size distribution was determined from the disdrometer data by

$$N(D_i) = \frac{1}{\Delta t \cdot \Delta D} \sum_{j=1}^{M_i} A_j v_{t,j} \qquad \left[m^{-3} mm^{-1} \right] \tag{3.3}$$

where Δt is the integration time length, A_j is the effective measuring area of the j-th particle, $v_{t,j}$ is the terminal velocity of the j-th particle, M_i is the number of particles in the i-th size category. In this study, Δt is 5 minutes. The differential reflectivity (Z_{DR} in dB) is computed based on Eq. 1.2.

The scattering amplitude is computed with the T-matrix method (Barber and Yeh 1975; Vivekananden et al. 1991) which takes into account the scattering behaviors of nonspherical dielectric bodies in both the Rayleigh and Mie scattering regimes. Input parameters include the dielectric constant, particle shape (e.g., aspect ratio), and temperature. For rain, these parameters follow Zhang et al. (2001).

Properties of ice particles are complex. Aspect ratios and bulk densities continuously change throughout storm evolution making computations of the scattering amplitudes less straight forward. In this study, the particles are assumed to be oblate spheroids and fall with their major axis along the horizontal. The aspect ratio (vertical divided by horizontal) is fixed at 0.7, as a first step, for the comparisons between the computed and measured radar parameters (sections 4.4 and 5.4). Calculations using various aspect ratio will be examined in Chapter 6. For simplicity, the effects of the canting angle distribution of the particles are considered negligible.

Ice particles were considered as a two-phase material of ice and air. The effective dielectric constant (ε_{eff}), which is a function of ice particle bulk density (ρ_s), was derived using a relationship between ρ_s and the equivalent volume diameter of ice particles (D in millimeter) given by

$$\rho_s(D) = 0.178 D^{-0.922} \qquad \left[g\, cm^{-3} \right], \tag{3.4}$$

and the Maxwell-Garnett mixing formula (Ishimaru 1991; Bringi and Chandrasekar 2001) defined as,

$$\varepsilon_{eff} = \varepsilon_1 \frac{1+2fy}{1-fy} \tag{3.5}$$

for

$$y = \frac{\varepsilon_1 - \varepsilon_0}{\varepsilon_1 + 2\varepsilon_0} \tag{3.6}$$

and

$$f = \frac{\rho_s}{\rho_i} \tag{3.7}$$

where $\varepsilon_1$is the permittivity of ice, ε_0 is the permittivity of air, and ρ_i is the density of solid ice (0.92 g cm^{-3}). Equation 3.4 is an empirical relationship between ice particle bulk density and size found by Brandes et al. (2006) based on disdrometer data collected at the Marshall field site during winter seasons (October-April) between 2003 and 2005 (Fig. 3.1). Ice particle bulk density was computed using 5-minute measurements of the total precipitation volume from the disdrometer and mass from onsite precipitation gauges. Each data point in Fig. 3.1 contains more than 1000 ice particles and was collected in winds less than 2 m s^{-1}. All instruments were located inside wind shields that reduce wind speeds by a factor of 2 or greater (Scott Landolt, personal communication), and the dataset contains both rimed and unrimed ice particles. As will be shown later, the data closely follow the inverse relation between size and density found by Holroyd (1971) from ground-based observations of unrimed snowflakes. By using a size-dependent relationship, the scattering amplitudes allow for a variation in bulk ice particle density that is anticipated to occur with storm evolution. Note that the computed scattering

amplitudes do not represent melting or wetted particles. Modeling of melting ice particles can be found in Meneghini and Liao (2000) and Zawadzki et al. (2005), but they are not utilized in this study.

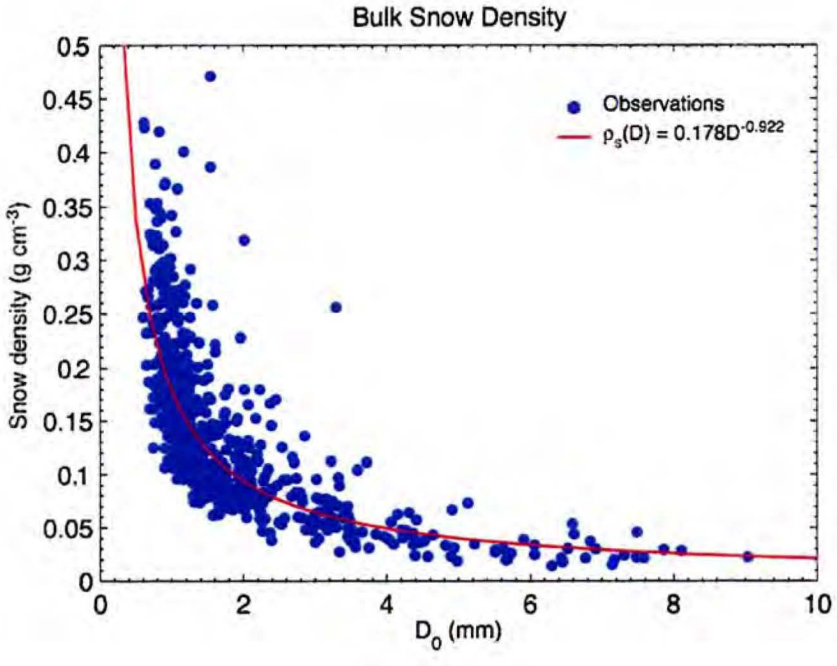

Figure 3.1: Relation between bulk ice particle density (ρ_s) and equivalent median volume diameter (D_0). Data points are from particle size distributions averaged over 5 minutes. The red line is a power-law relation through the data points used in this study.

Equation Chapter 4 Section 1

CHAPTER 4

20 FEBRUARY 2004

4.1 Weather conditions

Weak orographic precipitation developed behind a low pressure system on 20 February 2004. The surface low pressure center, associated with a 500-mb trough, was over northeastern Colorado at 1200 UTC on 19 February 2004 (Fig. 4.1a) and moved southeastward to Oklahoma by 0000 UTC on 20 February 2004 (Fig. 4.1b). The north-northeasterly wind on the backside of the surface low produced a shallow upslope orographic cloud over the study area as evident in the 0000 UTC Denver sounding on 20 February 2004[1] and the wind profiles from Platteville (Figs. 4.2-4.3). Behind the surface low, the winds varied between northerly and north-northeasterly between the surface and 600 mb level (4.0 km MSL; approximately 2.5 km deep). Winds from these directions are upslope onto the Palmer Ridge in Colorado, and are effective in producing precipitation over the Boulder-Denver corridor (Mahoney et al. 1995; Bernstein 2000). Above the upslope airmass, the atmosphere was at neutral stability, and the northwesterly and westerly flow associated with the upper-level synoptic features dominated.

The time-height cross-sections of the radiometer and wind measurements show a gradual moistening of air at low levels toward 0000 UTC on 20 February 2004 (Fig. 4.3a)

[1] In practice, the National Weather Service's soundings are typically released about one hour before the nominal time.

and a layer associated with the upslope flow that deepened with time with its top reaching nearly 4.0 km MSL (~2.5 km AGL) by 0300 UTC (Fig. 4.3b). The cloud layer extended into the northwesterly wind regime, above the top of the upslope airmass—a characteristic feature associated with shallow upslope precipitation over the same geographical locations documented by previous investigators (e.g., Boatman and Reinking 1984; Herzegh and Conway 1986; Rasmussen et al. 1995). The deepening upslope cloud layer was associated with the formation of a northerly barrier-jet (Marwitz 1983, 1987; Parish 1986). The barrier-jet is evident in the wind profiler measurements between 2 and 3 km MSL after 0000 UTC (Fig. 4.3b). Although the RHI scans were not parallel to the low-level winds, the radial Doppler velocity also depicted the enhancement of the low level flows (not shown). The barrier jet formation was accompanied by a rapid lowering of the melting level from 2.5 km MSL to 1.8 km MSL starting just before 0000 UTC (Fig. 4.3a) and a transition from rain to mixed-phase precipitation at the disdrometer site. Since there was no cold air advection behind the low pressure center at 0000 UTC, a sudden descent of the 0°C level may be attributed to a diabatic cooling of melting ice crystals leading to a pressure field perturbation similar to a winter storm studied by Marwitz and Toth (1993) over the same geographical region. As in Marwitz and Toth's case, the surface layer moistened shortly after the onset of precipitation (Fig. 4.3a) and the intensification of the barrier jet coincided with the intensification of precipitation at 0030 UTC.

The storm system produced a short period of precipitation over the study area, with the precipitation starting as light scattered rain over the Front Range region by 2000 UTC on 19 February 2004. At the disdrometer site, light rain began at 2200 UTC on 19

February 2004 and the surface air cooled to 4°C by 2330 UTC as the rain developed (Fig. 4.4). Subsequently, the surface air saturated, and the temperature decreased to 2°C. Afterward, the temperature was between 0.5 and 2°C at the disdrometer site during the precipitation event. Most of the time, the precipitation was mixed-phase[2]. The precipitation ended by 0200 UTC as the low pressure center further advanced eastward. A more detail discussion of the precipitation will be provided in the subsequent section.

4.2 Precipitation: the 2-D Video disdrometer observations

Table 4.1 summarizes precipitation observed by the disdrometer and the author. The author was present at the disdrometer site at the beginning of the precipitation event, and then drove between the disdrometer site and the NCAR Foothills laboratory (Fig. 2.1) between 0000 and 0100 UTC. Figure 4.5 shows scatter plots of observed terminal velocity and diameter at various stages of the precipitation event, and example images of the ice particles.

Light rain continued from 2200 UTC on 19 February 2001 to 0030 UTC the next day (Period A; Fig. 4.5a), and a mixed-phase precipitation (Period B; 0030-0100 UTC) followed a rapid decrease in temperature (section 4.1). Figure 4.5b shows that most of the observed particles were raindrops during Period B, but the field notes indicate that some of them were not completely melted (opaque raindrops). Afterwards, a brief period of mixed-phase precipitation dominated by large snow aggregates occurred (Period C; 0100-0115 UTC) due to the warm moist air at low levels (Figs. 4.3-4.4). The last period

[2] Mixed-phase precipitation refers to a rain-snow mixture in this study. Note that precipitation on 20 February 2004 included some melting snow particles, however.

of the precipitation event produced a mixture of raindrops and snow grains or irregularly shaped particles (Period D; 0115-0200 UTC). Figure 4.5d shows the ice particles having slower terminal velocity compared with that expected for raindrops of the same diameters.

Time histories of the particle size distribution parameters are shown in Fig. 4.6. Here, particle distributions were fit with the gamma based function (e.g., Ulbrich 1983)

$$N(D) = N_0 D^{\mu} e^{-\Lambda D} \quad [m^{-3}], \tag{4.1}$$

where N_0 ($mm^{-\mu-1}$ m^{-3}) is a number concentration parameter, μ is a shape parameter, and Λ (mm^{-1}) is a slope. The governing parameters were determined from the 2nd, 4th, and 6th moments of the observed particle distribution using the truncated-moment method (Vivekanandan et al. 2004). The n-th moment is given by

$$M_n = \int_{D_{\min}}^{D_{\max}} D^n N(D) dD, \tag{4.2}$$

where the limits of integration are truncated at the minimum (D_{min}) and the maximum (D_{max}) size categories of the observed particles. In the truncated- and non-truncated [i.e., the integration is from 0 to infinity (e.g., Kozu and Nakamura 1991)] moment methods, the distribution parameters N_0, Λ, and μ are determined to be such that the three chosen moments of the observed distributions are conserved. The figure shows that during the rain period (Period A), both μ and Λ are large (> 10 and > 15 mm^{-1}, respectively)—characteristic of light rain. Increasing trends in the two parameters indicate that the rainfall rate decreased over time.

The onset of the first mixed-phased period (Period B) is associated with a broadening of the particle size distribution (PSD) shown by a rapid decrease in μ to –2

and Λ to nearly 0 mm^{-1}. Consequently, the equivalent median volume diameter (D_0) increased to 2.98 mm from an average raindrop D_0 of 0.88 mm (Fig. 4.6b). The values of μ and Λ essentially show no variation during the subsequent two mixed-phase periods (Periods C-D). However, the values of D_0 were > 4 mm and the maximum diameter (D_{max}) was > 6 mm during Period C due to the presence of aggregates while the irregular particles were mostly less than 2 mm (Period D). PSD parameters are not shown for times after 0145 UTC in Fig. 4.6 because the precipitation weakened (< 80 particle counts per 5 minute).

4.3 Radar observations

Radar data were characterized by pronounced snowbands oriented in the northwest-southeast direction that slowly propagated southeastward with time, as evident in the PPI scans performed by the CSU-CHILL radar (Figs. 4.7-4.8). These snowbands were likely associated with instabilities released by convective generating cells[3] (Carbone and Bohne 1975; Hobbs et el. 1980; Herzegh and Conway 1986) embedded in the upper northwesterly flow. The presence of convective vertical motions associated with the generating cells can be inferred from narrow banded structures in the radial Doppler velocity field indicative of converging/diverging flow (Fig. 4.7, right column). Over time, the snowbands became less defined (Figs. 4.7d).

Precipitation streaks originating from the generating cells were produced due to vertical wind shear, including the directional shear between the upslope layer and the

[3] Generating cell/region is defined in the Glossary of Meteorology as "a small region of locally high reflectivity from which a trail of hydrometeors originates."

northwesterly regime aloft. The average shear was 8 m s^{-1} km^{-1} between the surface and the cloud top with the maximum shear of 16-18 m s^{-1} km^{-1} from 3 to 4.5 km between 00 and 01 UTC. The precipitation streaks tilted more horizontally as the low-level jet strengthened, carrying precipitation particles in the upslope layer further upshear.

Generally, the precipitation streaks were associated with Z_H greater than 10 dBZ and Z_{DR} of 1 dB or less (Fig. 4.8). The values of Z_H are relatively small and those of Z_{DR} are slightly higher between the fall streaks. The combination of relatively low Z_{DR} (< 1 dB) and high Z_H (> 10 dBZ) within the precipitation streaks aloft suggests the presence of low density snow aggregates (e.g., Vivekanandan et al. 1993). The polarimetrically-derived particle designations (PID; Vivekanandan et al. 1999) suggest dry snow (light blue) associated with the snow bands, as expected, while irregular ice crystals (light pink) are designated in between the snow bands (Fig. 4.8). The PID criteria for dry snow and irregular ice particles essentially differ only in the reflectivity. Thus, the particle designations basically indicate that particles between the fall streaks were generally smaller than those within the streaks. The PID algorithm in part depends on the temperature profile. In this case, the temperature profiles based on the radiometer measurements were used.

As in the present case, Field et al. (2004) found pronounced precipitation streaks and anticorrelated patterns between Z_H and Z_{DR} with the Chilbolton Advanced Meteorological Radar in a mixed-phase cloud. Comparisons of the radar data and observations with a research aircraft carrying a 2-D C probe and a Small Ice Detector (Field et al. 2004) revealed the presence of well-developed dendrites in regions of large Z_{DR} and low Z_H, and aggregates associated with the generating regions and precipitation

trails. The formations of the dendrites were explained by the fact that the entire cloud layer was mixed-phase within the planar-growth temperature range, thereby favoring the depositional growth mode. In a study of rainbands over the Washington Cascades, Herzegh and Hobbs (1980) attributed the presence of different ice particle types inside and outside of the generating regions to fluctuations in supersaturation. They found that generating regions were supersaturated with respect to water, allowing rapid ice crystal growth through deposition and accretion, while the air was subsaturated with respect to water outside of the generating regions at the same temperature, leading to a slower depositional growth rate. Similar conditions as found in the two studies may apply to the 20 February case.

Another interesting feature in Fig. 4.8a is the large Z_{DR}, between 1.8 and 4 dB, found in a region of weak Z_H (< 5 dBZ) embedded in the upper northwesterly flow between two generating cells (heights between ~3.7 and 4.7 km MSL; referred to as the peak-Z_{DR} region, hereafter). Large values of Z_{DR} associated with small Z_H are an indication that the particles were horizontally oriented pristine ice crystals (e.g., Hall et al. 1984; Vivekanandan et al. 1993; Vivekanandan et al. 1994; Straka et al. 2000). Consistently, the PID algorithm identified pristine ice crystals (dark blue) (Fig. 4.8a). Perhaps planar ice crystals, such as hexagonal plate and crystals with broad branches (e.g., sector plates), were present as they are expected to form at the measured temperatures between –14 and –19°C for cloud supersaturated with respect to ice (Magono and Lee 1966) based on the 0000 UTC Denver sounding (Fig. 4.2). Such a Z_{DR} pattern was reported by Hogan et al. (2002) at a temperature of -15°C. They attributed this to a water-saturated updraft reaching near the cloud top for a period of time.

Figure 4.9 shows a sequence of radar measurements associated with the peak-Z_{DR} region, which initially spreads over a range of 16 km at 0032 UTC (A in Fig. 4.9a). With a formation of a weak convective turret at ranges 20-23 km by 0044 UTC, the values of Z_{DR} near these ranges were reduced (Figs. 4.9b-c). Perhaps aggregation or riming of the ice crystals occurred such that the ice crystals became less pristine, thereby reducing Z_{DR}. The peak-Z_{DR} region weakened with time and the signature of pristine ice crystals was eventually lost. Later, another peak-Z_{DR} region appeared (B in Fig. 4.9d), but the signature was much weaker compared with the one earlier.

Strong spatial gradients in radar reflectivity at horizontal or vertical polarization interfering with the side-lobes can also produce high values of Z_{DR} (Herzegh and Conway 1986). That is, although backscattering from the scatterers within the main lobe may be weak, the side lobes "see" nearby strong scatterers and produce anomalously large Z_{DR}. Beam mismatches between the vertically and horizontally polarized components could also cause such an anomaly. Because the observed peak-Z_{DR} regions evolved with time, it was determined that this was not an artifact from the side lobe seeing ground targets. Additionally, there were no significant horizontal reflectivity gradients in this region indicating that the horizontal gradients in Z_H did not affect the Z_{DR} measurements. However, the chance of Z_{DR} contamination cannot be ruled out entirely because the vertical gradients were about 8-10 dBZ km^{-1} due to the presence of the fall streaks.

Figure 4.10 shows time-height cross-sections of radar measurements and the PID field corresponding to the disdrometer site. The cross sections were produced from successive RHIs by making vertical profiles of the measurements, which were averaged over 2 km in the horizontal centered at the disdrometer site and over a depth of 0.4 km at

every 0.1 km. Contoured on each plot are Z_{DR} > 0.5 dB in increments of 0.25 dB. The most frequently designated hydrometeor type at each height level is shown in the PID field. Vertical structures are complex due to a significant directional wind shear above the upslope airmass. Nevertheless, the previously-discussed peak-Z_{DR} regions being classified as pristine ice crystals and a slanted band of maximum Z_H (> 18 dBZ) depicting a single precipitation streak passing over the disdrometer site (*cf.* Fig. 4.8) are shown. Comparisons between the disdrometer observations and Fig. 4.10 allows for associating the mixed-phase precipitation dominated by snow aggregates (Period C) with the precipitation streak, as well as the mixed-phase precipitation dominated by rain with the region of light precipitation that followed the passage of the precipitation streak.

4.4 Comparisons of the measured and calculated Z_H and Z_{DR}

Figure 4.11 shows time histories of radar-measured and disdrometer-based computations of Z_H and Z_{DR} using the computational method described in Chapter 3. Solid lines are the radar parameters computed assuming that all particles are either rain (green) or frozen particles (black). Mixed-phase precipitation was partitioned into rain and ice-particle categories using particle terminal velocity (Fig. 4.5), and radar parameters for the two precipitation types were individually calculated (dashed lines in Fig. 4.11). Here, hydrometeors were considered raindrops when the terminal velocities were within 40% of the empirical relationship for raindrops found by Brandes et al. (2002); whereas, particles falling slower than the threshold were assumed ice particles. Although this method does not completely separate raindrops and ice particles especially

at small sizes, the radar parameters based on the partitioned particle datasets roughly represent contributions from raindrops and ice particles to the radar returns because radars are more sensitive to large particles.

The radar measurements shown in Fig. 4.11 correspond to average measurements over a 1-km radius circle centered at the disdrometer site. The standard deviation of the Z_H and Z_{DR} values were 2-3 dBZ and 0.2-0.4 dB, respectively. For a radar-disdrometer comparison, trajectories of particles were taken into account due to the presence of pronounced sheer-induced precipitation streaks. Because winds were unidirectional below the elevation of the 1.5° PPI scans at the disdrometer site, particle trajectory was computed based on a simple geometrical analysis following Marshall (1953). In this method, the trajectory of a particle sampled by the disdrometer is followed in a backward sense to the locations of cloud where radar beams from the 0.5 and 1.5° antenna elevations intersect, using the formula

$$\Delta x = \frac{dU/dh}{2v_t} h^2 . \tag{4.3}$$

In the equation, Δx and h are the relative horizontal and vertical distances traveled by the particle, with dU/dh the vertical wind shear, and v_t the particle terminal velocity. Vertical air motions were considered negligible within the layer considered. The assumed terminal velocity profile was based on the disdrometer observations (Fig. 4.5) and the long-term melting layer observations presented in Fabry and Zawadzki (1995), assuming particle terminal velocities of 1 m s^{-1} for the ice-layer, 1.5 m s^{-1} for mixed-phase precipitation, and 4 m s^{-1} or greater for rain depending on the observed medium volume diameters. The vertical wind shear was determined from the radial Doppler velocity for the 41° azimuth direction. Δx was in the order of 4 km (9 km) with the associated time

lag of about 7 (12) minutes for *h* corresponding to the 0.5° (1.5°) elevation angle while snow aggregates dominated the precipitation during Period C.

Generally, the computed Z_H match well with the radar measurements. The correspondence between the rain-density assumed Z_H and the measurements during Period A is good, especially for the lower elevation scans. An offset of approximately 8 dBZ between the computed and measured Z_H with the 1.5° elevation scans partly comes from ice particles having a smaller dielectric factor compared to rain, because the 1.5° scans sampled precipitation above the melting layer. In Period B, calculations using raindrop scattering amplitudes generally better agree with the measurements even though the precipitation was a mixture of rain and snow. The partitioned datasets indicate that raindrops produced an average of 19 dBZ of the measured Z_H while only 10 dBZ or less were from snow aggregates. Thus, the better agreement achieved with the rain-based estimations is consistent with the backscattered radar signals from raindrops that overwhelmed those from snow aggregates due to the lower dielectric factor and the relatively low particle concentration of snow aggregates during the time segment. Later, a different result is presented for the 5 March 2004 case.

Similarly, the computed Z_{DR} are consistent with the measurements in Period B. The over estimates of Z_{DR}, when assuming all particles to be raindrops, are expected because the dielectric factor of rain is higher than snow and D_0 as large as 6 mm (Fig. 4.6b) would correspond to an oblate raindrop which causes Z_H to be much greater than Z_V. During this period, raindrops were typically 1 mm in diameter. Such raindrops would have an aspect ratio of 0.99 (Brandes et al. 2002) and theoretically produce a Z_{DR} of approximately 0.2 dB (Herzegh and Jameson 1992). Z_{DR} computed from the rain-only

dataset (green dashed line) and the measured Z_{DR} is consistent with the theory. Z_{DR} based on bulk ice particle density (total and partitioned datasets) also match the measurements because light rain and dry aggregates typically yield Z_{DR} of a similar magnitude.

The mixed-phase period dominated by snow aggregates (Period C) was short and comparisons are limited. Nevertheless, the ice particle-density based Z_H and Z_{DR} match the measurements. Recall that a precipitation streak reached the ground at the disdrometer site during this period (section 4.3). Consequently, the large snow aggregates dominated the radar returns over the small raindrops ($D < 1.4$ mm, Fig. 4.6b). Although the effect of melting ice particles and snowflakes is unclear here, the dominance of the aggregates is evident from the partitioned datasets that indicate at least 12.3-16.1 dBZ of total Z_H to be from snow while only 3.6-7.9 dBZ from rain.

As the low-level cloud layer lifted, precipitation reaching the ground decreased. During Period D the disdrometer sampled generally small snow grains or irregular particles mixed with raindrops (section 4.3). The contributions from the ice particles in this period were < -3 dBZ—approximately 10 dBZ less than those from raindrops. A better agreement between the measurements and the computed values when using the raindrop scattering amplitudes is plausible here because the ice particles were typically less than 2 mm in diameter (Fig. 4.5b) and needless to say, the dielectric factor was smaller than that of rain, thus making ice particles to be less dominant in the sample volume. Another possible reason for the smaller values of the ice-based Z_H compared with the measurements is simply that not enough precipitation reached the disdrometer because the cloud layer lifted (Fig. 4.10). An increase in the measured and computed Z_{DR}

from Period C to D perhaps reflects the change in the dominant particle type from the relatively low bulk density aggregates to raindrops.

Similar to the S-Pol measurements, the disdrometer-based radar parameters matched the CSU-CHILL measurements during the rain-snow transition period (Period B) and a brief period of mixed-phase period dominated by snow (Period C) (not shown). The calculations and measurements were not comparable in Period D because the CSU-CHILL radar sampled the elevated precipitation layer while only a small amount of the precipitation reached the ground in Period D.

Table 4.1: Summary of disdrometer observations and field notes taken by the author on 20 February 2004. Surface air temperatures were measured at the disdrometer site. The most dominant particle type (in terms of number) was determined from visual inspections of the disdrometer data. The comments section is from the author's field notes.

Time (UTC)	Hydrometer	Temperature (°C)	Comments
(A) Before 0030	Rain	2-9	Light rain
(B) 0030-0100	Mixture of rain and aggregates	0.8-2.0	Wet aggregates were present. Some opaque raindrops were also observed at the disdrometer site.
(C) 0100-0115	Aggregates with some rain	0.8	Large aggregates up to 1-2 cm in diameter were observed at the Foothills Lab.
(D) After ~0115	Mixture of rain and irregular ice particles	0.8-1.8	Essentially no aggregates.

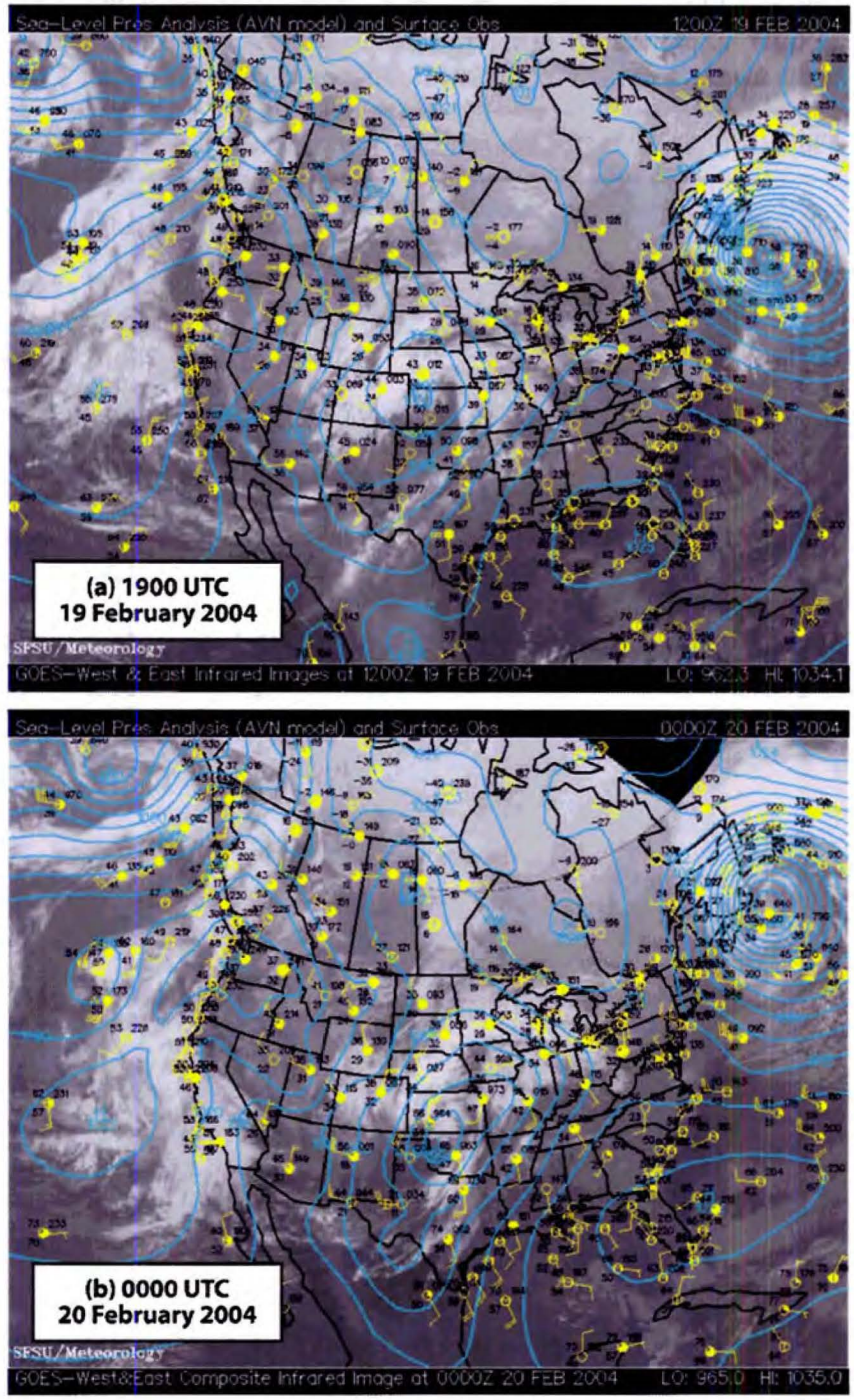

Figure 4.1: Visible satellite image and surface analysis for (a) 1200 UTC on 19 February 2004 and (b) 0000 UTC on 20 February 2004. Blue contours are isobars at a 4-mb interval. Full barbs are wind speed at 10 knots.

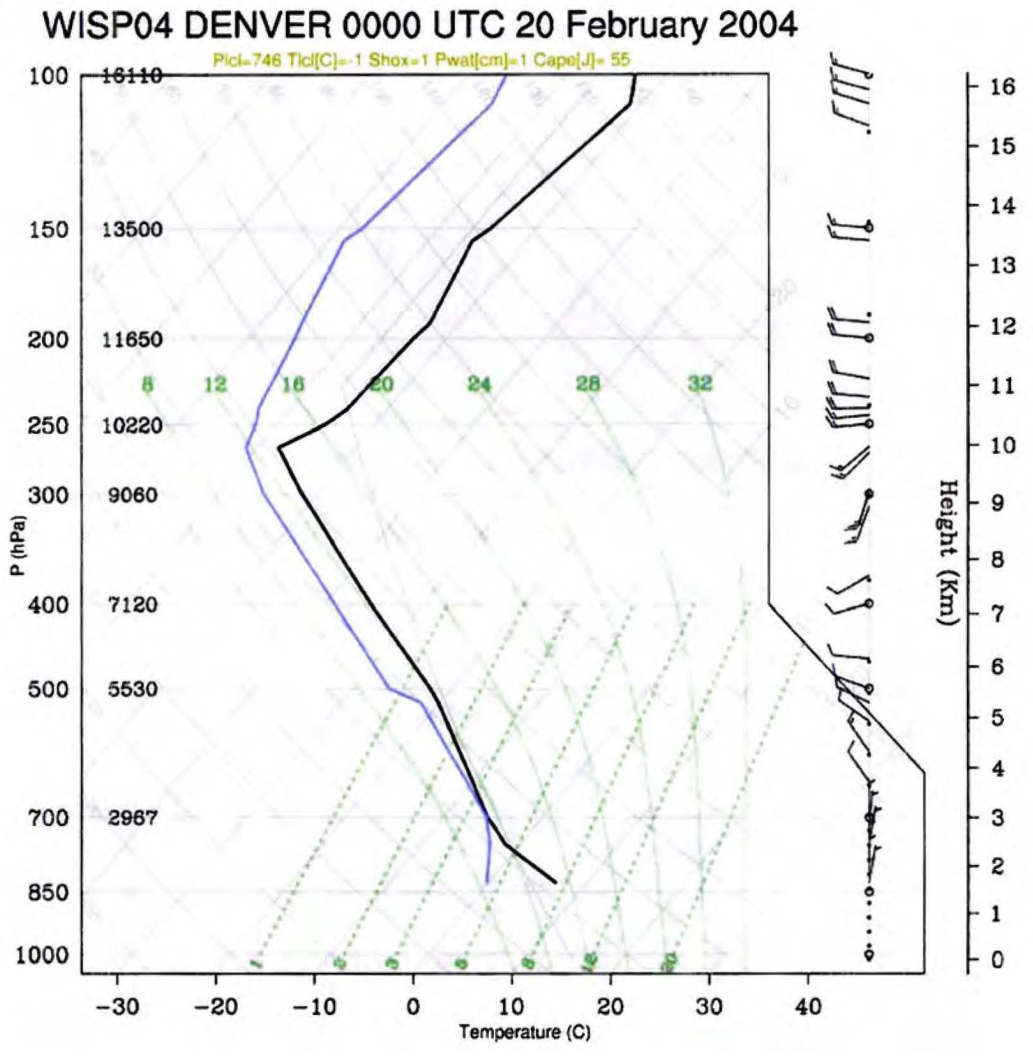

Figure 4.2: The National Weather Service (NWS) sounding from Denver for 0000 UTC on 20 February 2004. Full barbs are wind speed at 10 m s^{-1}.

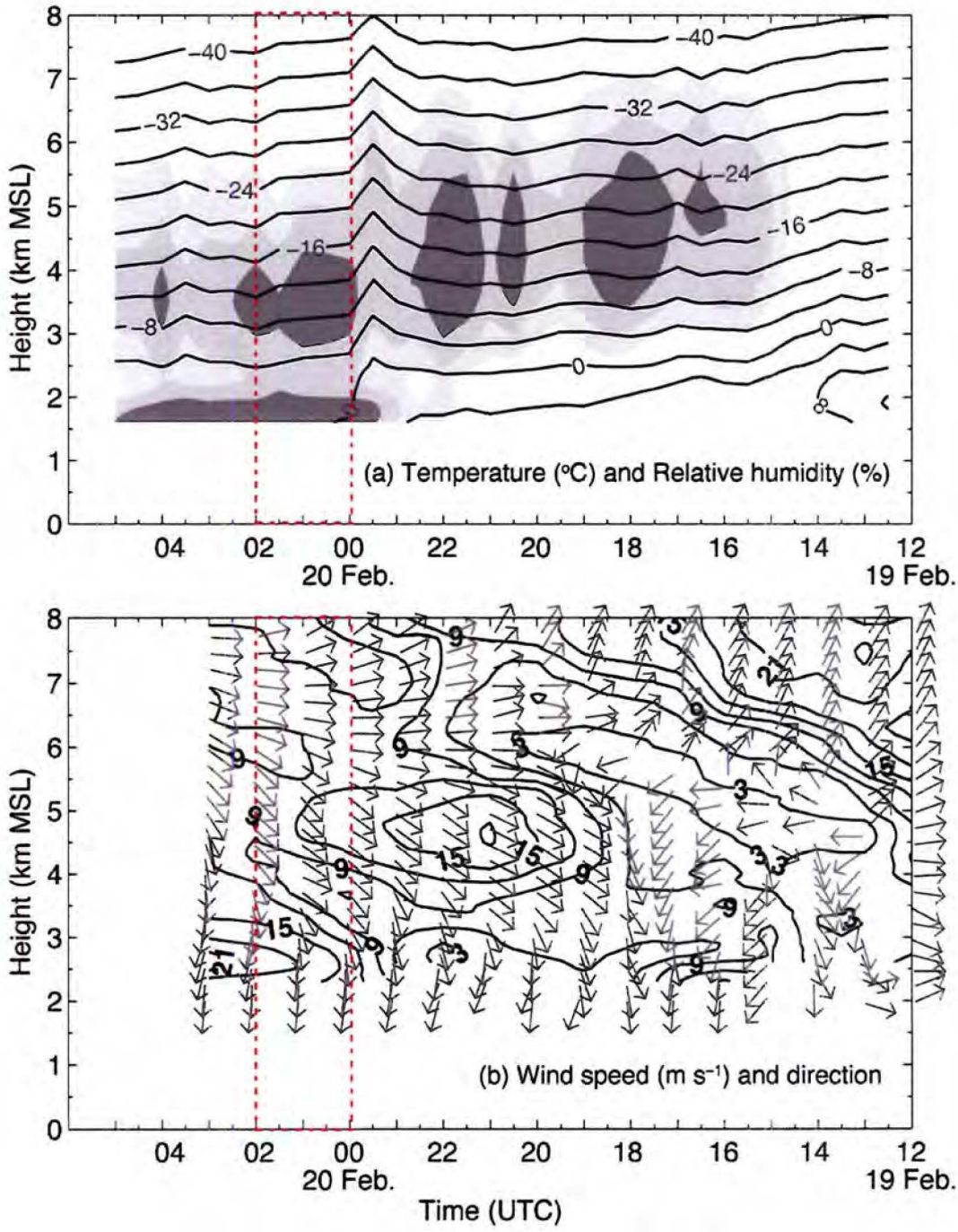

Figure 4.3: Time-height cross-sections of (a) temperature (contours) and relative humidity (grayscale), and (b) wind speed (contours) and direction (arrows) for 19-20 February 2004. In (a), relative humidity > 90% (dark), 80-90% (medium), and 70-80 % (light) are shaded. The red box indicates the study period.

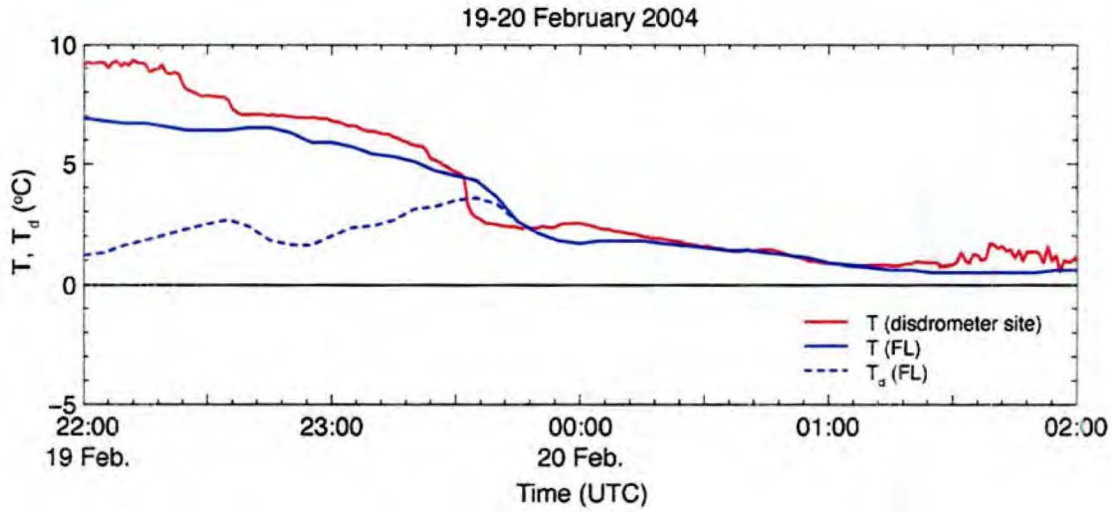

Figure 4.4: Time histories of surface air temperature (T) at the disdrometer site as well as surface air temperature and dewpoint temperature (T_d) at the NCAR Foothills laboratory (FL) for 19-20 February 2004.

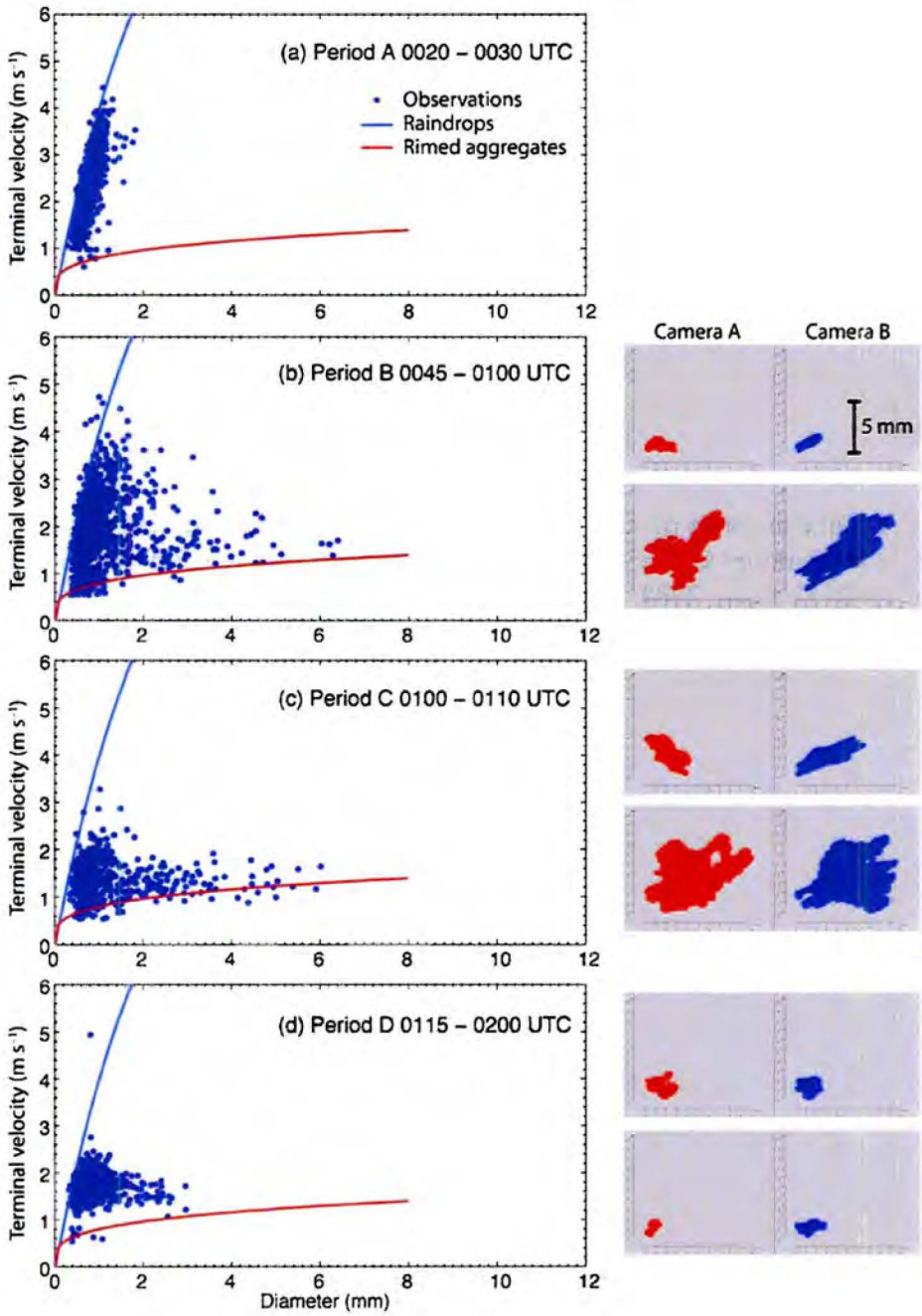

Figure 4.5: Observed terminal velocity versus equivalent volume diameter for select time segments in (a) Period A, (b) Period B, (c) Period C, and (d) Period D on 20 February 2004. Hydrometeor observations during these time periods are indicated in Table 4.1. Overlaid are the terminal velocity relations for raindrops from Brandes et al. (2002), and densely rimed aggregates from Locatelli and Hobbs (1974). Sample particle images for (b)-(d) from the two cameras are shown on the right.

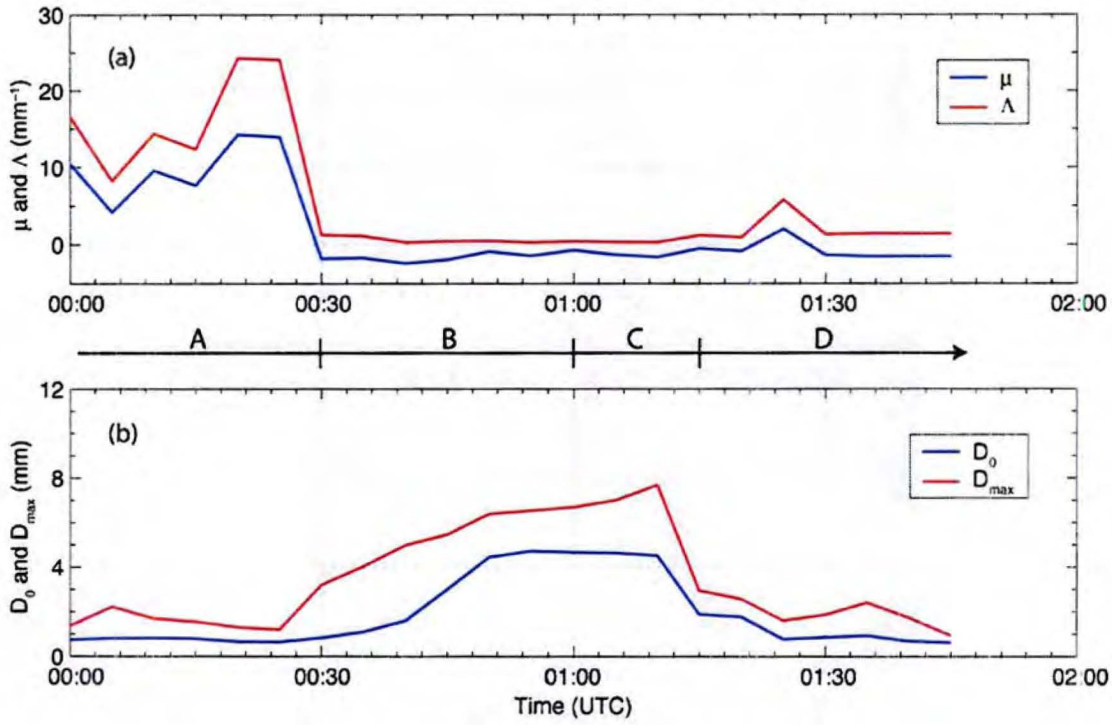

Figure 4.6: Time histories of (a) shape (μ) and slope (Λ), and (b) median equivalent volume diameter (D_0) and maximum particle size (D_{max}) from 5-minute PSDs.

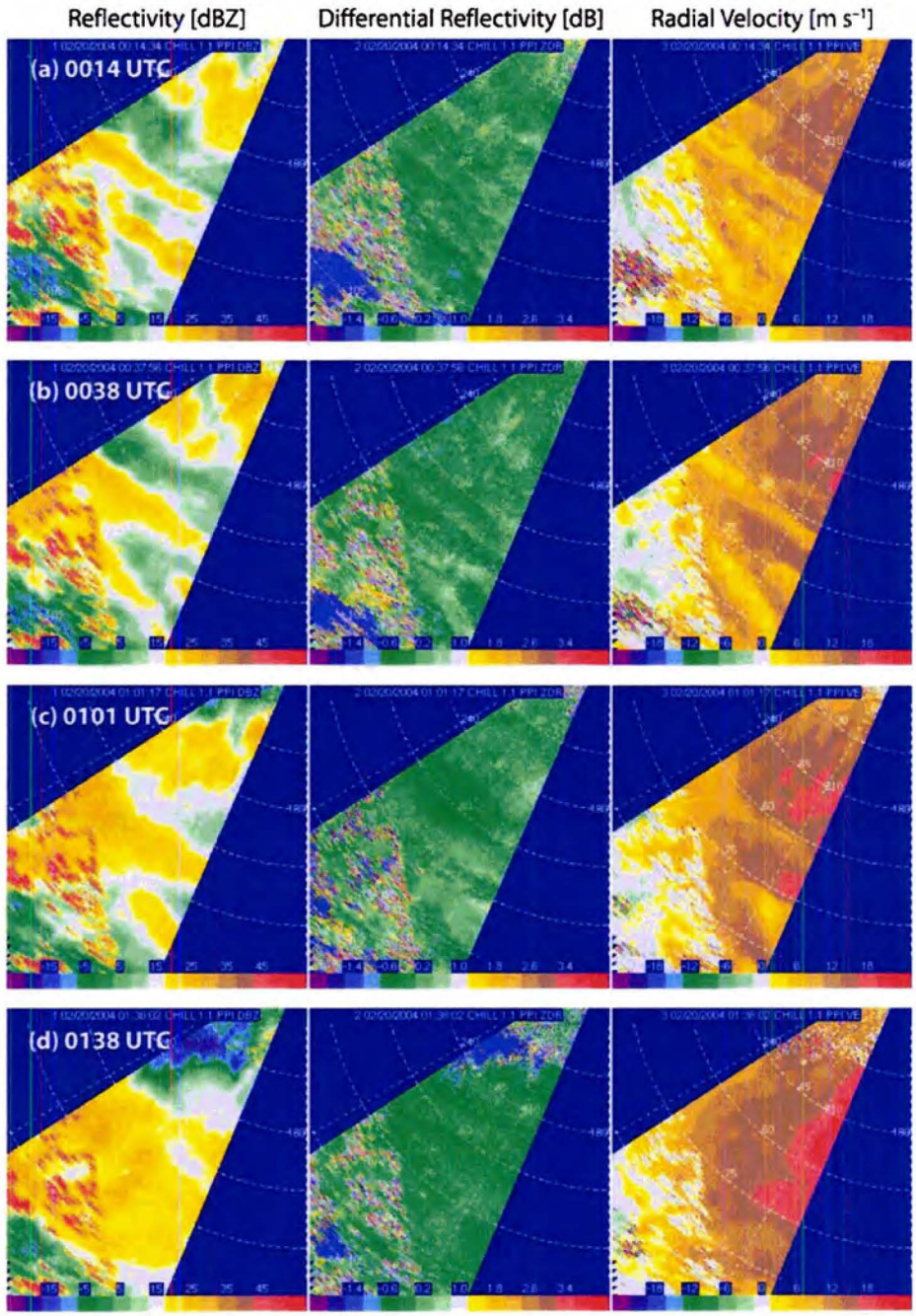

Figure 4.7: The CSU-CHILL radar measurements of Z_H (left column), Z_{DR} (center), and Doppler radial velocity (right) from the 1.1° PPI scans for (a) 0014 (b) 0038, (c) 0101, and (d) 0138 UTC on 20 February 2004. The range rings are in 15 km increments.

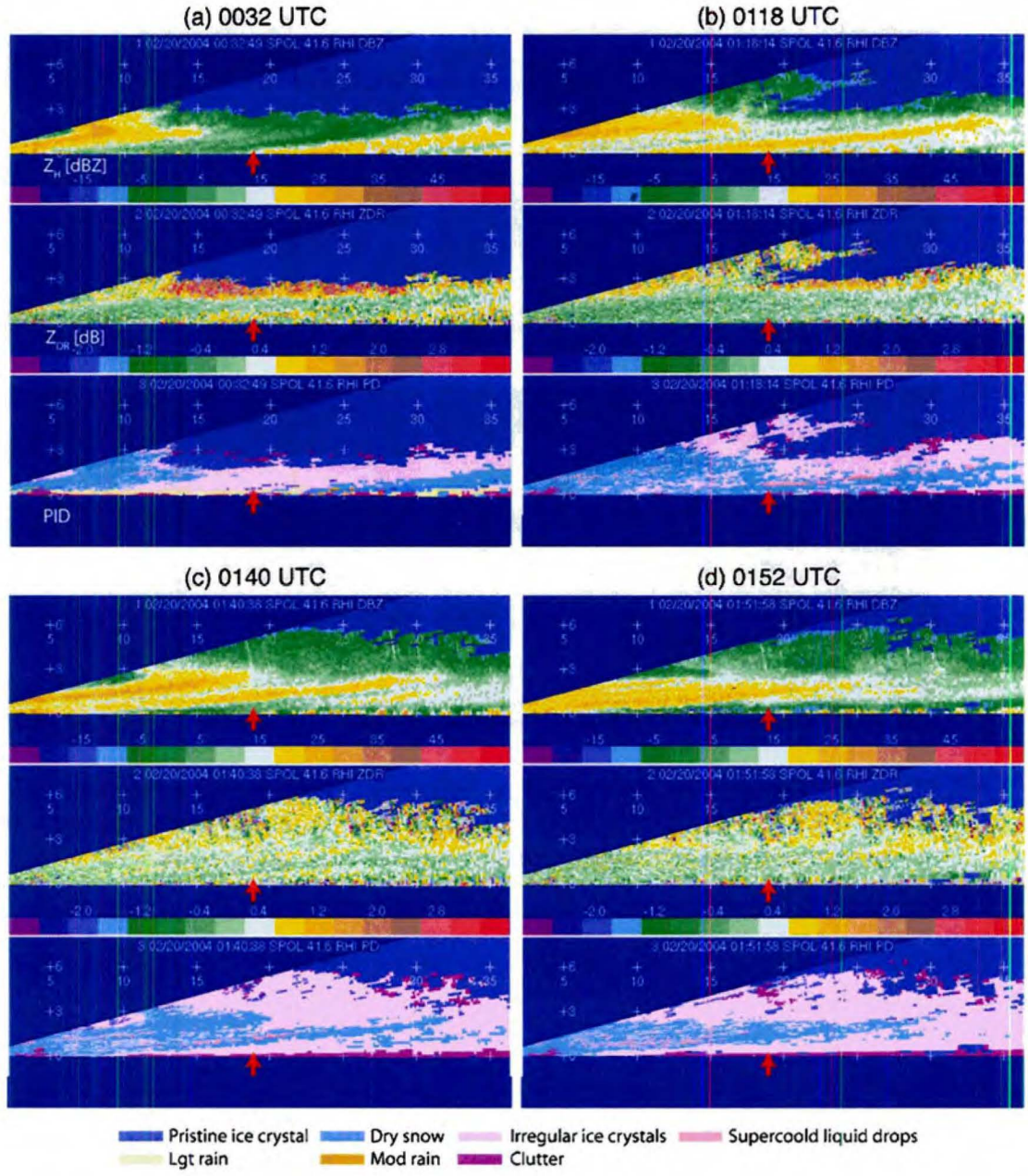

Figure 4.8: Vertical cross-sections of Z_H (upper row), Z_{DR} (middle), and PID (bottom) through the azimuth angle of 41.6° for (a) 0032, (b) 0118, (c) 0140, and (d) 0152 UTC. The measurements are from the S-Pol radar. Red arrows indicate the disdrometer location, and +'s are placed in increments of 5 km in the horizontal and 3 km in the vertical. The ordinates are in kilometers above the ground level.

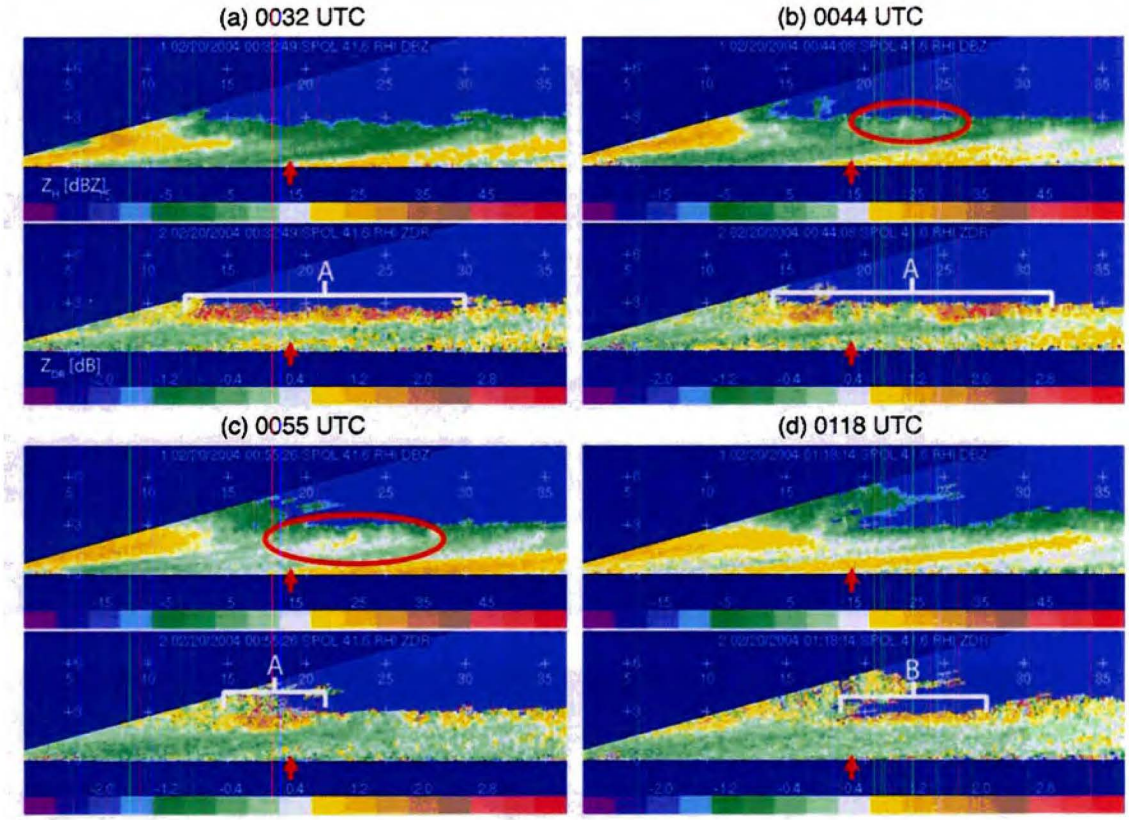

Figure 4.9: Same as Fig. 4.8 without the PID field. Radar scans are for (a) 0032, (b) 0044, (c) 0055, and (d) 0118 UTC. Red circles enclose a small turret (see text). A and B are the peak-Z_{DR} regions corresponding to those labeled in Fig. 4.10.

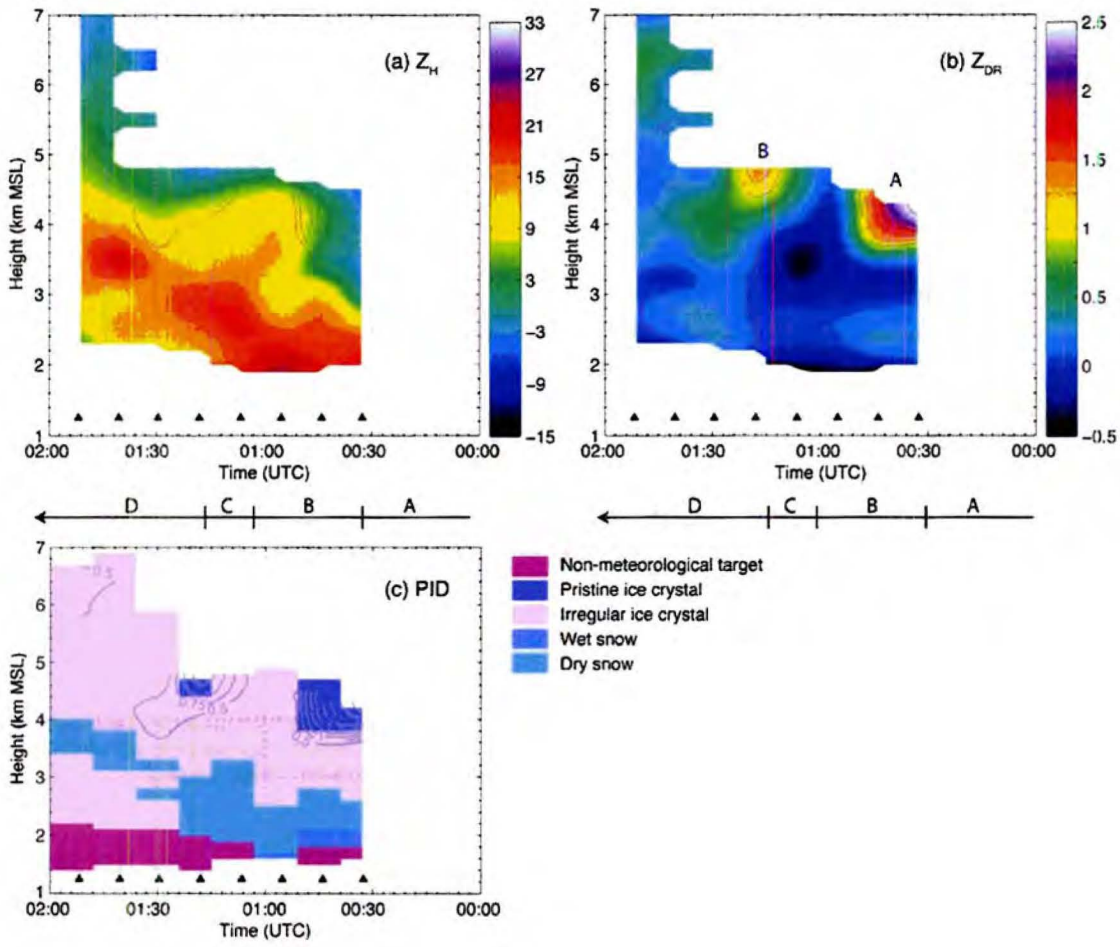

Figure 4.10: Time-height cross-sections of (a) Z_H, (b) Z_{DR}, and (c) PID for the disdrometer site. The measurements are from the S-Pol radar. Z_{DR} larger than 0.5 dB are contoured at an interval of 0.25 dB and overlaid on each frame. Time increases to the left.

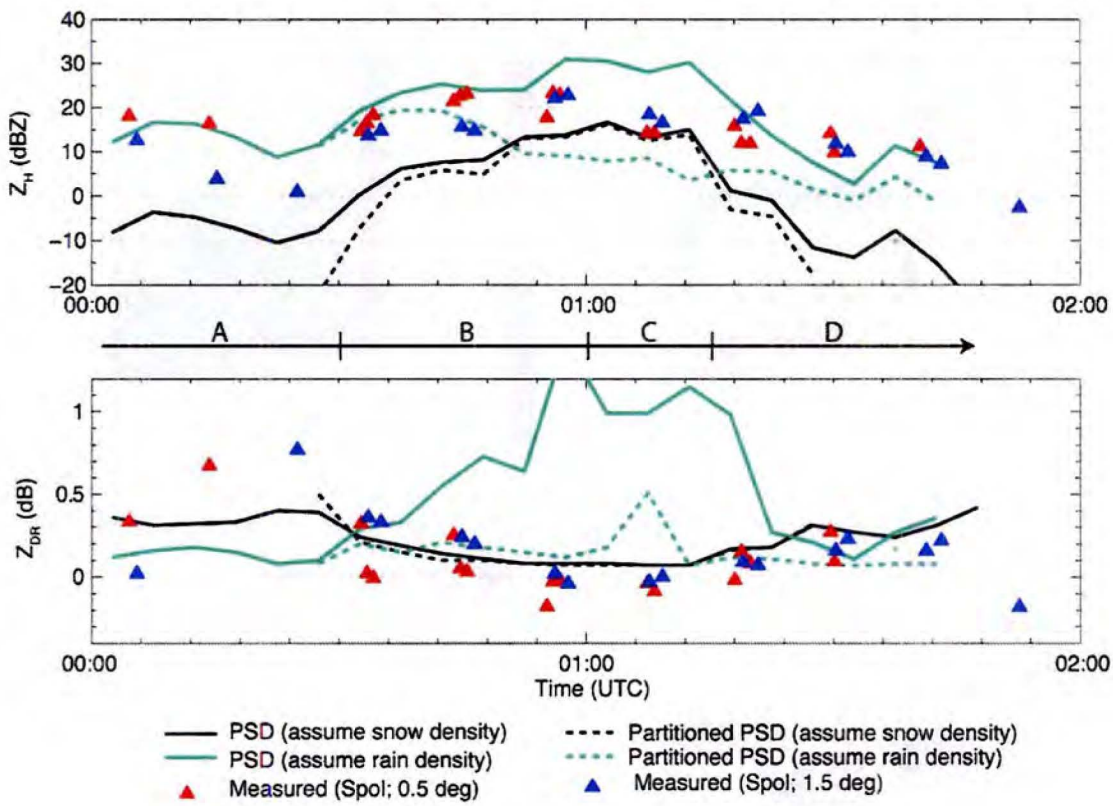

Figure 4.11: Time histories of measured and retrieved Z_H (top) and Z_{DR} (bottom). Computed radar parameters (solid and dashed lines) are based on 5-minute PSDs. Solid lines are calculated radar parameters assuming all particles are either frozen particles (black) or rain (green). Dashed lines are computations only for partial dataset for particles that were identified as frozen particles (black) or rain (green). Radar measurements (triangles) are averaged over a circular area having a radius of 1 km centered at the disdrometer site.

Equation Chapter 5 Section 1

CHAPTER 5

5 MARCH 2004

Another upslope precipitation event occurred on 5 March 2004. The S-Pol radar collected data between 0000 and 0500 UTC utilizing the same scanning strategy as the previous case. The disdrometer operated throughout the precipitation event, but the radiometer and CSU-CHILL radar data were not collected.

5.1 Weather conditions

Precipitation on 5 March 2004 over the Front Range region was dominated by a lee-side trough (Bluestein 1993) that formed on 4 March 2004 and an extratropical cyclone that passed to the south of Colorado (Fig. 5.1a). The lee-side trough developed in relation to a 500-mb short-wave trough embedded in a long-wave trough over the western United States. While the lee-side trough persisted in the eastern Colorado, the extratropical cyclone moved from northern Mexico to the central United States on 4-5 March. By 0000 UTC on 5 March 2004, the lee trough weakened (Fig. 5.1b), but remained in northeastern New Mexico for ~6 hours producing upslope condition over the study area, while the extratropical cyclone traveled farther eastward (Fig. 5.1c).

Cloudiness over the study area was initiated with the flow around the extratropical cyclone as it advected moisture from the Gulf of Mexico into the eastern Colorado (Fig.

5.2a). An orographic cloud persisted, owing to the northeasterly upslope flow associated with the lee trough in northeastern New Mexico, while the extratropical cyclone moved eastward (Fig. 5.2b). The 0000 UTC sounding from Denver, launched prior to the onset of precipitation there, shows the upslope northeasterly winds from the surface to approximately 4.0 km MSL, and southwesterly flow aloft (Fig. 5.3a). The orographic cloud layer was essentially at neutral stability and extended to 6.1 km MSL into the southwesterly flow regime. The cloud top temperature was −26°C.

With the onset of precipitation at ~2340 UTC on 4 March at the Foothills Lab, the surface layer rapidly moistened (Fig. 5.4). An abrupt decrease in temperature from 7 to 2°C occurred between 2340 UTC on 4 March to 0000 UTC on 5 March at this location. Similarly, the surface layer cooled rapidly from 5.5 to 0.5°C at approximately 0100 UTC at the disdrometer site, where the onset of precipitation was at ~0000 UTC (Fig. 5.4). Evaporation of precipitation in the surface layer combined with the cold air damming, as suggested by the northerly and northeasterly flow at low levels (Figs. 5.4b and 5.5) as well as cold air advection indicated by the cross-isothermal flow at the 700-mb level (not shown) may have caused the temperature to decrease significantly. Afterward, the surface temperature changed only slightly between 0.5 and −0.5°C.

Figure 5.3b shows the rawinsondes launched at 0310 UTC from the S-Pol radar site. The lower atmosphere was essentially at neutral stability as in the earlier sounding, but a deeper moist layer developed above the upslope airmass. The saturated layer aloft is associated with the formation of upper level cloud over higher terrain after 0100 UTC that gradually spread in the north-south direction (Figs. 5.2b-d). Notice, however, that the upper-level cloud shield barely enveloped the disdrometer site as the precipitation

was clearing from the northeast of Denver by 0300 UTC (e.g., Fig. 5.2d). Associated with this drying, the radar echo top began to descend at about 0230 UTC, eventually lowering to 4.7 km MSL by 0400 UTC (section 5.3). The cloud top temperature associated with the upslope layer was approximately –18°C while it was < –26°C for the upper-level cloud shield (Fig. 5.3b). A wind shift from easterly to northerly in the upslope layer was also occurring at the time corresponding to the 0310 UTC sounding (Fig 5.5).

5.2 Precipitation: The 2-D Video disdrometer observations

Most of the precipitation fell between 0000 and 0500 UTC at the disdrometer site. Table 5.1 summarizes the hydrometeor types noted by the author. Early precipitation was light rain (Period A). A rain-to-snow transition (Period B) occurred with the abrupt temperature decrease at 0100 UTC (Fig. 5.4). As in the 20 February 2004 case, the phase transition accompanied significant decreases in μ and Λ (Fig. 5.6, Period A to B). The field notes indicate that ice pellets were mixed with raindrops at this time. The smaller terminal velocities of ice pellets, compared with raindrops, are clearly depicted in the disdrometer data (Fig. 5.7, Period B). Large aggregates also existed at this time resulting in an increase in D_0 to 4.6 mm (Fig. 5.6). The mixed-phase precipitation period ended by 0120 UTC.

Later (0120-0145 UTC; Period C), observed precipitation consisted mostly of ice pellets and some small aggregates. Beginning at 0145 UTC (Period D), 1-3 mm plate-like crystals (plates and dendrites) became notable, and the number of large aggregates

increased significantly (Period D; Fig. 5.7b). The largest aggregate observed during this period was 15.7 mm in diameter. The observed terminal velocities show a weak relation to aggregate size. A power-law relationship derived from the observations is similar to that deduced from unrimed aggregates observed by Locatelli and Hobbs (1974) (*cf.* Fig. 4.5). Similar to the previous case, broad PSDs' indicated by small negative values of μ, near-zero Λ, and large D_0 characterize the snow distributions in Periods B through D (Figs. 4.5 and 5.6).

At ~0220 UTC, another change in particle habit occurred (Period E). Small lump graupel and lightly rimed irregularly shaped ice particles were mostly observed, and number of aggregates significantly decreased. Consequently, the values of μ and Λ increased (Fig.5.6). The terminal velocity appears to have a slightly stronger size-dependency compared with the previous stage (Fig. 5.7, compare Period D and E). The median volume diameter decreased significantly between the period of heavy aggregation (Period D; generally $D_0 > 5$ mm) and the subsequent graupel/snow pellet period (Period E; $D_0 \leq 3$ mm). This change would correspond to an estimated bulk density increase of 0.05 g cm^{-3} (Fig. 3.1).

5.3 Radar observations

In this section, the evolution of the precipitation layer is discussed. A sequence of radar observations indicated that early in the rain period (Period A), an elevated moist layer was present (Fig. 5.8a) consistent with the 0000 UTC Denver sounding (Fig. 5.3a). The surface layer became saturated as the precipitation developed (Fig. 5.8b). The PID

algorithm designated irregular ice crystal in the upper half and dry snow in the lower half of the precipitation layer. With the onset of the northerly flow after ~0230 UTC, the flow regime became more favorable for producing heavier orographic precipitation over the windward slopes of the Palmer Ridge to the south of the study area. Figure 5.8c particularly shows the region of heavier precipitation advecting toward the south of the disdrometer site (18.8 km). Eventually, the precipitation layer became shallow, and the light precipitation was mostly designated as irregular ice crystals by the PID algorithm (Fig. 5.8d). Overall, Z_{DR} slightly increased with time especially in the lower portions of the precipitation layer (e.g., < 3 km AGL).

Changes in precipitation microphysics can be inferred from the time-height cross-sections of the Z_H and Z_{DR} (Fig. 5.9). The cross-section was produced in the same way as in the 20 February 2004 case (Fig. 4.10; section 4.3). An overall decrease in Z_{DR} and increase in Z_H toward ground in Period B though Period D indicates that aggregation was taking place in the lower half of the cloud layer (below 3-3.5 km MSL) which is consistent with the ground observations of aggregates. These aggregates were composed of mostly dendrites with ferns and stellar ice crystals. However, lightly rimed or unrimed dendrites, stellar ice crystals, and some plates were also present (Table 5.1). Such ice crystals nucleate in water-saturated conditions within the planar crystal temperature range (Magono and Lee 1966; Fukuta and Takahashi 1999). Thus, these conditions were likely present at heights above 3.7 km MSL, corresponding to the upper half of the precipitation layer, and a relatively warm lower layer (> -7 or -6°C; Fig. 5.5) likely promoted an efficient aggregational process (e.g., Rogers 1974; Hobbs 1975).

As in Fig. 5.8, after ~0230 UTC, Z_{DR} increased and Z_H decreased in the lower half of the cloud layer (see for example below 3 km MSL in Fig. 5.9) consistent with an increase in bulk density as inferred from the disdrometer observations and the general absence of large aggregates. The temperatures gradually decreased in this layer after the period dominated by aggregates (Fig. 5.5). Colder temperatures likely made the aggregational process less efficient. Considering the time that particles took to settle through the cloud, some embryos of the graupel particles and rimed irregular ice perhaps originated in a region of a relatively higher Z_{DR} measured aloft between 0130 and ~0230 UTC (Fig. 5.9). "Cold-type" ice crystals (Hobbs 1975) such as rosettes and bullets also may have been advected from the upper-level cloud shield (section 5.1), which formed to the west of the disdrometer site by this time.

5.4 Comparison of the measured and computed radar parameters

Figure 5.10 shows histories of measured and computed Z_H and Z_{DR}. The radar measurements were averaged over a 1-km radius circle as in the 20 February 2004 case. The Z_H and Z_{DR} fields were uniform in the horizontal (Fig. 5.8); thus, the computations do not take in account particle trajectories. The standard deviation of the measured Z_H was 2-3 dBZ and that of Z_{DR} were between 0.2 and 0.3 dB from 0000 to 0400 UTC and were 0.2 and 0.5 dB afterwards due to lower signal to noise ratios.

The Z_H estimations with the disdrometer data in Period A are slightly less than the radar measurements because the measurements are in part from an elevated cloud layer with the maximum reflectivity at ~3 km (Fig. 5.8a). Additionally, evaporation at low

levels may account for the offset between the estimated and measured values. When Z_H is computed assuming that all particles are frozen in the rain period (Period A), the computations are significantly less than the measurements, reflecting the dependency of Z_H on the hydrometeor dielectric constant.

Agreement between the measured and computed Z_H is excellent during the rain-snow transition and snow periods (after 0100 UTC). Well-matched estimations in Period B, when using the scattering amplitude for frozen particles are consistent with return signals from large, low density aggregates dominating over the smaller raindrops and ice pellets. This is clearly evidenced with the Z_H computed based on the partitioned dataset containing only ice particles (black dotted line), which overlaps the radar measurements and the estimates of Z_H using all observed particles. Long (2004) simulated polarimetric radar parameters for a selection of Colorado winter storms using the T-matrix and Muller-matrix techniques. From the T-matrix estimations of signal returns from a rain-snow mixture at a 10-cm wavelength (S-band), he concluded that raindrops would typically dominate the radar returns in mixed-phase precipitation because of the higher dielectric factor of raindrops. However, the results from the three mixed-phase periods of the 20 February event and the current case reveal that radar returns are perhaps more sensitive to the precipitation phase (liquid or ice) that is more dominant in terms of particle sizes and/or number concentration. Z_H gradually increases in Period C though Period D in response to a broadening of PSD (Fig. 5.6) from active aggregation in the lower atmosphere. An overall reduction in the particle size and an associated decrease in snowfall rate (Period D and Period E) coincide with a Z_H reduction of 10 dBZ or more as discussed previously.

Similarly, Z_{DR} calculations and measurements for the respective rain and snow phases show good agreement with the calculated values mostly within the measurement errors (Fig. 5.10). As with Z_H, Z_{DR} calculations based on raindrop scattering amplitudes greatly exceed the measurements during the rain-snow transition period because the scattering amplitudes of raindrops take into account their tendency to become more oblate with size. Correspondence for the snow period is attributable in large part to accounting for change in particle density. Small Z_{DR} is associated with low-density aggregates in Period B through Period D. The values of computed Z_{DR} slightly increased when the number of aggregates significantly decreased and small graupel particles and snow grains with higher density became dominant (Period E). A general decrease in Z_{DR} from 0.3 and 0.1 dB between the 1.5 and 0.5° elevation scans during Period E can be interpreted as evidence that particles were more pristine having a higher bulk density and more oblate at higher elevations, and that the riming process between the two scan levels caused the particles to become less oblate in the mean and less dense as they fell. Aggregational growth processes have the same effect on Z_{DR}, but few aggregates were observed and rimed ice particles dominated at the ground level in Period E (Table 5.1). The computed Z_{DR} is generally less than the measured Z_{DR} after 0400 UTC. A change in particle habit was not observed at this time, and inspection of the radar data indicated that the larger values of the measured Z_{DR} were due to a decrease in signal-to-noise ratios (< 30) associated with the weakening precipitation at this time.

In order to examine the assertion that riming processes reduced Z_{DR} between the 1.5 and 0.5° elevation scans during Period B, a simple computation was performed to determine the liquid mass that an ice crystal would accrete during its descent towards the

ground to become a rimed particle of observed sizes. The equivalent diameters were generally 1-3 mm during this period (Fig. 5.6). The expression for particle growth rate via the riming process for a single ice crystal is given by,

$$\left.\frac{dm}{dt}\right)_{RM} = E_{c,i}\,\overline{A}(t)\,w_L v_t \tag{5.1}$$

where $E_{c,i}$ is the collection efficiency between the ice particle and cloud droplets, w_L is the cloud liquid water content, and v_t is the terminal velocity of the ice particle (Pruppacher and Klett, 1997), with $\overline{A}(t) \cong (\pi/4)D_i^2$ for an oblate spheroidal ice particle of equivalent diameter D_i falling with its major axis in the horizontal. Equation 5.1 assumes that the size and fall velocity of cloud drops are negligible compared with those of the ice crystal. The growth rate with respect to the vertical displacement of the ice crystal is expressed as

$$\begin{aligned}\left.\frac{dm}{dh}\right)_{RM} &= \left.\frac{dm}{dt}\right)_{RM} \Big/ \frac{dh}{dt} \\ &= \alpha\frac{\pi}{4}D_i^2 E_{c,i} w_L\end{aligned}, \tag{5.2}$$

where dh/dt is the sum of the vertical velocity of air (w) and v_t, and $\alpha = 1/(1+w/v_t)$. The integration of Eq. 5.2 from heights h_0 to h_f ($h_0 > h_f$) yields the expression of the liquid equivalent mass (m) gained by the ice crystal,

$$\Delta m = m(h_f) - m(h_0) = \alpha\frac{\pi}{4}D_i^2 E_{c,i} w_L (h_0 - h_f) \tag{5.3}$$

assuming that the change in particle diameter is negligible. For simplicity, $E_{c,i}$ of 1, and w_L of 0.05-0.1 g m^{-3} were assumed. The cloud water content of 0.05-0.1 g m^{-3} is reasonable based on previous observations of upslope storms in the Front Range regions (e.g., Boatman and Reinking 1984; Pobanz et al. 1994; Rasmussen et al. 1995). The w was considered negligible; thus $\alpha = 1$. According to Eq. 5.3, a 1-3 mm ice particle would

accumulate 0.026-0.235 mg (w_L = 0.1 g m^{-3}) or 0.013-0.117 mg (w_L = 0.05 g m^{-3}) of rime between the heights of the 1.5 and 0.5 degrees antenna elevation scans at the disdrometer site. This corresponds to a decrease in bulk density by 0.050-0.017 (w_L = 0.1 g m^{-3}) or 0.025-0.008 g cm^{-3} (w_L = 0.05 g m^{-3}) between the two levels, while the accretion process also makes the particles less oblate. Therefore, the reduction in Z_{DR} between the two heights by the decrease in bulk density and increase in axis ratio (less oblate in the mean) is plausible. A greater change in mass is possible if the effect of the upslope flow over the topography, e.g., in order of 0.2 m s^{-1} (Cotton and Anthes, 1989) is taken into account. Note, however, that the reduction in Z_{DR} between the two levels is within the measurement error of the radar system.

Table 5.1: Summary of field notes taken at the disdrometer site on 5 March 2004. Particles types are listed from most to least dominant in terms of numbers. Typical aggregate sizes (mm), percentage of total particles identified as aggregates, and degree of riming (none, light, moderate, heavy) are noted.

Time (UTC)	Hydrometer	Aggregates	Temperature (°C)
(A) 0000-0100	Raindrops	—	5.5-7
(B) 0100-0120	Mixture of rain and ice pellets	Wet aggregates	0.5-5.5
(C) 0120-0145	Ice pellets	3-8mm 30 % light	0.5
(D) 0145-0220	Dendrites, plates, stellars	3-10 mm 40 % light to moderate	0.1
(E) 0220-0400	Irregular ice particles, lump graupel	2-5 mm 5-20 % light (irregular ice particles)	–0.5-0.1

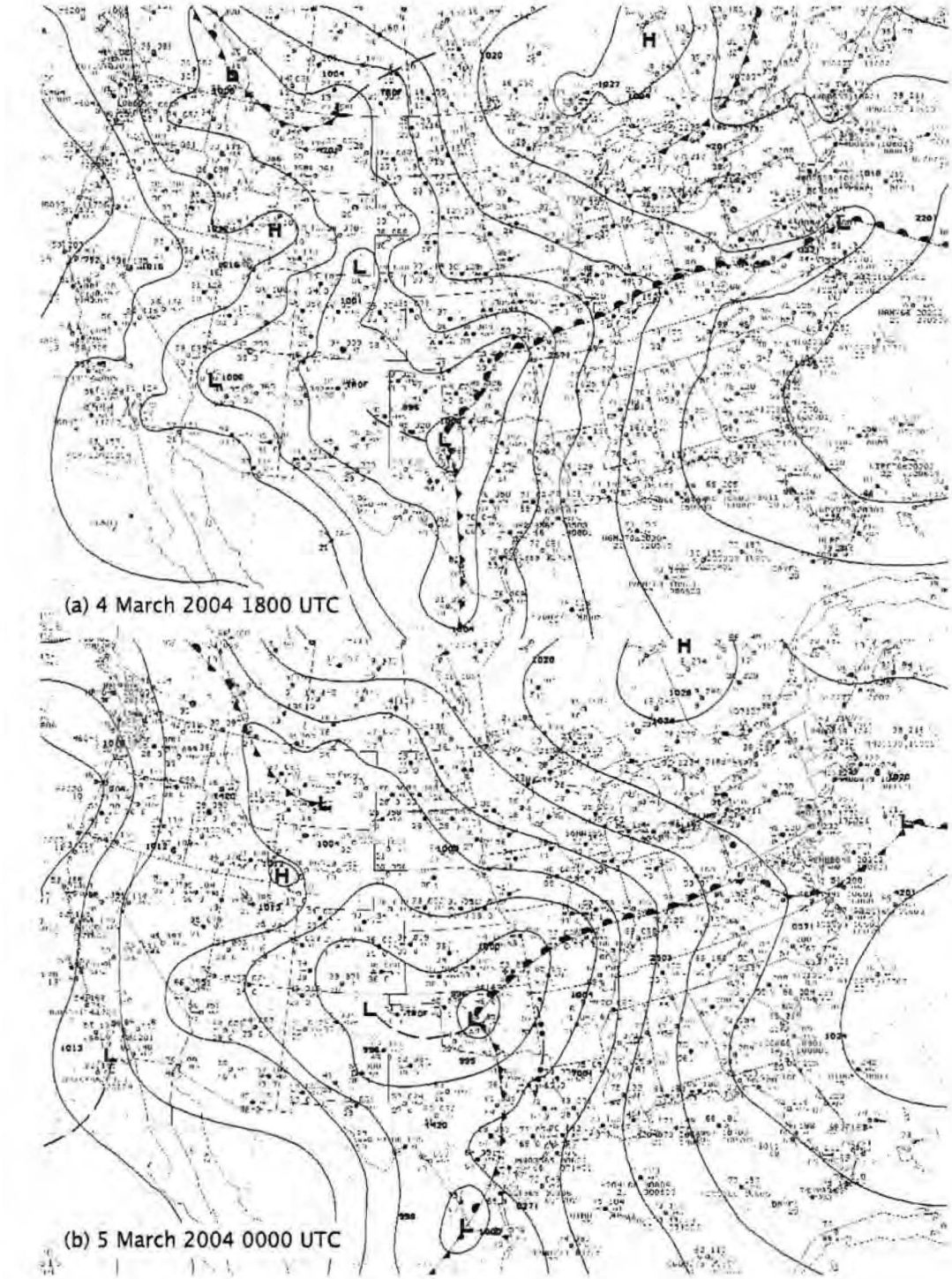

Figure 5.1: The NCEP surface analysis for (a) 1800 UTC on 4 March 2004, (b) 0000 UTC, and (c) 0300 UTC on 5 March 2005. Contour lines are mean sea level pressure in intervals of 4 mb.

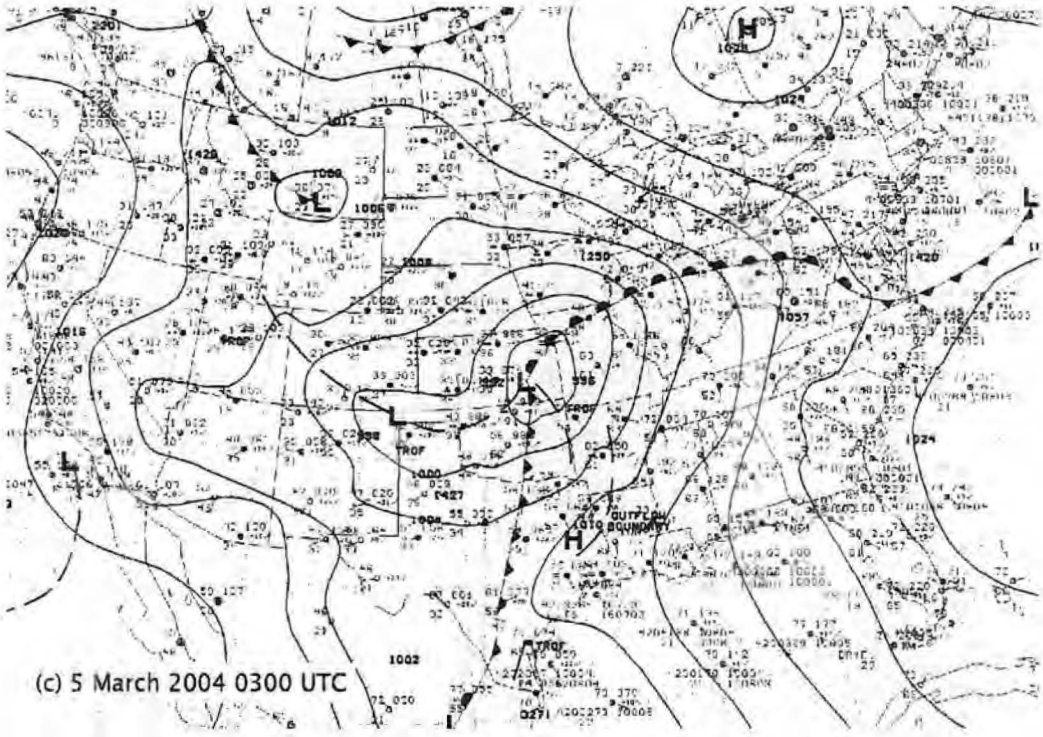

Figure 5.1: Continued.

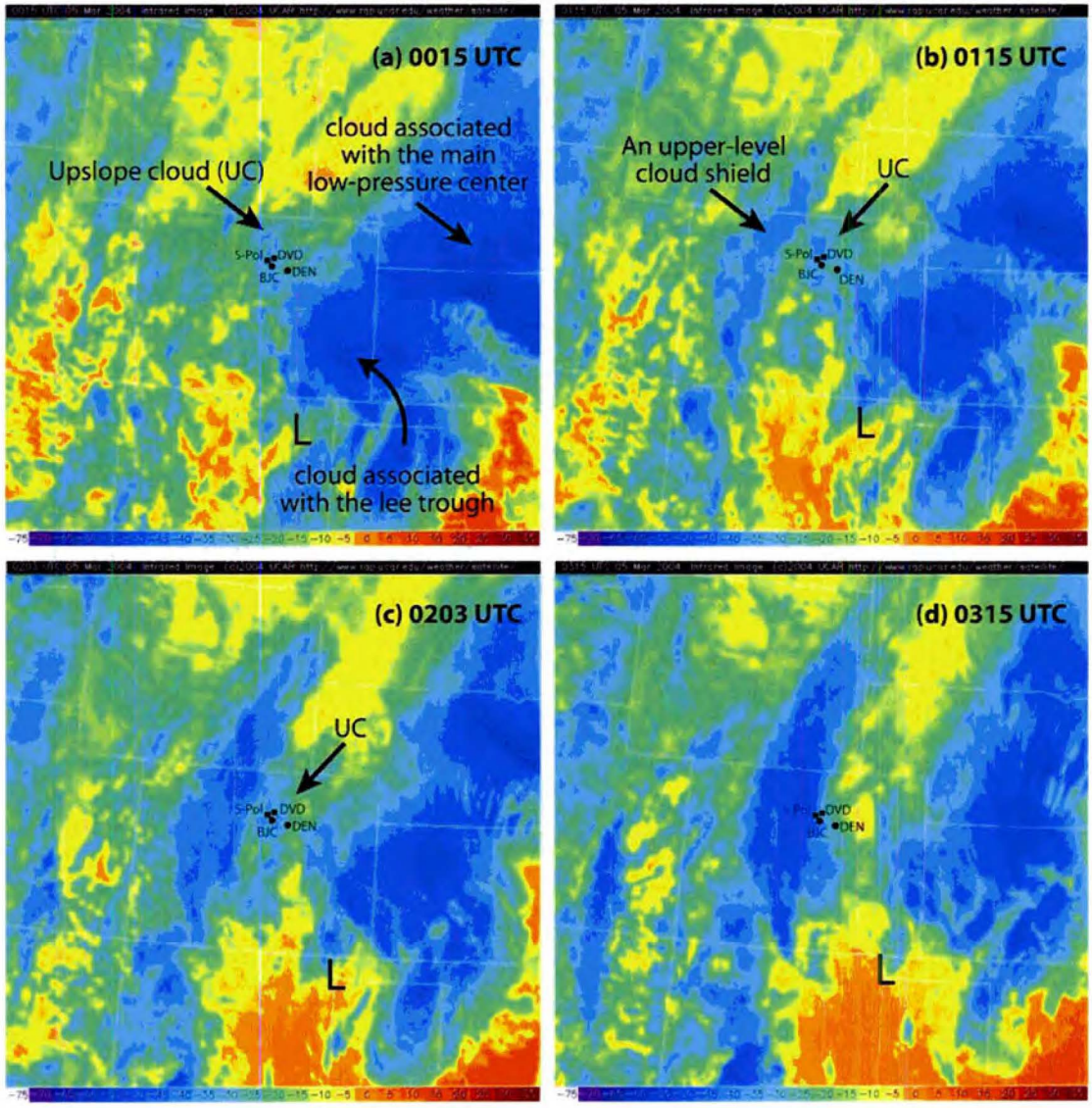

Figure 5.2: Infrared satellite images for (a) 0015, (b) 0115, (c) 0203, and (d) 0315 UTC on 5 March 2004. The color scale shows temperatures in degrees Celsius. The locations of the S-Pol radar, disdrometer (DVD), and the NWS surface stations in Boulder (BJC) and Denver (DEN) are shown. "L" corresponds to the low pressure center associated with the lee trough detemined from the surface analysis (Figs. 5.1b-c). Also indicated are various cloud features discussed in the text.

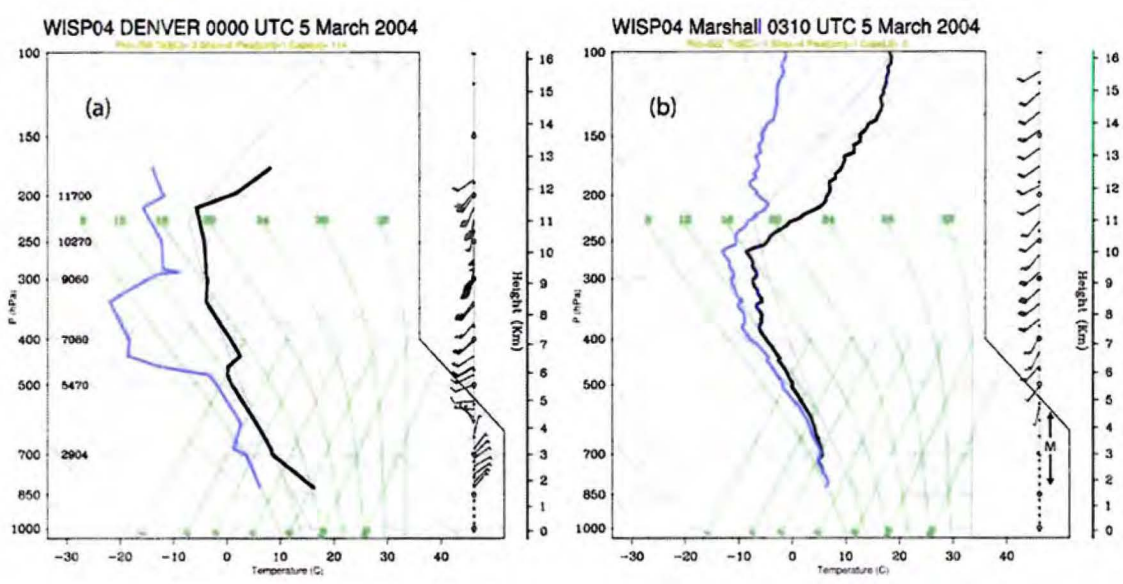

Figure 5.3: Skew-T soundings at (a) 0000 UTC from Denver, and (b) 0310 UTC from the Marshall field site. Full flags on wind barbs indicate 10 m s^{-1}. M indicates missing wind data.

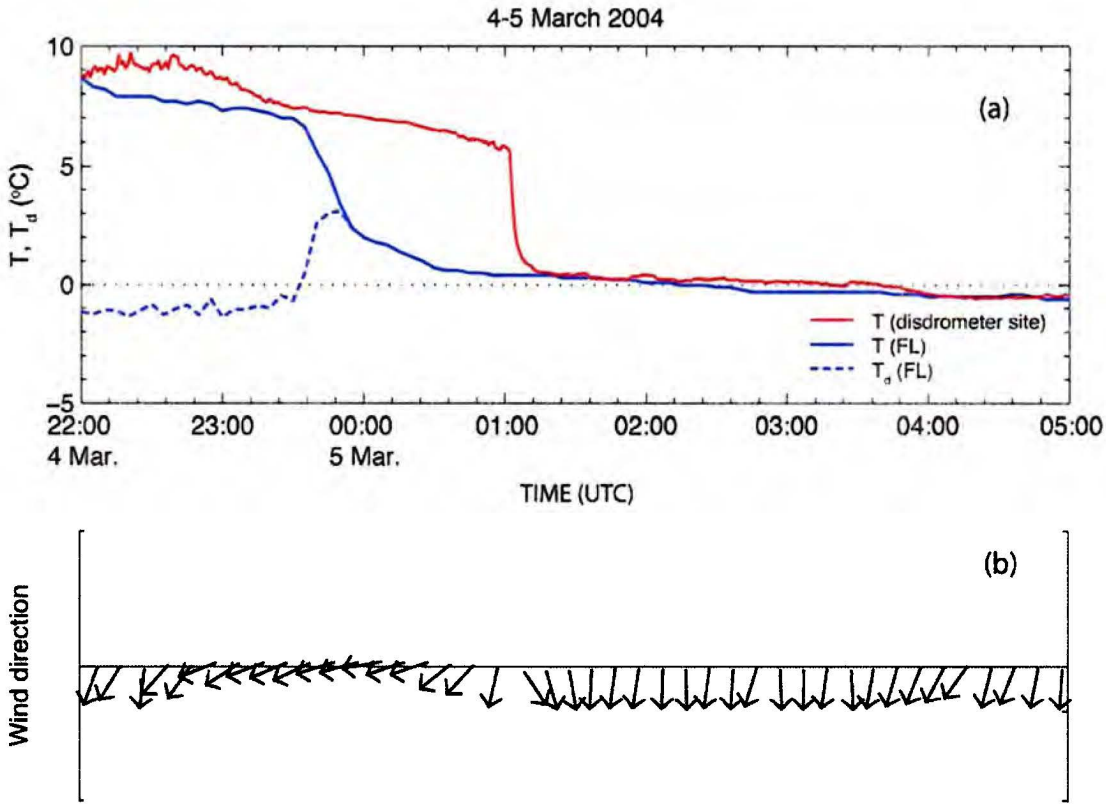

Figure 5.4: (a) Time histories of surface air temperature (T) at the disdrometer site and the FL and dewpoint temperature (T_d) at the FL for 4-5 March 2004. (b) Wind directions recorded at the disdrometer site.

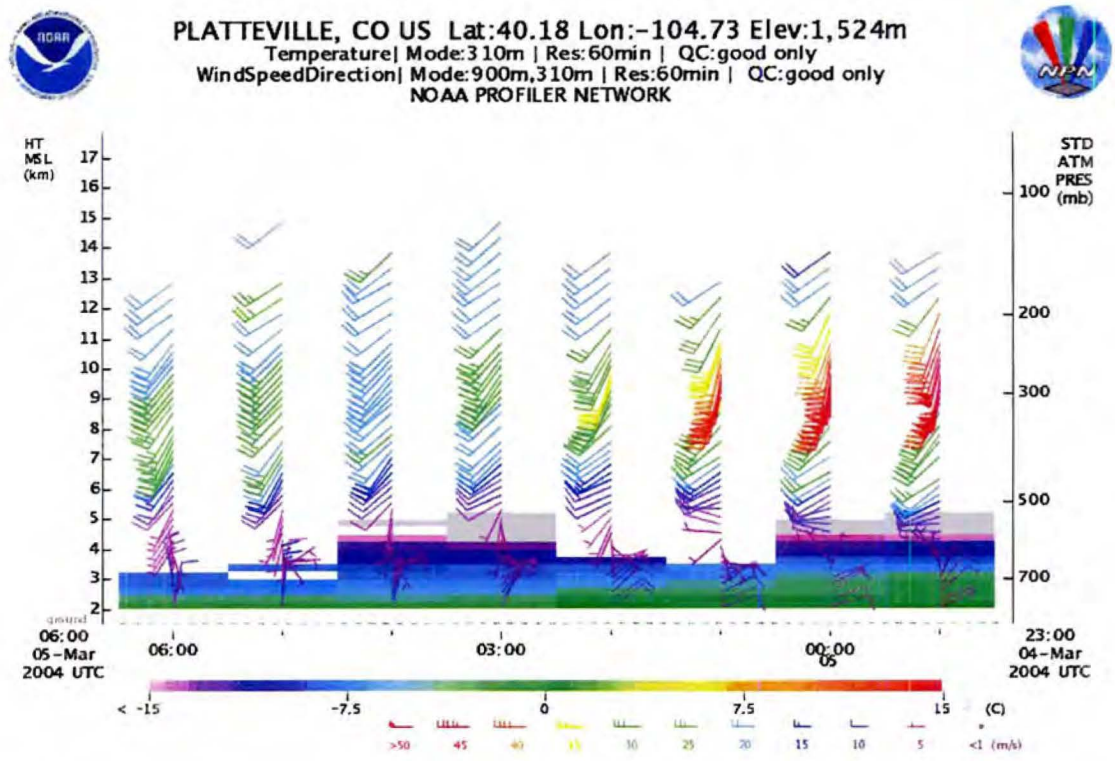

Figure 5.5: Time-height cross-section showing wind profiles and temperature at Platteville between 2300 UTC on 4 March 2004 and 0600 UTC on 5 March. Winds are color-coded in terms of wind speed (the wind barbs shown at the bottom of the figure). Temperature scales are indicated by the color bar. Temperatures lower then -15°C are in gray.

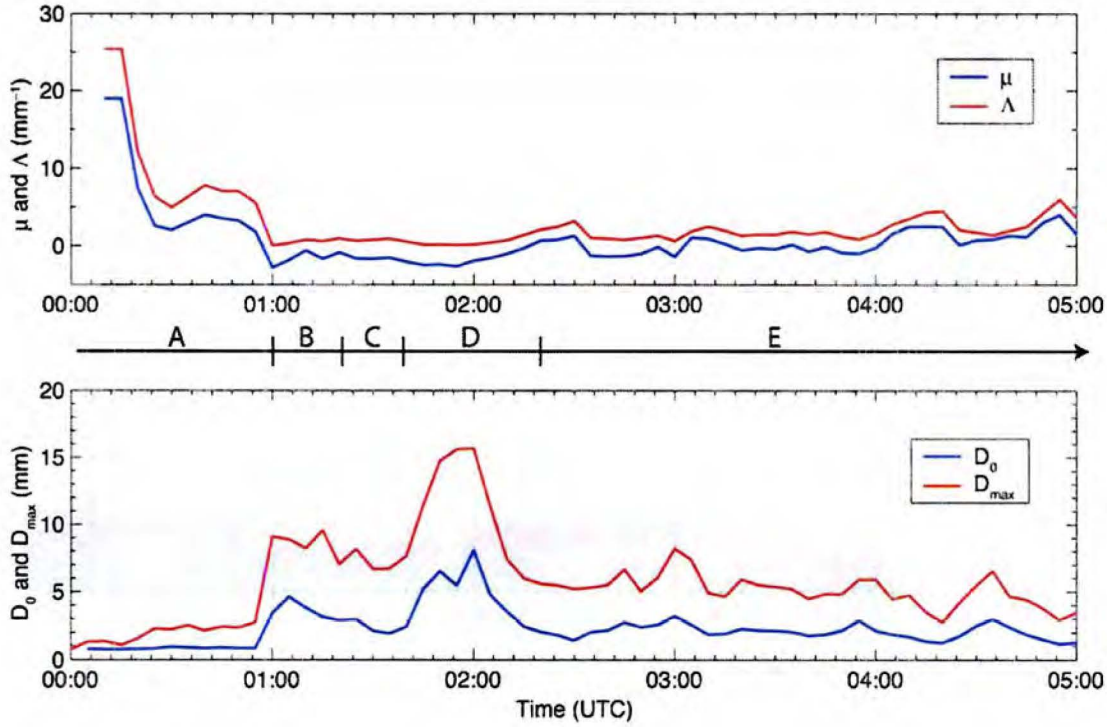

Figure 5.6: Same as Fig. 4.6, but for 5 March 2004. Periods A-E correspond with Table 5.1.

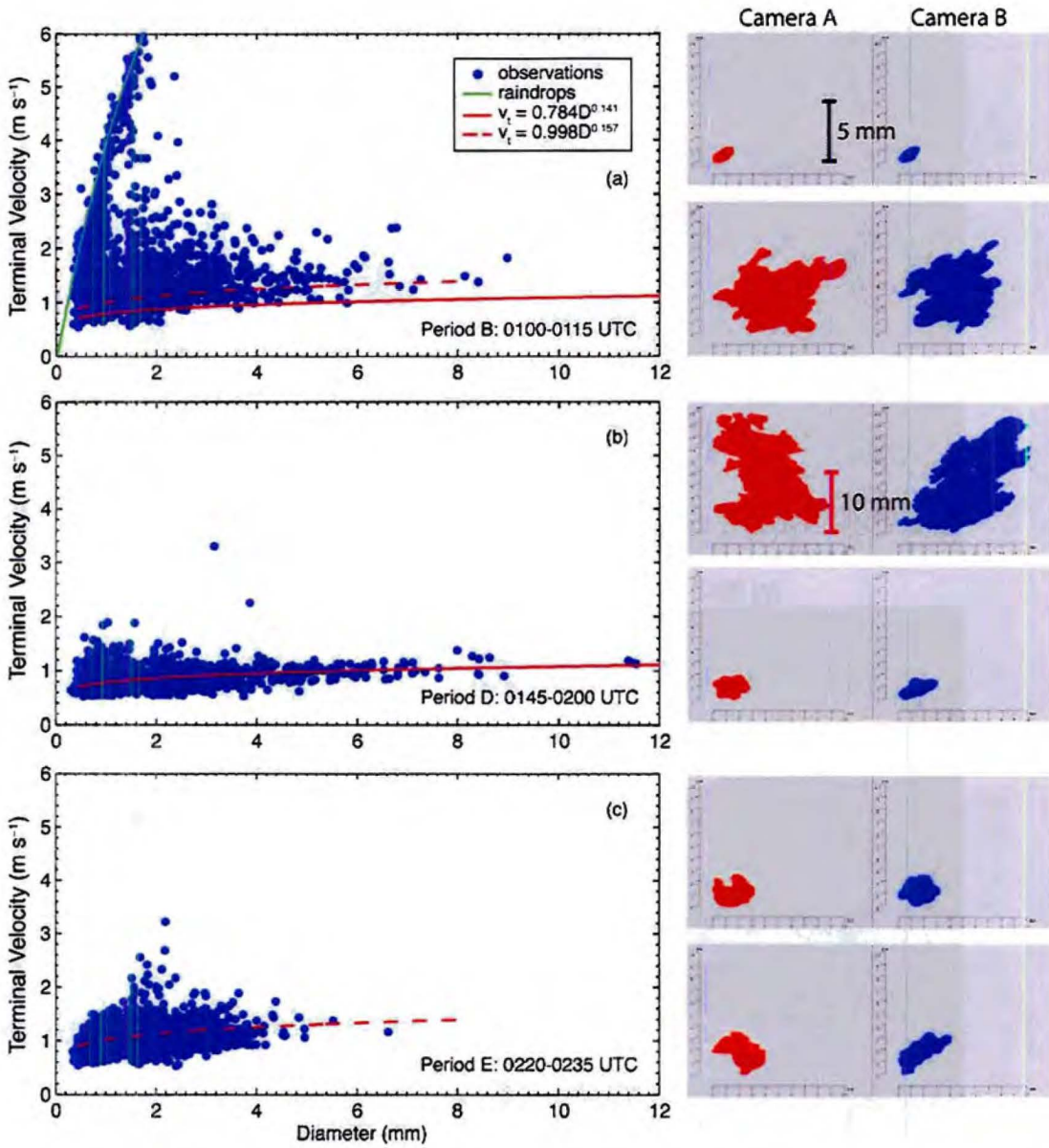

Figure 5.7: As in Fig. 4.5 but for select time segments in (a) Period B, (b) Period D, and (c) Period E on 5 March 2004. Power relations correspond with data points in b (solid) and c (dashed). The bold black line on the sample particle images indicates the 5 mm length scale for all images except for the third row from the top.

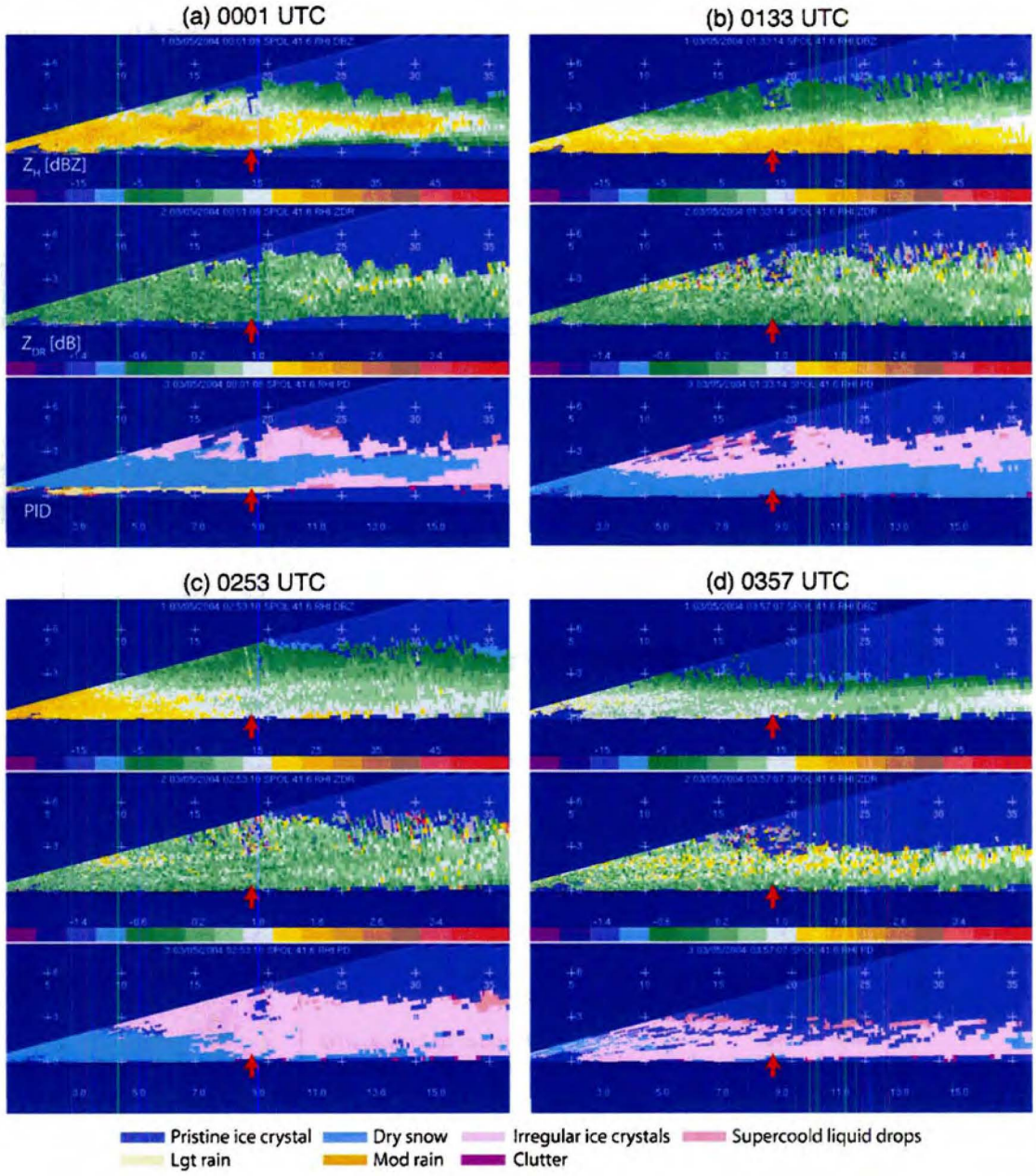

Figure 5.8: Same as Fig. 4.8 but for (a) 0001 UTC, (b) 0133, (c) 0253, and (d) 0357 UTC on 5 March 2004.

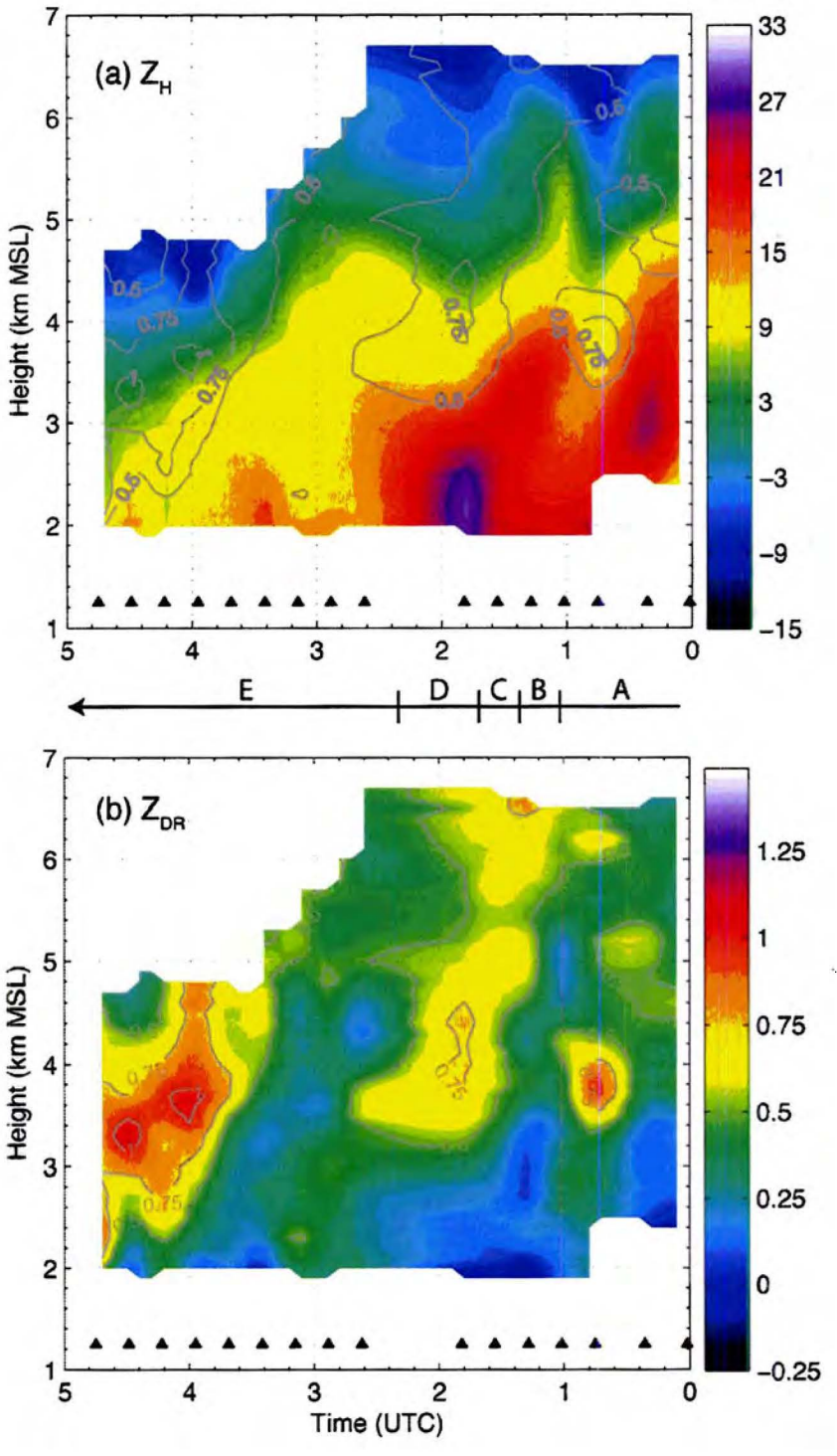

Figure 5.9: As in Fig. 4.10 but for 5 March 2004.

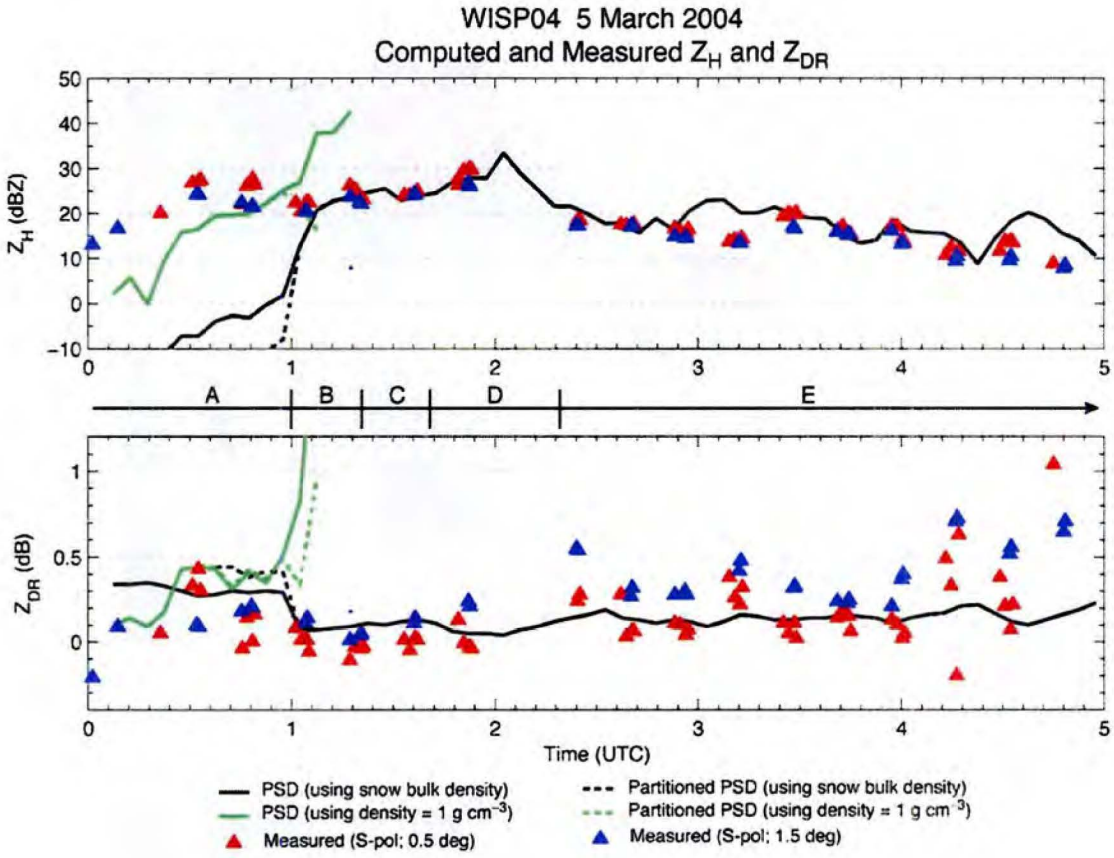

Figure 5.10: Same as Fig. 4.11 but for 5 March 2004.

Equation Chapter 6 Section 1

CHAPTER 6

SENSITIVITY OF THE SCATTERING CALCULATION TO ASSUMED ICE PARTICLE CHARACTERISTICS

The computational method used to this point in this study has considered a single ρ_s-D relation (Eq. 3.4) and assumed a constant axis ratio of 0.7. Undoubtedly, the values of Z_H and Z_{DR} are dependent on various assumptions of ice particle characteristics. Thus, it is important to examine the effect of these assumptions on the scattering calculations. In this section, the sensitivity of scattering calculations to bulk ice particle density and particle shapes is demonstrated using the data from 5 March 2004. Z_{DR} is also sensitive to fall mode of ice particles, but this factor is not considered here and is left as a future topic of research.

The computations are based on Rayleigh-Gans approximation. In this method, backscattering amplitude at horizontal (S_{HH}) and vertical (S_{VV}) polarization is defined as

$$\begin{aligned} S_{HH}(r,D) &= \frac{k_0^2}{4\pi}\frac{V(\varepsilon_r-1)}{1+1/2(1-\lambda_\varsigma)(\varepsilon_r-1)} \quad [mm] \\ S_{VV}(r,D) &= \frac{k_0^2}{4\pi}\frac{V(\varepsilon_r-1)}{1+\lambda_\varsigma(\varepsilon_r-1)} \quad [mm] \end{aligned}, \tag{6.1}$$

where k_0 is the free space propagation coefficient, ε_r the real component of dielectric factor, V the particle volume, D the equivalent diameter, r the axis ratio, and λ_ς the

depolarizing factor [see e.g., Bringi and Chandrasekar (2001)]. The depolarizing factor is a function of particle shape alone. For an oblate particle it is given by,

$$\lambda_\zeta = \frac{1+f^2}{f^2}\left(1-\frac{1}{f}\tan^{-1}(f)\right) \tag{6.2}$$

where

$$f^2 = \frac{1}{r^2} - 1. \tag{6.3}$$

Since the dielectric factor of frozen particles is relatively small, most ice particles are Rayleigh scatterers at S-band unless they are relatively large and wet. Therefore, the backscatter amplitudes and differential scattering amplitudes for a single particle derived using the T-matrix and Rayleigh-Gans methods differ only slightly when particles are larger than 20 mm (not shown), and thus the estimates of radar parameters from the two approaches are essentially the same.

6.1 Bulk ice particle density

Numerous ρ_s-D relations are found in the literature. Table 6.1 lists a selection of these works for snow aggregates and graupel-type particles (including irregular ice particles)—the two dominant particle types that were observed during Periods C-E on 5 March 2004—and the more generally-classified ice particles (i.e., containing various types of crystal habits and their aggregates). Differences among the relationships arise from the various techniques used to determine ρ_s, instrument sensitivities, definition of characteristic dimension, and atmospheric conditions. Nevertheless, Eq. 3.4 generally matches the size-dependent relations, especially like those of Holroyd (1971) and Fabry

and Syzrmer (1999) (Figs. 6.1-6.2). The expression from Magono and Nakamura (1965) is an anomaly possibly because their dataset included wet snow aggregates. Additionally, the densities of graupel particles from the past studies are generally higher than Eq. 3.4 for a given size, ranging between 0.1 and 0.7 g cm^{-3}.

In order to test the sensitivity of the scattering calculations (Eq. 6.1) to assumed ρ_s, a select set of relations in Table 6.1 was used to compute the backscattering cross-section at horizontal polarization (σ_H) and differential reflectivity (σ_{DR}) for a single particle. They are defined in Vivekanandan et al. (2004) as

$$\sigma_H = \frac{4\pi}{k^2}|S_{HH}|^2 \quad [mm^4], \tag{6.4}$$

where k^2 is the wavenumber, and

$$\sigma_{DR} = 10\log_{10}\frac{|S_{HH}|^2}{|S_{VV}|^2} \quad [dB], \tag{6.5}$$

respectively. The axis ratio is 0.7 as assumed in Chapters 4-5. In addition, constant ρ_s of 0.1 and 0.7 g cm^{-3} was attempted for graupel-like particles.

The effect of density on σ_{DR} is clear. As expected, the more dense an ice particle is the larger the σ_{DR} for a given particle size in response to the assumed oblate particle shape (Figs. 6.3a and 6.4a). The differences among the various relations are 0.2 dB or less for particle sizes larger than 1 mm, with an exception of σ_{DR} computed using the relation given by Magono and Nakamura (1965). On the other hand, σ_{DR} does not vary with size when ρ_s is fixed (Fig. 6.4a). Furthermore, the differences in σ_H increases with size (Figs. 6.3b and 6.4b) due to the D^6-dependency (Vivekanandan et al. 1993), which arises from Rayleigh scattering.

Figures 6.3c-d and 6.4c-d show the net effect of the ρ_s-D relations on the observed PSDs for the storm stages during which an abundance of aggregates were present (aggregate-period; Periods C-D) and the subsequent period in which graupel-like particles became dominant (graupel-period; Period E). The calculations assumed ρ_s = 0.92 g cm^{-3} when the estimated ρ_s exceeded the density of solid ice. With the exception of Magono and Nakamura (1965), the disdrometer-based Z_{DR} and Z_H are within 0.2-0.4 dB and 2-10 dBZ of radar measurements, respectively, when using a size-dependent ρ_s-D relation. In contrast, assuming a constant density of 0.7 g cm^{-3}, the computed Z_{DR} and Z_H exceed radar measurements on average by 1.0 dB and 20 dBZ (Fig. 6.4d). These overestimates are an effect of accumulating the density bias over size spectra due to not taking into account the decrease in density with size, and the overestimates are exacerbated when calculating Z_H due to the D^6-effect. Thus, there is a considerable advantage to using a representative size-dependent ρ_s when computing radar parameters.

The current sensitivity test shows that the ρ_s-D relation developed with disdrometer data collected at the Marshall field site (Eq. 3.4) produced the best overall agreement with the Z_H measurements. Since particle shapes have no effect on Z_H, and Z_H depends primarily on ρ_s, this correspondence reveals that Eq. 3.4 well represents the ρ_s of this snow event. This in turn suggests that the discrepancies between the measured and estimated Z_{DR} are from the assumed particle shapes and/or distribution of canting angle (i.e., fall mode).

6.2 Particle shapes

Two approaches were taken to examine the sensitivity of scattering calculations to axis ratios. The first approach assumed axis ratios of aggregates, graupel, and irregular ice particles found in the literature. In the second method, empirical relations between aspect ratio and particle size from the disdrometer observations for Periods C-E on 5 March 2004 were used. Natural snowflakes have complex shapes; however, it is generally thought that details of the particle shapes are not important for scattering calculations because the dielectric factor of ice particles is small (e.g., Vivekanandan et al. 1994; Hogan et al. 2000). Here, Eq. 3.4 is used to estimate bulk ice particle density. Z_H is not shown here because it is not sensitive to particle shapes.

Previous observations have indicated that aggregates are nearly spherical (Magono and Nakamura 1965), and radar parameters have often been modeled with axis ratios between 0.8 and 1.0 (Vivekanandan et al. 1993; Hogan et al. 2000; and Liao et al. 2005). Heymsfield (1978) determined the axis ratios of graupel particles to be 0.4-0.9 based on aircraft observations. A similar range of axis ratios is expected for irregular ice particles and heavily rimed ice particles. Similar to the bulk density of ice particles, a wide range of values is possible depending on the methodologies and definitions to express axis ratio. In this study, axis ratios, defined as the ratio between the minor and major axis, of 0.4, 0.8, and 0.9 were attempted.

The effect of particle axis ratios is to reduce Z_{DR} to near zero values as the ice particles become less oblate (i.e., the axis ratio approaches unity) (Hall et a. 1984; Herzegh and Jameson 1992). This is evident in Fig. 6.5a in which σ_{DR} based on constant

values of axis ratio is shown. With an increase in particle size, the parameter becomes less sensitive to particle shape due to a smaller dielectric factor or, similarly, a reduced bulk density (Herzegh and Jameson 1992). Consequently, the differences in the disdrometer-based Z_{DR} for the ensemble of particles among the various assumptions are less during the aggregate-period, when a characteristic particle size (D_0) was relatively larger, compared to the graupel-period (Fig. 6.5b). It is interesting to notice in Fig. 6.5b that the computed Z_{DR} is in overall agreement with the measurements from the higher elevation scans when assuming an axis ratio of 0.4, while the correspondence is better with the data from the lower-elevation scans when the particles are considered less oblate. This is consistent with the earlier assertion that the initially oblate particles became less oblate as they descended towards the ground during this period due to riming (section 5.4).

Data from the 2-D Video disdrometer includes individual images of naturally falling ice particles. Using these images, relations between particle size and aspect ratio were determined for the aggregate- and graupel-period (Fig. 6.6). The data points are mean values of aspect ratios as seen from the two cameras in the disdrometer. In this study, aspect ratio is defined as the ratio between the maximum dimension in the vertical and horizontal directions (Fig. 6.7). The thought is that the aspect ratio expressed in this way corresponds with the instantaneous incident electromagnetic waves at vertical and horizontal polarization. As a snowflake passes through the two virtual measurement planes (Fig. 2.3), it drifts horizontally due to ambient winds and/or changes its orientation. The current results are possibly affected by these factors to some degree.

In Fig. 6.6, least-square fits through the mode of aspect ratios, with a 0.5-mm interval size categories between 0.25 and 20.5 mm, for the two storm stages are essentially the same. Additionally, the aspect ratios are nearly constant with average modal values of 0.80 (Fig. 6.6a) and 0.84 (Fig. 6.6b). A significant scatter for particle sizes < 2 mm is partly due to canted ice crystals and an artifact of the disdrometer data analysis algorithm that can be produced when particles seen by the two cameras are mismatched. The scatter is typically less for larger snowflakes.

When taking into account the changes in both density and aspect ratio with particle size, the calculations of the scattering amplitudes yield σ_{DR} shown in Fig. 6.8. A small increase in σ_{DR} for D > 1 mm is in response to a decrease in aspect ratio according to the expressions shown in Fig. 6.6. However, the changes are insignificant over the entire size range. Consequently, the calculated Z_{DR} was not sensitive to the size-axis ratio relation and was similar to that from an assumption of r = 0.8 (the green line in Fig. 6.5b). Future studies will examine aspect ratios and axis ratios of ice particles collected in a wind-protected environment and their relevance for studies of scattering behaviors of frozen particles for remote sensing applications.

Table 6.1: Empirical relations between density and particle size (D) and ranges of observed ice particle bulk densities (ρ_s) found in the literature. D is in mm, and ρ_s is in g cm^{-3}. Ice particle types and the ranges of particle size for the individual relations are also indicated.

Relationship	Reference	Description
$\rho_s = 0.0707D^{-1.1}$	Locatelli and Hobbs (1974) – 1	Aggregates of unrimed radiating assemblages of dendrites D = 2.0 – 12.0
$\rho_s = 0.170D^{-1.0}$	Holroyd (1971)	Unrimed snowflakes D = 0.1 – 25.0
$\rho_s = 0.175D^{-0.66}$	Hogan et al. (2000)	Irregular crystals and aggregates D = 0.3 – 5.0
$\rho_s = 2.0D^{-2.0}$	Magono and Nakamura (1965)	Wet and dry snowflakes D = 0.1 – 25.0
$\rho_s = 0.150D^{-1.0}$	Fabry and Syzrmer (1999) – 1	Snowflakes D = 0.2 – 7.0
$\rho_s = 0.120D^{-1.0}$	Fabry and Syzrmer (1999) – 2	Snowflakes D = 0.2 – 7.0
$\rho_s = 0.113D^{-0.9}$	Locatelli and Hobbs (1974) – 2	Graupel-like snow D = 0.5 – 2.2
$\rho_s = 0.07D^{-1.1}$	Brown and Francis (1995)	Irregular ice crystals D = ~0.1 – 5.0
$\rho_s = 0.05$ to 1.0	Locatelli and Hobbs (1974)	Lump graupel D = 0.5 – 2.0
$\rho_s > 0.10$ to 0.20	Locatelli and Hobbs (1974)	Lump graupel D = 0.5 – 3.0
$\rho_s > 0.20$ to 0.45	Locatelli and Hobbs (1974)	Lump graupel D = 0.5 – 1.0
$\rho_s = 0.45$-0.70	Zikmunda and Vali (1972)	Graupel D = 1.0 – 0.5
$\rho_s = 0.25$-0.45	Zikmunda and Vali (1972)	Lump graupel D = 1.0 – 2.0
$\rho_s = 0.20$-0.40	Heymsfield (1978)	Lump graupel D = 1.0 – 4.0
$\rho_s = 0.35$–0.70	Heymsfield (1978)	Conical graupel D = 1.0 – 4.0
$\rho_s = 0.178D^{-0.922}$	Brandes et al. (2006); Eq. 3.4 in this study	Unrimed and rimed snowflakes D = 0.6 – 9.0

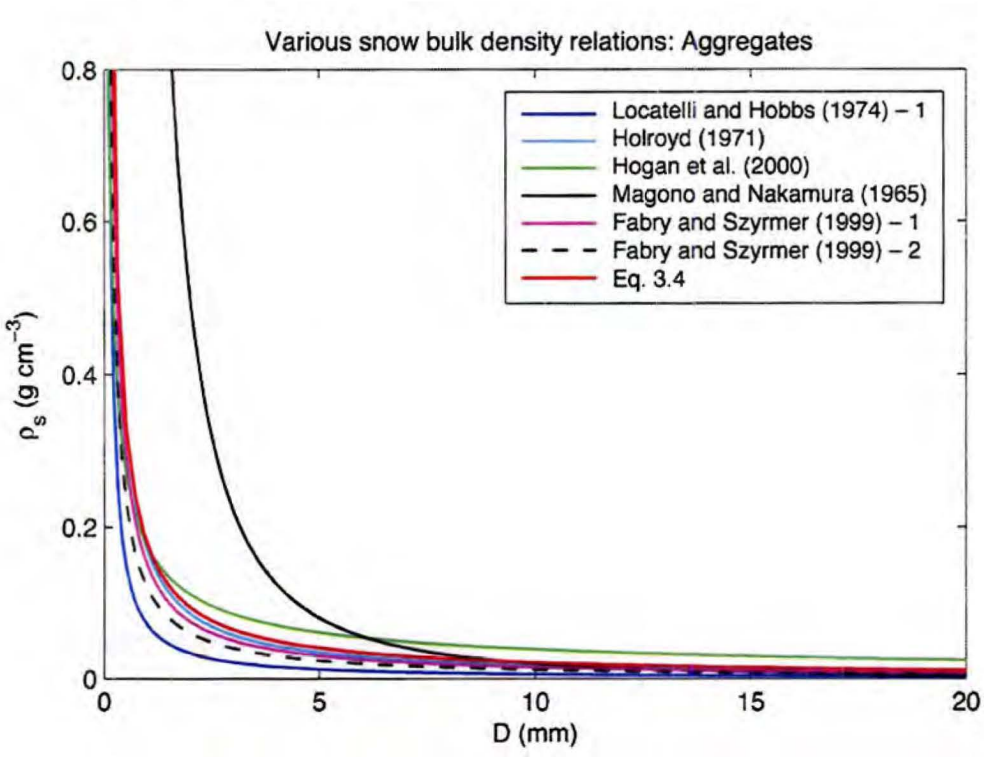

Figure 6.1: Density-size relations for various ice particles and aggregates found in the literature. See Table 6.1 for descriptions.

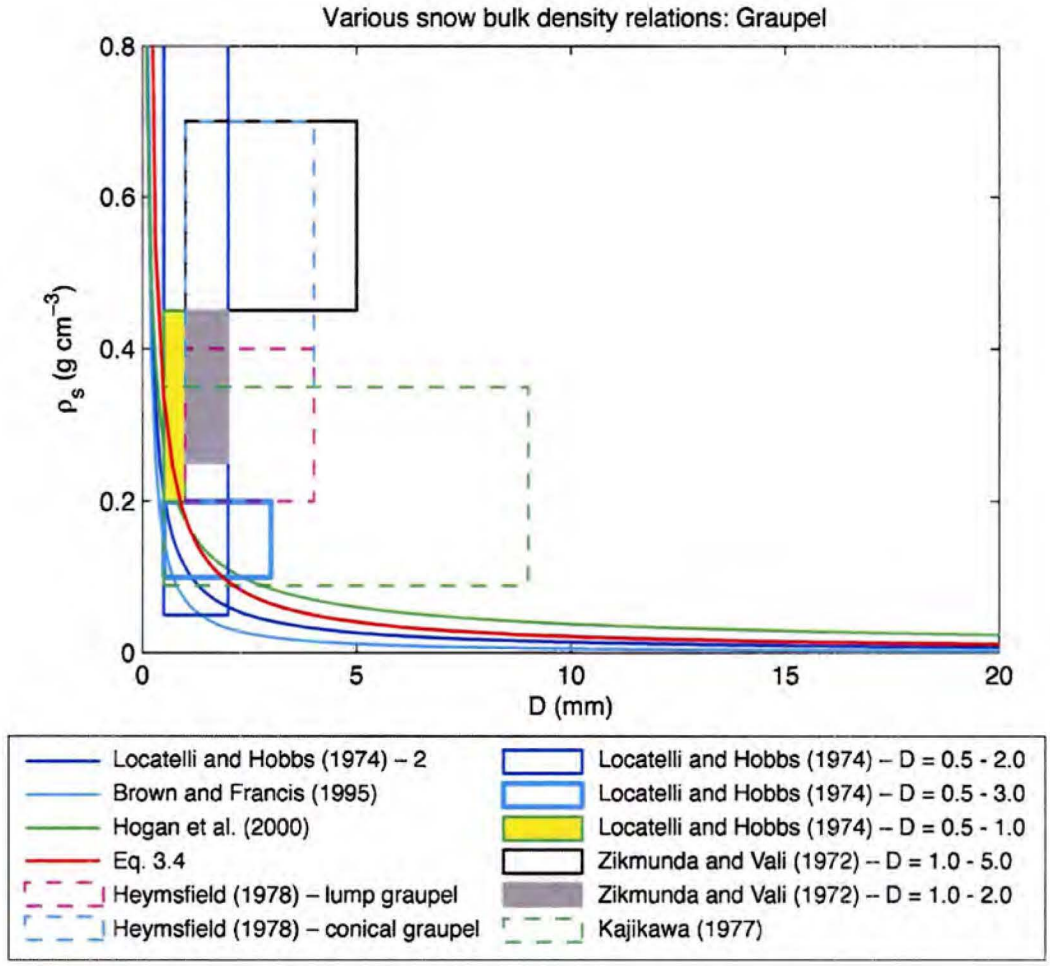

Figure 6.2: Same as Fig. 6.1 but for graupel-type particles (conical graupel, lump graupel, graupel-like snow, and rimed ice crystals). The ranges of bulk densities of observed graupel-type particles are enclosed with boxes.

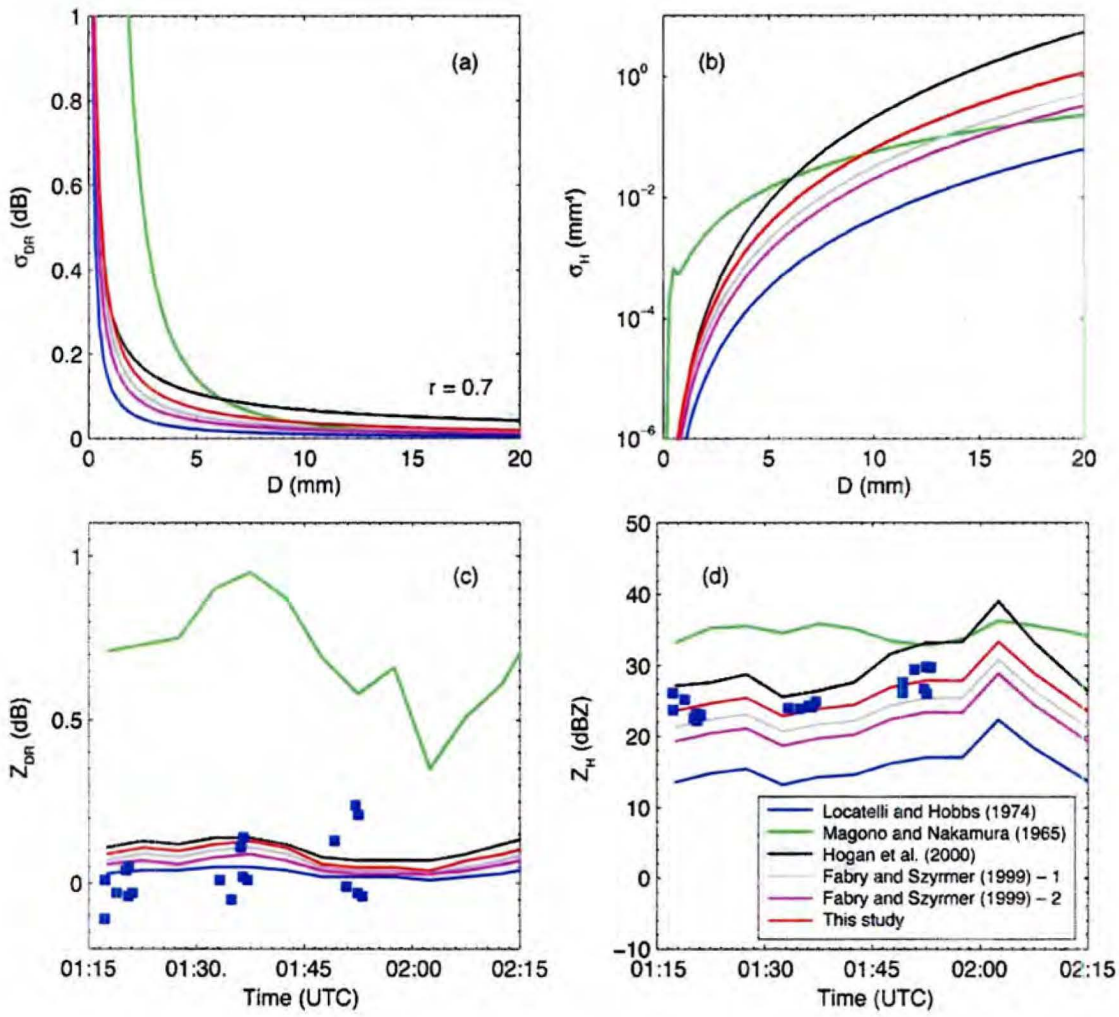

Figure 6.3: (a) Differential reflectivity (σ_{DR}) and (b) backscatter cross section (σ_H) for a single scatterer as a function of equivalent volume diameter using a select set of ρ_s-D relations from Fig. 6.1. (c) and (d) are time series of Z_{DR} and Z_H, respectively, for Periods C-D during the 5 March 2004 event. Blue squares are radar measurements. Axis ratio (r) of 0.7 is assumed. σ_H is undefined at D~0.6 mm when assuming the ρ_s-D relation from Magono and Nakamura (1965) (Table 6.1).

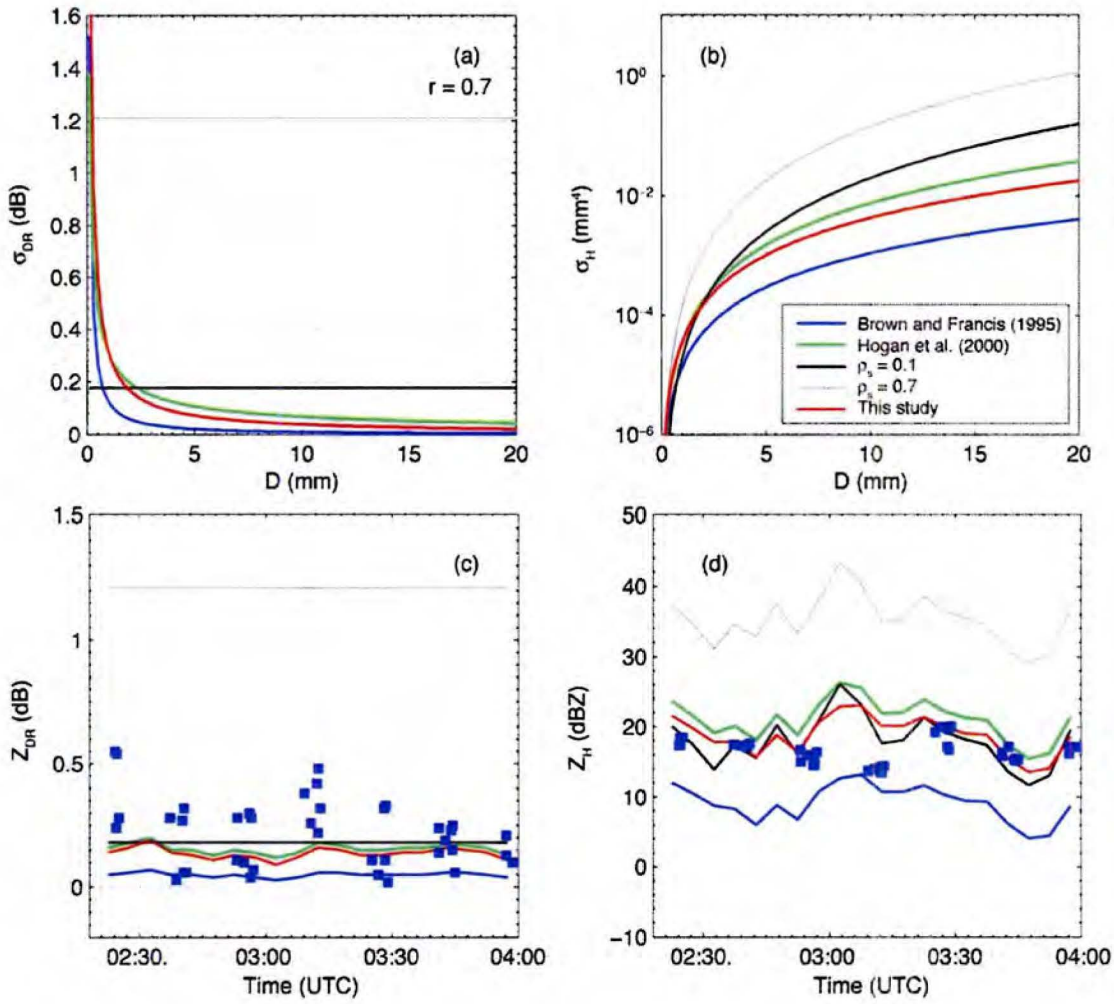

Figure 6.4: Same as Fig. 6.3 but using the ρ_s-D relations in Fig. 6.2. Z_{DR} and Z_H are estimated for Period E.

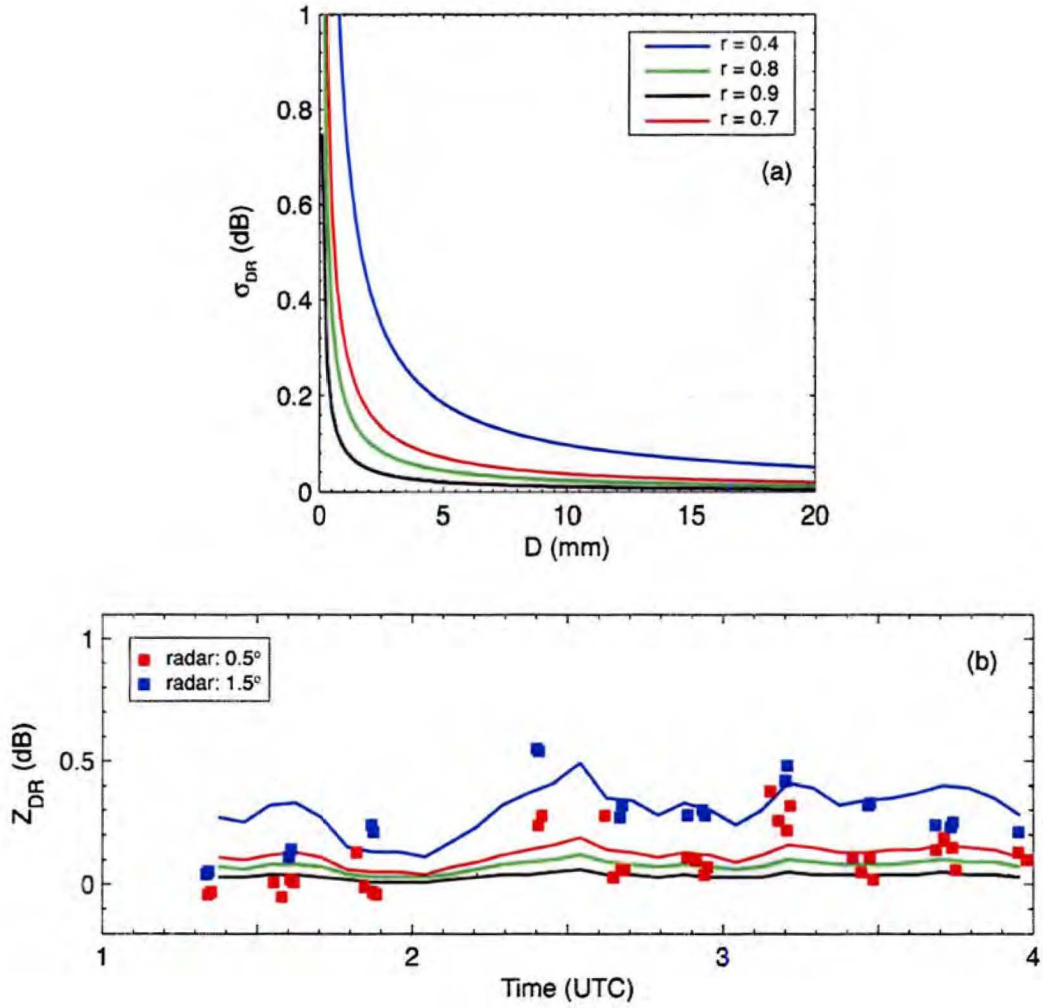

Figure 6.5: (a) σ_{DR} for aspect ratios of 0.4, 0.7, 0.8, and 0.9 as a function of equivalent volume diameter. r = 0.7 is an assumption used in Chapters 4-5. (b) Time series of computed Z_{DR} assuming aspect ratios in (a) for 0100-0400 UTC on 5 March 2004. Squares are radar measurements as in Fig. 5.10.

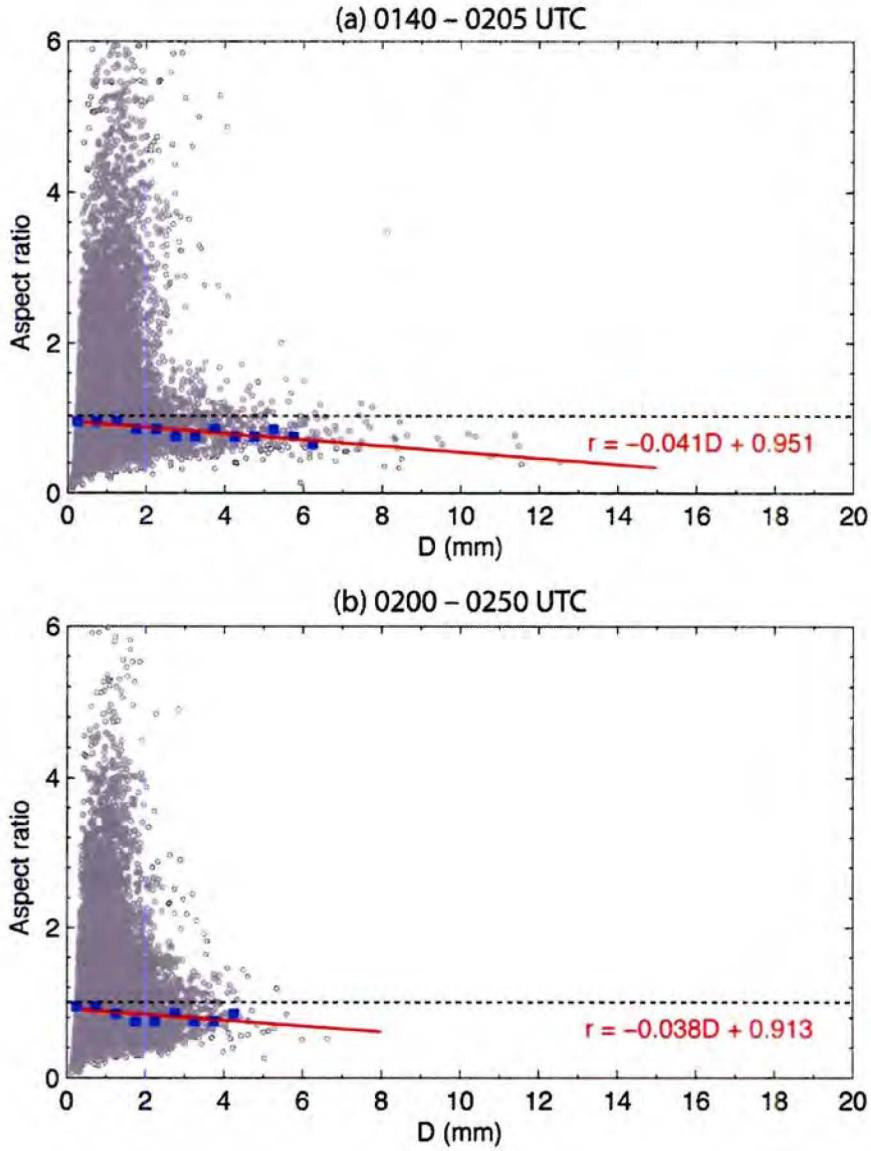

Figure 6.6: Aspect ratios versus equivalent volume diameter for time segments shown on 5 March 2004. 14740 and 19417 data points are in (a) and (b), respectively. Overlaid are modes of aspect ratios for particle size categories at an increment of 0.5 mm (blue square), and a least-square fit through the modes (red line). The size categories with fewer than 10 data points were not used to obtain the least-square fit. Dashed lines are aspect ratio of 1.

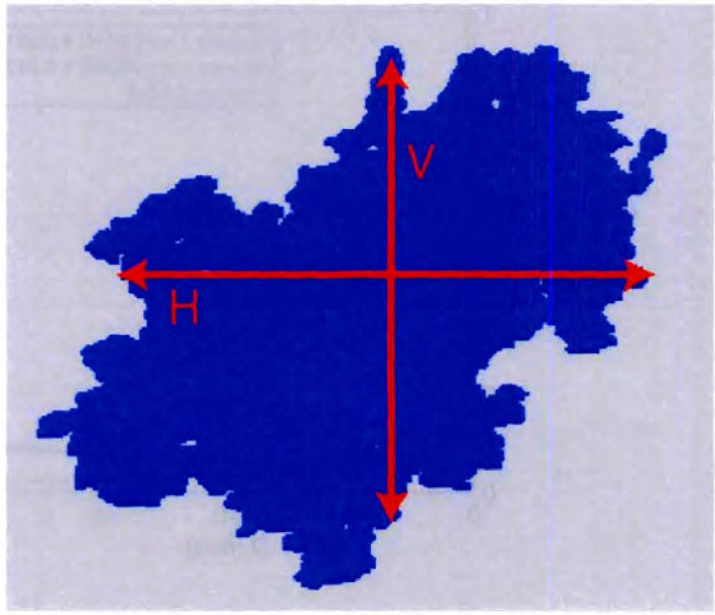

Figure 6.7: Illustration of the horizontally (H) and vertically (V) polarized electromagnetic waves intersecting a snowflake.

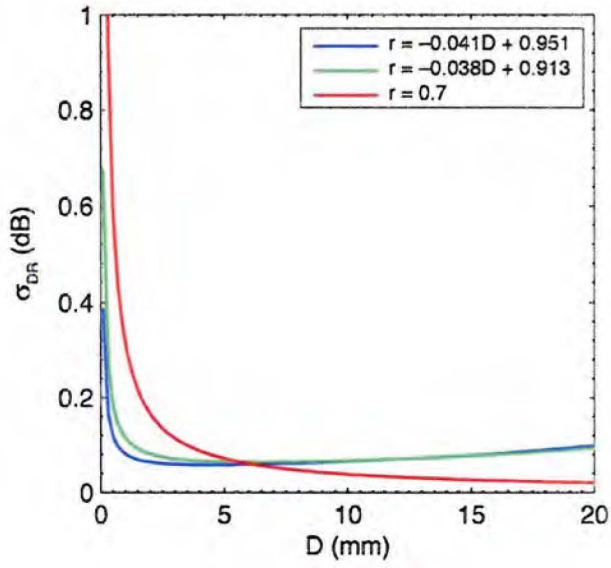

Figure 6.8: σ_{DR} as a function of equivalent volume diameter with an assumption that particle aspect ratios are related to particle size by the least-square fits in Fig. 6.6. The σ_{DR} computed with a constant axis ratio of 0.7 is overlaid. Eq. 3.4 is used for the scattering calculations.

Equation Chapter 7 Section 1

CHAPTER 7

RADAR-BASED RETRIEVALS OF PARTICLE SIZE DISTRIBUTIONS IN WINTER PRECIPITATION

Measurements of Z_H and Z_{DR} have previously been used to infer raindrop size distributions (e.g., Kozu and Nakamura 1991; Zhang et al. 2001; Brandes et al. 2004). Here, the retrieval procedure, referred to as the constrained-Gamma approach (Zhang et al. 2001; Vivekanandan et al. 2004), is applied to the data from Periods B-E on 5 March 2004. The retrievals are based on the definitions of Z_H and Z_{DR} expressed in terms of the Gamma PSD parameters [N_0, μ, and Λ (Eq. 4.1)], particle backscattering amplitudes based on Eq. 3.4, and an empirical relation between μ and Λ. From data collected from October through April between 2003 and 2005 at the Marshall site and at the disdrometer site during the WISP04 project, Brandes et al. (2006) determined that μ and Λ (mm^{-1}) are related by

$$\mu = -0.004992\Lambda^2 + 0.7982\Lambda - 0.6658 \tag{7.1}$$

using the 2nd, 4th, and 6th moments of the 5-minute PSDs. Figure 7.1 shows the correspondence between the Λ-μ relation and data points from the 5 March 2004 case.

The retrieval procedure first estimates Z_{DR} by iteratively finding Λ and the associated μ and PSD that match the measured Z_{DR}. Subsequently, N_0 is determined from the measured Z_H based on the definition of Z_H,

$$Z_{H,m} = \frac{4\lambda^4}{\pi^4 |K_w|^2} N_0 \int_0^{D_{max}} D^{\mu} \exp(-\Lambda D) |S_H|^2 \, dD, \tag{7.2}$$

where $Z_{H,m}$ is the reflectivity measurements, and the integral term is the N_0-normalized reflectivity calculated from the estimated Λ and $\mu(\Lambda)$. Once the three parameters are known, total particle concentration (N_t), D_0, and snowfall rates (S) can be computed from:

$$N_t = \int_0^{D_{max}} N(D) dD \quad [m^{-3}], \tag{7.3}$$

$$D_0 = \frac{\mu(\Lambda) + 3.67}{\Lambda} \quad [mm], \tag{7.4}$$

and

$$S = \int_0^{D_{max}} \frac{\pi}{6} D^3 \rho_s(D) N(D) v_t(D) dD \quad [mm\, h^{-1}]. \tag{7.5}$$

Whereas the measurements of Z_{DR} are used to estimate D_0 by relating drop shape and size when retrieving raindrop size distributions, the Z_{DR} measurements predict D_0 from the relation between ρ_s and particle size in snow. Thus, the retrievals depend on prescribed ρ_s-D and Λ-μ relations. The technique also depends on D_{max} because the integrals in Eqs. 7.3 and 7.5 are evaluated up to a reasonable maximum particle size rather than an infinite size.

Figure 7.2 compares the 3rd moment, N_T, D_0, and S deduced from the radar measurements and disdrometer observations. The 3rd moments, related to particle volume, match relatively well between the two datasets with a correlation coefficient of 0.58 in log space.

Total concentrations for Periods B and C are relatively consistent with the observations. However, the correlation is poor (0.24 in log space) between the

observations and retrievals particularly for N_T from the 0.5° elevation scans after 0220 UTC (Period E) when smaller and denser particles became dominant. On average, the retrievals exceeded the observations by one order of magnitude similar to the results obtained from a dual-wavelength-based retrieval by Liao et al. (2005). Consistently, the radar-based D_0 are generally smaller than the disdrometer observations with the root mean square error (RMSE) of 1.44 mm (Fig. 7.2c). Discrepancies arise partly from the fact that the bulk density rapidly changes toward smaller particle size (Fig. 3.4), the dynamic range of Z_{DR} for ice particles is small, and because the zero-order moment of the PSDs is retrieved from higher moments. *The results indicate that the current retrieval technique tends to infer denser particles for a given value of Z_{DR}.*

The correlation between the disdrometer-based S and the retrievals was 0.23 in the current case (Fig. 7.2d). Computations of S are sensitive to ρ_s, the 3rd moment of PSDs, and terminal velocity (Eq. 7.5). Considering the number of assumptions made about the complex characteristics of natural ice particles and the large discrepancies in the retrieved concentration and D_0 (Figs. 7.2b-c), or equivalently ρ_s, such a small correlation is not surprising. A similar correlation (0.2) with the disdrometer measurements was produced when computing S with an operationally utilized relationship between reflectivity and snowfall rate given by

$$Z = 200S^{1.6}, \tag{7.6}$$

where reflectivity (Z) is in $mm^6\ m^{-3}$ and S in $m\ h^{-1}$. Some improvements to estimating S should be possible as more is learned about the size distributions of natural ice particles in future studies and more radar-disdrometer comparison data become available in order to utilize polarimetric measurements.

Sensitivity of the retrieval procedure to ρ_s-D and Λ-μ relations was examined through simple sensitivity tests. The results showed that an increase in bulk density by 0.02 g cm^{-3} can change the retrievals of the 3rd moments by nearly 50% and the total concentration by 60%. Similar retrieval sensitivity is expected for variations of particle axis ratios as they are also related to the scattering behavior of ice particles. The changes in the retrievals were less sensitive to variations in the Λ-μ relation. The improvement was most significant for N_T when the distribution was broadened and shifted to larger particle sizes as the RMSE was reduced by 14 % to 10.75×10^4 m^{-3}. On the other hand, making the PSDs narrower increased the RMSE by 30.4% to 16.43×10^4 m^{-3}. The changes were less noticeable for the 3rd moments. Test results suggest that the current retrieval procedure is sensitive to the ρ_s-D relation, and produces too many small, dense particles as stated previously.

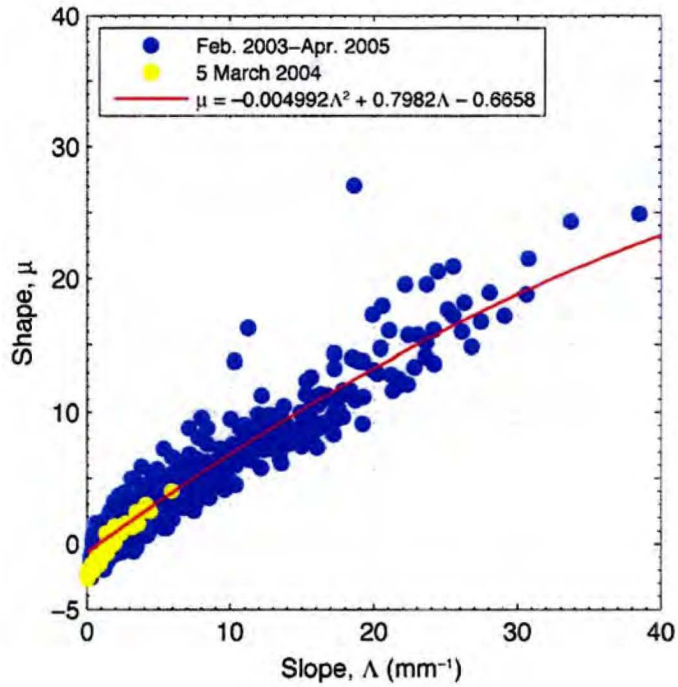

Figure 7.1: Scatter plot of shape parameter (μ) and slope (Λ) of 5-minute PSDs from data collected between February 2003 and April 2005 (blue dots). A least-square fit through the data points is overlaid (red line). Data points in yellow are from the 5 March 2004 event.

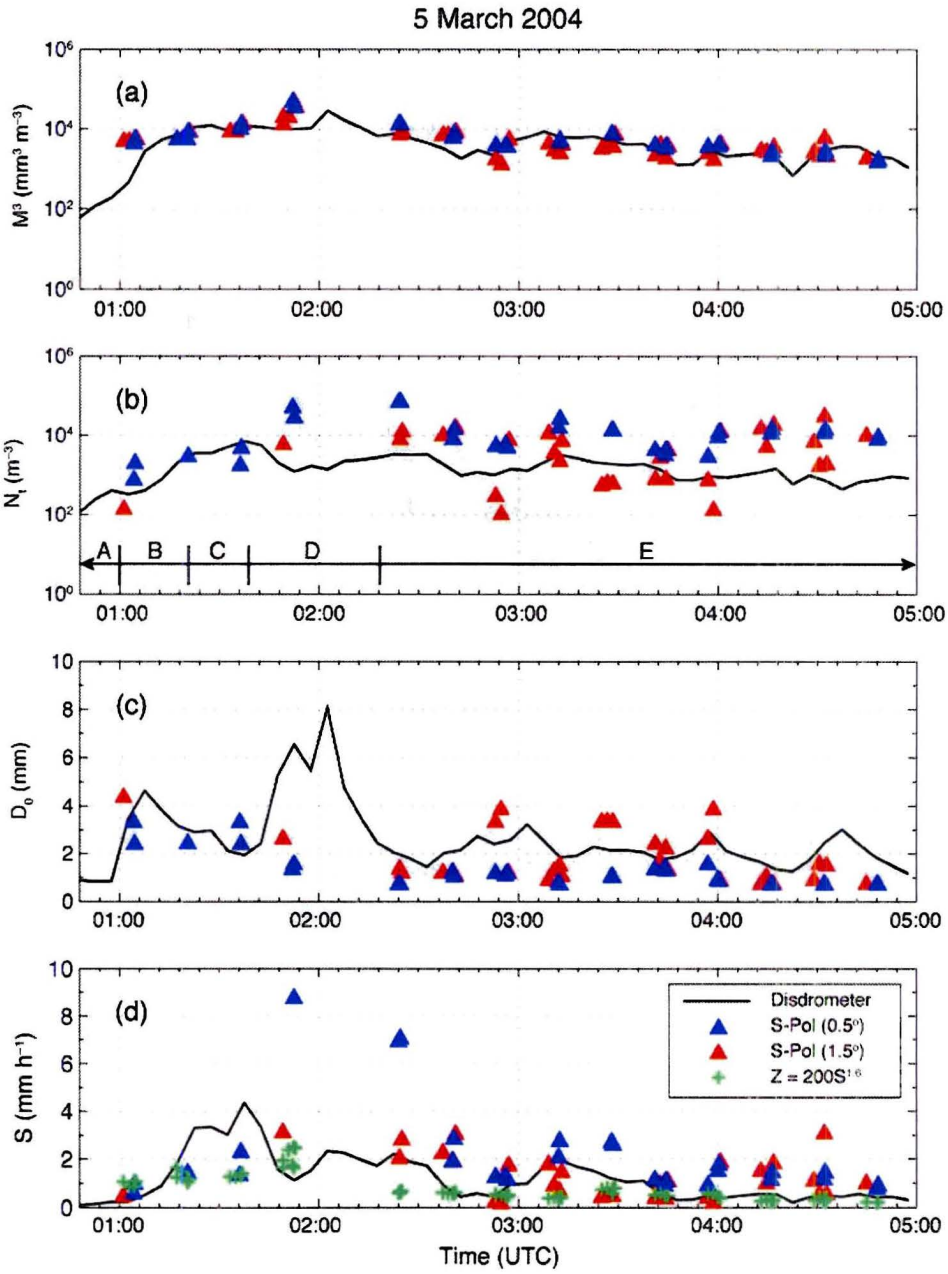

Figure 7.2: Time series of (a) the third-order moments of 5-minute PSDs (M^3), (b) total concentration (N_t), (c) median equivalent volume diameter (D_0), and (d) snowfall rate (S) for 5 March 2004. Solid lines are disdrometer observations, and the triangles are the retrievals from the radar measurements. The green crosses in (d) show snowfall rate computed from Eq.7.6.

Equation Chapter 8 Section 1

CHAPTER 8

SUMMARY AND CONCLUSIONS

8.1 Summary and conclusions

Radar reflectivity and differential reflectivity were computed for rain and snow as observed by a video disdrometer and compared to simultaneous radar measurements collected during two precipitation events. The scattering amplitudes for ice particles, computed from the T-matrix technique, were derived by exploiting an empirical relationship between particle size (D) and bulk ice particle density (ρ_s) (Eq. 3.4). The ρ_s-D relation accounted for changes in bulk density of ice particles in order to better characterize the precipitation in the calculations. The shape of the ice particles was assumed to be oblate with a fixed aspect ratio of 0.7.

The two precipitation systems studied here occurred on 20 February and 5 March 2004. Shallow precipitation formed on both days over the WISP04 domain within upslope flows associated with low pressure systems. The precipitation was mostly a mixture of rain and snow on 20 February, and three stages of the mixed-phase precipitation were identified. The first stage occurred in association with a rapid lowering of the 0°C level and a formation of a barrier jet (Period B). The precipitation was characterized with raindrops and a relatively small concentration of aggregates. The

latter two mixed-phase precipitation periods were associated with a passage of a wind shear-induced precipitation fall streak, within which aggregates formed. The aggregates were mixed with light rain at the ground level. On the other hand, it was suggested that little aggregation occurred outside the fall streak, and ice crystals possibly rimed. At the ground level, the precipitation outside the fall streak consisted of raindrops with small irregular ice particles ($D < 2$ mm). The source regions of the precipitation streaks near the cloud top were depicted with high Z_{DR} (1.8-4 dB) and low Z_H (< 5 dBZ), which suggested the presence of oriented pristine ice crystals.

The precipitation on 5 March 2004 was more stratiform in nature compared with the 20 February case possibly due to a relatively higher atmospheric stability which suppressed overturning. There were distinct periods of rain, rain-snow transition, active aggregation, and riming. Similar to the previous case, the onset of the rain-snow transition period was associated with an abrupt cooling of the surface layer. However, the precipitation during the rain-snow transition period on 5 March 2004 was dominated by large aggregates, and not rain. The transition from the active aggregation to riming stages was explained by the reduced efficiency in the aggregation process due to the gradual cooling at low levels to temperatures less than -7°C, as well as by the possible change in hydrometeor types from branched ice crystals such as dendrites with ferns to ice crystals that form in colder environments. Consistent with the surface observations, the radar measurements showed a general increase in Z_{DR} and decrease in Z_H at low levels as this transition occurred.

Overall, the comparisons between the measured and computed Z_H and Z_{DR} showed good agreement. On 5 March 2004, the computed values during the snow period

mirrored the changes in hydrometeor habits. Aggregates were associated with small Z_{DR} and large Z_H as expected. An increase in bulk density, as the number of aggregates decreased and that of compact graupel and irregular ice particles increased, was reflected by a general increase in Z_{DR} and a decrease in Z_H in both the measurements and the estimations. The results revealed that the use of the size-density relation was important in achieving good agreement between the computed values and measurements. Additionally, the agreement was better achieved during mixed-phase periods when the scattering amplitudes of the dominant hydrometeor type (i.e., in liquid or solid phase) in terms of size and/or concentration were assumed. For example, a better agreement was with the calculations based on ice particle-scattering amplitudes during the rain-snow transition period on 5 March 2004 because large aggregates (D_{max} of ~8-9 mm) overwhelmed the radar reflectivities (due to the D^6-dependency of Z_H) and thereby masked the presence of rain despite the higher dielectric factor of rain. In contrast, the correspondence was better for the rain-based estimations on 20 February 2004 while rain dominated over aggregates during the rain-snow transition period (Period B), and while a relatively small number of irregular particles were observed with rain during the third mixed-phase period (Period D). Large biases in the Z_H and Z_{DR} estimations during the mixed-phase periods when applying the scattering amplitudes for the less dominant hydrometeor type, disclose the importance of knowing the dominant hydrometeor type. However, the ratio between the sizes of ice particles and raindrops and that of the ice particle and raindrop concentration that would determine which scattering amplitudes to apply to estimate radar observables are yet to be quantified.

The sensitivity of the scattering calculations to ρ_s and axis ratio of particles were examined based on the Rayleigh-Gans approximation using data from the 5 March 2004 case. The biases in the computed Z_H and Z_{DR}, when applying various size-dependent ρ_s relations found in the literature, were 2-10 dBZ and 0.2-0.4 dB, respectively. The discrepancies were typically larger when holding ρ_s fixed because biases in ρ_s increased with size and accumulated over the size spectra, and therefore significantly affecting the resulting scattering amplitudes. In this study, the largest offsets were 20 dBZ (Z_H) and 1.0 dB (Z_{DR}) when assuming ρ_s of 0.7 g cm^{-3} for graupel particles. The best agreement between the disdrometer-based and radar-measured values was with the ρ_s-D relation derived using Eq. 3.4. The results reveal that the use of a size-dependent ρ_s is essential in reducing the error in estimations of radar parameters.

In order to examine sensitivity to particle shapes, axis ratios for the observed particle types found in the literature and empirical relations between aspect ratios and size derived from the current disdrometer observations were considered. Consistent with previous research (e.g., Hall et al. 1984; Herzegh and Jameson 1992), Z_{DR} decreased as particles became less oblate, and the sensitivity to the axis ratio reduced with increasing particle size due to a decrease in dielectric factor associated with lower bulk density. When using the empirical relation between the aspect ratio and particle size in conjunction with Eq. 3.4, there were less temporal fluctuations in Z_{DR} because the relation between the two variables was weak.

The disdrometer-based Z_H and Z_{DR} in the present case studies were generally within one standard deviation of the radar measurements collected within 1-km of the disdrometer [2-3 dBZ for Z_H in both cases; 0.2-0.4 dB (20 February) and 0.2-0.3 dB (5

March) for Z_{DR}]. The bias in the computed Z_H values was smaller than the calculations with the PARSIVEL disdrometer data performed by Löffler-Mang and Blahak (2001) (3-5 dBZ in stratiform and -6-16 dBZ in convective cases). The larger bias with the PARSIVEL disdrometer is in part due to estimating the particle masses from the maximum dimension of the particles. The high temporal and pixel resolutions of the 2-D Video disdrometer for measuring size and fall velocity of individual particles, and its ability to sufficiently sample large snowflakes, clearly provided adequate data for this study. The disdrometer measurements also facilitated discriminating rain and snow and showed interesting features in the evolution of the size spectra. For example, the disdrometer evidenced a rapid broadening of the size distributions at the onset of the rain-snow transition followed by a relatively stable particle size distributions of ice particles, characterized with much smaller Λ than rain and small negative/positive values of μ.

Reproduction of radar parameters with disdrometer observations is an important initial step in the development of radar-based algorithms for winter precipitation. Well-matched retrievals provide a foundation for reconstructing particle size distributions. Such a capability is required for improving microphysical parameterizations in numerical forecast models and quantifying winter precipitation from radar measurements.

The PSD retrieval procedure based on the measurements of Z_H and Z_{DR} produced an overall agreement in total particle volume while the total particle concentration was generally overestimated. Consequently, snowfall rate retrieved from the radar measurements was poorly correlated with the disdrometer measurements. Results showed that the procedure is sensitive to the empirical relations between the bulk ice particle density and particle size due in part to the small dynamic range of Z_{DR} for snow

while bulk density rapidly increases for particle size < 2.5 mm. The retrievals were less sensitive to variations in the relation between slope and shape parameters. In order to improve the retrieval method and develop radar-based algorithms to be used for winter weather, examination of additional polarimetric radar and disdrometer datasets are in order.

8.2 Recommendations for future research

The initial step of verifying a good correspondence between the video disdrometer and radar observations has been achieved in this study, and the current findings laid the groundwork for further research required in order to develop radar-based algorithm for cold season precipitation. Recommendations for future research are,

- Apply scattering models for disdrometer-observed melting ice particles and snow aggregates, and compare to the radar measurements
- Incorporate fall mode of the ice particles in the current scattering model and perform radar-disdrometer comparisons
- Explore the feasibility of utilizing the disdrometer-observed particle shapes for examining backscattering amplitudes of various ice particles
- Quantify factors that determines the dominance of a particular hydrometeor type over others (for example rain versus snow aggregates) in terms of size and/or number that justify better agreements between the measured and computed radar observables when using scattering amplitudes of the more-

representative hydrometeor phase (liquid versus solid) during a rain-to-snow transition period

- Perform additional radar-disdrometer comparisons on several precipitation events
- Improve the current retrieval technique by using a Λ-μ relationship determined from higher moment of size distribution, for example.

The above-listed researches calls for:

- Examining data collected in a wind-protected environment to investigate ice particle shapes and determine relation between axis ratio and particle size
- Taking detailed notes while collecting disdrometer data in order to verify hydrometeor types being sampled by the disdrometer (for example, small raindrops versus snow grain; wet versus dry snowflakes)
- Collecting additional radar-disdrometer comparison data.

REFERENCES

Auer, A. H., and D. L. Veal, 1970: The dimension of ice crystals in natural clouds. *J. Atmos. Sci.*, **27,** 919-926.

Aydin, K., T. A. Seliga, and V. Balaji, 1986: Remote sensing of hail with a dual-linear polarization radar. *J. Climate Appl. Meteor.*, **25,** 1475-1484.

Barber, P., and C. Yeh, 1975: Scattering of electromagnetic waves by arbitrarily shaped dielectric bodies. *App. Optics*, **14,** 2864-2872.

Barthazy, E., S. Göke, R. Schefold, and D. Högl, 2004: An optical spectrometer for shape and fall velocity measurements of precipitation size hydrometeors. *J. Atmos. Ocean. Technol.*, **21,** 1400-1416.

Bernstein, B. C., 2000: Regional and local influences on freezing drizzle, freezing rain, and ice pellet events. *Wea. Forecasting*, **15,** 485-508.

Bluestein, H. 1992: *Synoptic-dynamic Meteorology in Midlatitudes.* Vol. 2, Oxford University Press, Oxford, U.K., 594 pp.

Boatman, J. F., and R. F. Reinking, 1984: Synoptic and mesoscale circulations and precipitation mechanisms in shallow upslope storms over the Western high-plains. *Mon. Wea. Rev.* **112,** 1725-1744.

Brandes, E. A., G. Zhang, and J. Vivekanandan, 2002: Experiments in rainfall estimation with a polarimetric radar rainfall estimator. *J. Appl. Meteor.*, **41,** 674-685.

Brandes, E. A., G. Zhang, and J. Vivekanandan, 2004: Drop size distribution retrieval with polarimetric radar: Model and application. *J. Appl. Meteor.*, **43,** 461-475.

Brandes, E. A., J. Vivekanandan, and J. D. Tuttle, 1995: A study of thunderstorm microphysics with multiparameter radar and aircraft observations. *Mon. Wea. Rev.*, **123,** 3129-3143.

Brandes, E. A., K. Ikeda, G. Zhang, M. Schönhuber, and R. M. Rasmussen, 2006: A statistical and physical description of hydrometeor distributions in Colorado snow storms using a video disdrometer. *J. Appl. Meteor.* In press.

Bringi, V. N., and V. Chandrasekar, 2001: *Polarimetric Doppler Weather Radar.* Cambridge University Press, 636 pp.

Bringi, V. N., G. J. Huang, and V. Chandrasekar, 2001: An areal rainfall estimator using differential propagation phase: Evaluation using a C-band radar and a dense gauge network in the tropics. *J. Atmos. Oceanic Technol.*, **18,** 1810-1818.

Bringi, V. N., J. Vivekanandan, and J. D. Tuttle, 1986: Multiparameter measurements in Colorado convective storms. 2. Hail detection studies. *J. Atmos. Sci.*, **43,** 2564-2577.

Brown, P. R. A., and P. N. Francis, 1995: Improved measurements of the ice water-content in cirrus using a total-water probe. *J. Atmos. Oceanic Technol.*, **12,** 410-414.

Carbone, R. E., and A. R. Bohne, 1975: Cellular snow generation-Doppler radar study. *J. Atmos. Sci.*, **32,** 1384-1394.

Cotton, W. R., and R. A. Anthes, 1989: *Storm and Cloud Dynamics.* Academic Press, San Diego, California, 883 pp.

Doviak, R. J., and D. S. Zrnic, 1993: *Doppler Radar and Weather Observations.* Academic Press, San Diego, California, 562 pp.

Evans, K. F., and J. Vivekanandan 1990: Multiparameter radar and microwave radiative-transfer modeling of nonspherical atmospheric ice particles. *IEEE Trans. Geosci. Remote Sens.*, **28,** 423-437.

Fabry, F., and I. Zawadzki, 1995: Long-term radar observations of the melting layer of precipitation and their interpretation. *J. Atmos. Sci.*, **52,** 838-851.

Fabry, F., and W. Syzrmer 1999: Modeling of the melting layer. Part II: Electromagnetic. *J. Atmos. Sci.*, **56,** 2593-3600.

Field, P. R., R. J. Hogan, and P. R. A. Brown, 2004: Simultaneous radar and aircraft observations of mixed-phase cloud at the 100m scale. *Quart. J. Roy. Meteor. Soc.*, **130,** 1877-1904.

Fukuta, N., and T. Takahashi, 1999: The growth of atmospheric ice crystals: A summary of findings in vertical supercooled cloud tunnel studies. *J. Atmos. Sci.*, **56,** 1963-1979.

Goddard, J. W. F., and S. M. Cherry, 1984: The ability of dual-polarization radar (copolar linear) to predict rainfall rate and microwave attenuation. *Radio Sci.*, **19,** 201-208.

Goedecke, G. H., and S. G. O'Brien, 1988: Scattering by irregular inhomogeneous particles via the digitized greens-function algorithm. *Appl. Optics*, **27,** 2431-2438.

Gorgucci, E., V. Chandrasekar, V. N. Bringi, and G. Scarchilli, 2002: Estimation of raindrop size distribution parameters from polarimetric radar measurements. *J. Atmos. Sci.*, **59,** 2373-2384.

Hall, M. P. M., J. W. F. Goddard, and S. M. Cherry, 1984: Identification of hydrometeors and other targets by dual-polarization radar. *Radio Sci.*, **19,** 132-140.

Herzegh, P. H., and A. R. Jameson, 1992: Observing precipitation through dual-polarization radar measurements. *Bull. Amer. Meteor. Soc.*, **73,** 1365-1374.

Herzegh, P. H., and J. W. Conway, 1986: On the morphology of dual-polarization radar measurements: Distinguishing meteorological effects from radar system effects. Preprints, *23rd Conference on Radar Meteorology,* Snowmass, CO, Amer. Meteor. Soc., 55-58.

Herzegh, P. H., and P. V. Hobbs, 1980: The mesoscale and microscale structure and organization of clouds and precipitation in mid-latitude cyclones. Part II: Warm-frontal clouds. *J. Atmos. Sci.*, **37,** 597-611.

Heymsfield, A., 1972: Ice crystal terminal velocities. *J. Atmos. Sci.*, **29,** 1348-1357.

Heymsfield, A., 1978: The characteristics of graupel particles in Northeastern Colorado cumulus congestus clouds. *J. Atmos. Sci.*, **35,** 284-295.

Hobbs, P. V., 1975: Nature of winter clouds and precipitation in Cascade Mountains and their modification by aircraft seeding. Part I: Natural conditions. *J. Appl. Meteor.*, **14,** 783-804.

Hobbs, P. V., T. J. Matejka, P. H. Herzegh, J. D. Locatelli, and R. A. Houze, 1980: The mesoscale and microscale structure and organization of clouds and precipitation in mid-latitude cyclones. Part I: A case-study of a cold-front. *J. Atmos. Sci.*, **37,** 568-596.

Hogan, R. J., A. J. Illingworth, and H. Sauvageot, 2000: Measuring crystal size in cirrus using 35- and 94-GHz radars. *J Atmos. Oceanic Technol.*, **17,** 27-37.

Hogan, R. J., P. R. Field, A. J. Illingworth, R. J. Cotton, and T. W. Choularton, 2002: Properties of embedded convection in warm-frontal mixed-phase cloud from aircraft and polarimetric radar. *Quart. J. Roy. Meteor. Soc.*, **128,** 451-476.

Holroyd, III, E. W., 1971: The meso- and microscale structure of Great Lakes snowstorm bands: A synthesis of ground measurements, radar data, and satellite observations. Ph.D. dissertation, State University of New York at Albany, 148 pp.

Ishimaru, A., 1991: *Electromagnetic Wave Propagation, Radiation, and Scattering.* Prentice Hall, Englewood Cliffs, NJ, 637 pp.

Jayaweera, K. O. L. F., and R. E. Cottis, 1969: Fall velocities of plate-like and columnar ice crystals. *Quart. J. Roy. Meteor. Soc.*, **55,** 703-709.

Jayaweera, K. O. L. F., and T. Ohtake, 1974: Properties of columnar ice crystals precipitating from layer clouds. *J. Atmos. Sci.*, **31,** 280-286.

Kozu, T., and K. Nakamura, 1991: Rain parameter estimation from dual-radar measurements combining reflectivity profile and path-integrated attenuation. *J. Atmos. Oceanic Technol.*, **8,** 259-270.

Kruger, A., and W. F. Krajewski, 2002: Two-dimensional video disdrometer: A description. *J. Atmos. Oceanic Technol.*, **19,** 602-616.

Liao, L., R. Meneghini, T. Iguchi, and A. Detwiler, 2005: Use of dual-wavelength radar for snow parameter estimates. *J. Atmos. Oceanic Technol.*, **22,** 1494-1506.

Locatelli, J. D., and P. V. Hobbs, 1974: Fall speeds and masses of solid precipitation particles. *J Geophys. Res.*, **79,** 2185-2197.

Long, D. A., 2004: Evaluating the use of polarimetric cloud radars for studying winter storms. M.S. thesis, Dept. of Atmospheric Science Colorado State University, 87 pp.

Löffler-Mang, M., and U. Blahak, 2001: Estimation of the equivalent radar reflectivity factor from measured snow size spectra. *J. Appl. Meteor.*, **40,** 843-849.

Nespor, V., W. F. Krajewski, and A. Kruger, 2000: Wind-induced error of raindrop size distribution measurement using a two-dimensional video disdrometer. *J. Atmos. Oceanic Technol.* **17,** 1483-1492.

Magono, C., and C. W. Lee, 1966: Meteorological classification of natural snow crystals. *J. Fac. Sci.* Hokkaido Univ., Ser. 7, 321-362.

Magono, C., and T. Nakamura, 1965: Aerodynamic studies of falling snow flakes. *J. Atmos. Soc. Japan,* **43,** 139-147.

Mahoney, J. L., J. M. Brown, and E. I. Tollerud, 1995: Contrasting meteorological conditions associated with winter storms at Denver and Colorado Springs. *Wea. Forecasting*, **10,** 245-260.

Marshall, J. S., 1953: Precipitation trajectories and patterns. *J. Atmos. Sci.*, **10,** 25-29.

Marwitz, J. D., 1983: The kinematics of orographic airflow during Sierra storms. *J. Atmos. Sci.*, **40,** 174-185.

Marwitz, J. D., 1987: Deep orographic storms over the Sierra Nevada. Part I: Thermodynamic and kinematic structure. *J. Atmos. Sci.*, **44,** 159-173.

Marwitz, J. D., and J. Toth, 1993: The Front Range Blizzard of 1990. Part I: Synoptic and mesoscale structure. *Mon. Wea. Rev.*, **121,** 402-415.

Matrosov, S. Y., R. F. Reinking, R. A. Kropfli, and B. W. Bartram, 1996: Estimation of ice hydrometeor types and shapes from radar polarization measurements. *J. Atmos. Oceanic Technol.*, **13,** 85-96.

Matrosov, S. Y., R. F. Reinking, R. A. Kropfli, B. E. Martner, and B. W. Bartram, 2001: On the use of radar depolarization ratios for estimating shapes of ice hydrometeors in winter clouds. *J. Appl. Meteor.*, **40,** 479-490.

Meischner, P. F., V. N. Bringi, M. Hagen, and H. Holler, 1991: A squall line in southern Germany: Kinematics and precipitation formation as deduced by advanced polarimetric and Doppler radar measurements. *Mon. Wea. Rev.*, **119,** 678-701.

Meneghini, R., and L. Liao, (2000): Effective dielectric constants of mixed-phase hydrometeors. *J. Atmos. Oceanic Technol.*, **17,** 628-640.

Muramoto, K., K. Matsuura, and T. Shiina, 1995: Measuring the density of snow particles and snowfall rate. *Elect. Commun. Japan.,* **78,** 2353-2360.

Parish, T. R., 1986: Barrier winds along the Sierra Nevada Mountains. *J. Appl. Meteor.*, **21,** 925-930.

Pobanz, B. M., J. D. Marwitz, and M. K. Politovich, 1994: Conditions associated with large-drop regions. *J. Appl. Meteor.*, **33,** 1366-1372.

Pruppacher, H. R., and J. D. Klett, 1997: *Microphysics of Clouds and Precipitation*, 2nd Ed., Kluwer Academic Publishers, Dordrecht, The Netherlands, 954 pp.

Purcell, E. M., and C. R. Pennypacker, 1973: Scattering and absorption of light by non-spherical dielectric grains. *Astrophys. J.*, **186,** 705-714.

Rasmussen, R. M., B. C. Bernstein, M. Murakami, G. Stossmeister, J. Reisner, and B. Stankov, 1993: The 1990 Valentine's Day Arctic outbreak. Part I: Mesoscale and microscale structure and evolution of a Colorado Front Range shallow upslope cloud. *J. Appl. Meteor.*, **34,** 1481-1511.

Rogers, D. C., 1974: The aggregation of natural ice crystals. M.S. thesis, Dept. of Atmospheric Resources, University of Wyoming, 34 pp.

Ryzhkov, A. V., and D. S. Zrnic, 1998: Discrimination between rain and snow with a polarimetric radar. *J. Appl. Meteor.*, **37,** 1228-1240.

Ryzhkov, A. V., D. S. Zrnic, and B. A. Gordon, 1998: Polarimetric method for ice water content determination. *J. Appl. Meteor.*, **37,** 125-134.

Ryzhkov, A. V., T. J. Schuur, D. W. Burgess, P. L. Heinselman, S. E. Giangrande, and D. S. Zrnic, 2005: The Joint Polarization Experiment: Polarimetric rainfall measurements and hydrometeor classification. *Bull. Amer. Meteor. Soc.*, **84,** 1807-1826.

Schöenhuber, M., 1998: About interaction of precipitation and electromagnetic waves. Ph.D. dissertation, Technical University, Graz, Germany, 181 pp.

Seliga, T. A., V. N. Bringi, H. H. Alkhatib, 1981: A preliminary-study of comparative measurements of rainfall rate using the differential reflectivity radar technique and a raingage network. *J. Appl. Meteor.*, **20,** 1362-1368.

Smith, P. L., 1984: Equivalent radar reflectivity factors for snow and ice particles. *J. Climate Appl. Meteor.*, **23,** 1258-1260.

Straka, J. M., D. S. Zrnic, and A. V. Ryzhkov, 2000: Bulk hydrometeor classification and quantification using polarimetric radar data: Synthesis of relations. *J. Appl. Meteor.*, **39,** 1341-1372.

Thurai, M., and V. N. Bringi, 2005: Drop axis ratios from a 2D video disdrometer. *J. Atmos. Oceanic Technol.*, **22,** 966-978.

Vivekanandan, J., G. Zhang, and E. A. Brandes, 2004: Polarimetric radar estimators based on a constrained gamma drop size distribution model. *J. Appl. Meteor.*, **43,** 217-230.

Vivekanandan, J., R. Raghavan, and V. N. Bringi, 1993: Polarimetric radar modeling of mixture of precipitation particles. *IEEE Trans. Geosci. Remote Sens.*, **31,** 1071-1030.

Vivekanandan, J., W. M. Adams, and V. N. Bringi, 1991: Rigorous approach to polarimetric radar modeling of hydrometeor orientation distributions. *J. Appl. Meteor.*, **30,** 1053-1063.

Vivekanandan, J., G. Zhang, and M. Politovich, 2001: An assessment of droplet size and liquid water content derived from dual-wavelength radar measurements to the application of aircraft icing detection. *J. Atmos. Oceanic Technol.*, **18,** 1787-1898.

Vivekanandan, J., V. N. Bringi, M. Hagen, and P. Meischner, 1994: Polarimetric radar studies of atmospheric ice particles. *IEEE Trans. Geosci. Remote Sens.* **32,** 1-10.

Vivekanandan, J., D. S. Zrnic, S. M. Ellis, R. Oye, A. V. Ryzhkov, and J. Straka, 1999: Cloud microphysics retrieval using S-band dual-polarization radar measurements. *Bull. Amer. Meteor. Soc.*, **80,** 381-388.

Wolde, M., and G. Vali, 2001: Polarimetric signatures from ice crystals observed at 95 GHz winter clouds. Part I: Dependence on crystal form. *J. Atmos. Sci.*, **58,** 828-841.

Zawadzki, I., W. Szyrmer, C. Bell, and F. Fabry, 2005: Modeling of the melting layer. Part III: The density effect. *J. Atmos. Sci.*, **62,** 3705-3723.

Zhang, G., J. Vivekanandan, and E. Brandes, 2001: A method for estimating rain rate and drop size distribution from polarimetric radar measurements. *IEEE Trans. Geosci. Remote Sens.*, **39**, 830-841.

Zikmunda, J., and G. Vali, 1972: Fall patterns and fall velocities of rimed ice crystals. *J. Atmos. Sci.*, **29,** 1334-1347.